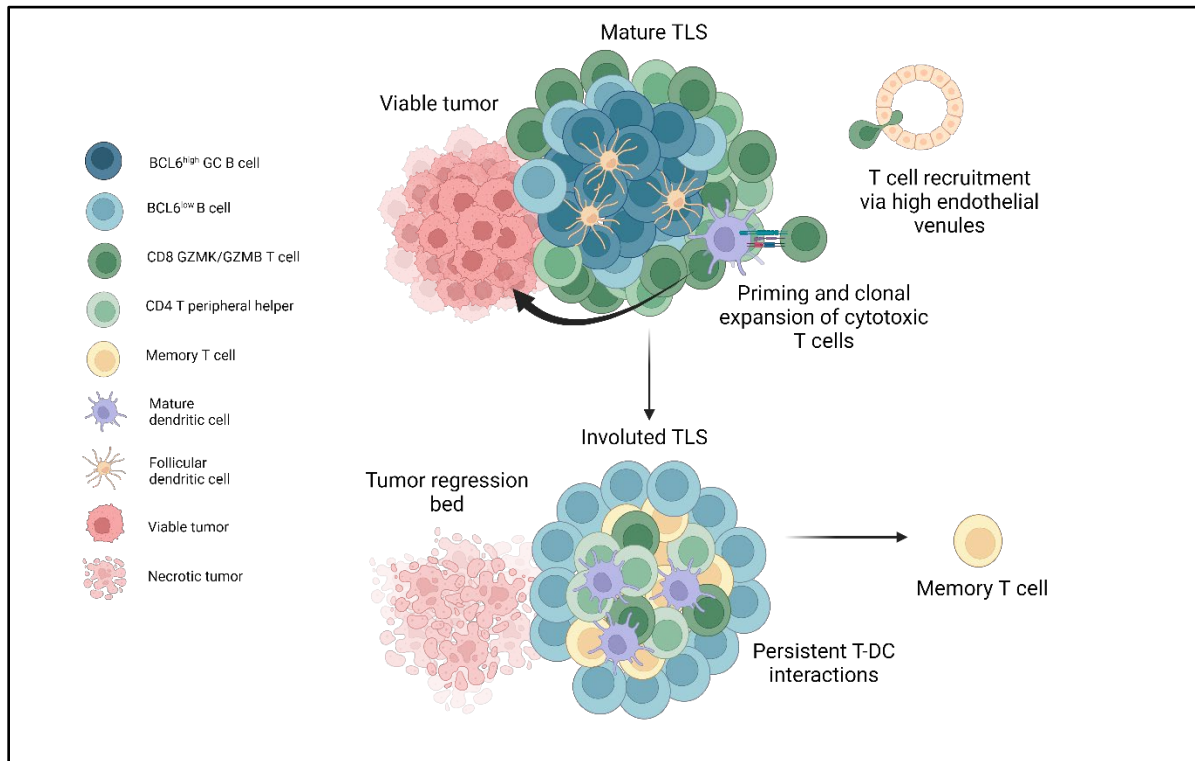


1  
2

## Graphical Abstract



3  
4  
5  
6  
7  
8  
9  
10  
11  
12  
13  
14  
15  
16  
17  
18  
19  
20  
21  
22  
23  
24  
25  
26

### Highlights

1. In patients with hepatocellular carcinoma (HCC), tertiary lymphoid structures (TLS) are induced by neoadjuvant immunotherapy and are associated with favorable clinical outcomes.
2. TLS within the same tumor demonstrate extensive sharing of expanded granzyme K and granzyme B-expressing CD8<sup>+</sup> T effector memory clonotypes, but the B cell repertoires of individual TLS are almost wholly distinct, consistent with independent germinal center reactions.
3. Within areas of viable tumor, mature TLS are characterized by high expression of CD21 and CD23, BCL6<sup>+</sup> germinal center B cells, and close interactions between DCLAMP<sup>+</sup> mature dendritic cells and CXCR5<sup>+</sup>CXCR3<sup>+</sup> CD4 T peripheral helper cells within a T cell zone adjacent to the B cell follicle.
4. Within areas of tumor regression, an involuted TLS morphology is identified that is notable for dissolution of the B cell germinal center, retention of the T cell zone, and increased T cell memory.

27 **Immune landscape of tertiary lymphoid structures in hepatocellular carcinoma (HCC)**  
28 **treated with neoadjuvant immune checkpoint blockade**

29

30 Daniel H. Shu<sup>1,2</sup>, Won Jin Ho<sup>1,2</sup>, Luciane T. Kagohara<sup>1,2</sup>, Alexander Girgis<sup>1,2,3</sup>, Sarah M. Shin<sup>1</sup>,  
31 Ludmila Danilova<sup>1</sup>, Jae W. Lee<sup>4</sup>, Dimitrios N. Sidiropoulos<sup>1,2</sup>, Sarah Mitchell,<sup>1</sup> Kabeer Munjal<sup>1</sup>,  
32 Kathryn Howe<sup>1</sup>, Kayla J. Bendinelli<sup>1</sup>, Hanfei Qi<sup>1</sup>, Guanglan Mo<sup>1</sup>, Janelle Montagne<sup>1,2</sup>, James M.  
33 Leatherman<sup>1</sup>, Tamara Y. Lopez-Vidal<sup>1,2</sup>, Qingfeng Zhu<sup>2,4</sup>, Amanda L. Huff<sup>1,2</sup>, Xuan Yuan<sup>3</sup>, Alexei  
34 Hernandez<sup>1</sup>, Erin M. Coyne<sup>1</sup>, Neeha Zaidi<sup>1,2</sup>, Daniel J. Zabransky<sup>1,2</sup>, Logan L. Engle<sup>5,6,7</sup>,  
35 Aleksandra Ogurtsova<sup>5,6,7</sup>, Marina Baretta<sup>1</sup>, Daniel Laheru<sup>1,2</sup>, Jennifer N. Durham<sup>1</sup>, Hao Wang<sup>1</sup>,  
36 Robert Anders<sup>2,4</sup>, Elizabeth M. Jaffee<sup>1,2,7</sup>, Elana J. Fertig<sup>1,2,3,8\*</sup>, Mark Yarchoan<sup>1,2,7\*</sup>

37

38 <sup>1</sup> Department of Oncology, Sidney Kimmel Comprehensive Cancer Center, Johns Hopkins  
39 University School of Medicine, Baltimore, Maryland.

40 <sup>2</sup> Convergence Institute, Johns Hopkins University, Baltimore, Maryland.

41 <sup>3</sup> Department of Biomedical Engineering, Johns Hopkins University School of Medicine, Baltimore,  
42 Maryland.

43 <sup>4</sup> Department of Pathology, Johns Hopkins University School of Medicine, Baltimore, Maryland,  
44 USA.

45 <sup>5</sup> Department of Dermatology, Johns Hopkins University School of Medicine, Baltimore, Maryland.

46 <sup>6</sup> The Mark Foundation Center for Advanced Genomics and Imaging, Johns Hopkins University,  
47 Baltimore, Maryland.

48 <sup>7</sup> Bloomberg~Kimmel Institute for Cancer Immunotherapy and Sidney Kimmel Comprehensive  
49 Cancer Center, Johns Hopkins University, Baltimore, Maryland.

50 <sup>8</sup> Department of Applied Mathematics and Statistics, Johns Hopkins University Whiting School of  
51 Engineering, Baltimore, Maryland.

52

53

54 \* Corresponding authors:

55 Mark Yarchoan (mark.yarchoan@jhmi.edu)

56 Elana J. Fertig (ejfertig@jhmi.edu)

57

58 **Keywords:** neoadjuvant immunotherapy, tertiary lymphoid structures, hepatocellular carcinoma,  
59 immune checkpoint inhibitors, single cell multiomics, imaging mass cytometry, single cell RNA,  
60 single cell TCR,

61 **ABSTRACT**

62  
63 Neoadjuvant immunotherapy is thought to produce long-term remissions through induction of  
64 antitumor immune responses before removal of the primary tumor. Tertiary lymphoid structures  
65 (TLS), germinal center-like structures that can arise within tumors, may contribute to the  
66 establishment of immunological memory in this setting, but understanding of their role remains  
67 limited. Here, we investigated the contribution of TLS to antitumor immunity in hepatocellular  
68 carcinoma (HCC) treated with neoadjuvant immunotherapy. We found that neoadjuvant  
69 immunotherapy induced the formation of TLS, which were associated with superior pathologic  
70 response, improved relapse free survival, and expansion of the intratumoral T and B cell  
71 repertoire. While TLS in viable tumor displayed a highly active mature morphology, in areas of  
72 tumor regression we identified an involuted TLS morphology, which was characterized by  
73 dispersion of the B cell follicle and persistence of a T cell zone enriched for ongoing antigen  
74 presentation and T cell-mature dendritic cell interactions. Involuted TLS showed increased  
75 expression of T cell memory markers and expansion of CD8<sup>+</sup> cytotoxic and tissue resident  
76 memory clonotypes. Collectively, these data reveal the circumstances of TLS dissolution and  
77 suggest a functional role for late-stage TLS as sites of T cell memory formation after elimination  
78 of viable tumor.

79  
80 **INTRODUCTION**

81  
82 Immune checkpoint blockade (ICB) therapy has revolutionized the treatment of metastatic solid  
83 tumors, offering to a subset of patients the potential for sustained remissions beyond what was  
84 previously possible with chemotherapy alone.<sup>1,2</sup> For patients with early stage, non-metastatic  
85 disease, the role for ICB and ideal timing of its administration remains an area of intense clinical  
86 investigation. Recent clinical data in patients with melanoma suggest that neoadjuvant  
87 immunotherapy, in which ICB is administered prior to curative-intent resection of the primary  
88 tumor, may produce superior long-term outcomes compared to immunotherapy given after  
89 surgery.<sup>3,4</sup> Preclinical data suggest that these improved outcomes may be attributable to an  
90 elevated and sustained tumor-specific immune response that occurs when immunotherapy is  
91 initiated with the primary tumor *in situ*.<sup>5,6</sup> However, in human subjects it is not known where or by  
92 what means the establishment of immunological memory occurs.

93  
94 Tertiary lymphoid structures (TLS), organized collections of B and T cells that can arise within  
95 solid tumors, have been associated with favorable responses to neoadjuvant ICB,<sup>7-13</sup> and it is  
96 hypothesized that TLS play a mechanistic role in promoting effective antitumor immunity.  
97 However, understanding of the structure, constituent immune populations, and life cycle of TLS  
98 in this treatment setting remains limited by the rarity of neoadjuvant clinical trial specimens,  
99 particularly in solid tumor types where the successes of immunotherapy have been modest, and  
100 paucity of animal models for TLS in cancer.<sup>14,15</sup> Thus patient samples from neoadjuvant clinical  
101 trials provide a unique opportunity to investigate the contribution of TLS to the development of  
102 antitumor immunity.

103  
104 We previously reported an association between TLS and pathologic response in a phase 1 trial  
105 of patients with locally advanced HCC who received neoadjuvant nivolumab and cabozantinib.<sup>8</sup>  
106 Here, we evaluated the clinical and immunological characteristics of TLS in an expanded cohort  
107 of patients with locally advanced hepatocellular carcinoma (HCC) treated with neoadjuvant ICB.  
108 We find evidence that neoadjuvant ICB induces the formation of intratumoral TLS, and that high  
109 TLS density following neoadjuvant therapy is associated with superior pathologic response to  
110 treatment and relapse-free survival. Using a multiomics approach employing imaging mass  
111 cytometry, bulk TCR and BCR sequencing of microdissected TLS, and paired single cell RNA

112 and TCR sequencing, we identify key differences in the spatial and immunological landscape of  
113 TLS in areas of viable and nonviable tumor that suggest that the contribution of TLS to antitumor  
114 immunity in tumors treated with neoadjuvant immunotherapy varies significantly according to  
115 morphological stage and circumstance.

116

## 117 RESULTS

118

### 119 Neoadjuvant ICB in HCC induces intratumoral TLS

120

121 To determine the clinical significance of TLS in patients with HCC treated with neoadjuvant ICB,  
122 we identified patients from the Johns Hopkins Liver Cancer Biorepository who had undergone  
123 surgical resection of their primary tumor after receiving neoadjuvant ICB-based therapy for locally  
124 advanced HCC. In total, 19 patients were identified who received treatment between October  
125 2019 and January 2022 (**Extended Data Table 1**). 11/19 (57.9%) were male, 13/19 (68.4%) had  
126 tumors with moderately differentiated histology, and 11/19 (57.9%) had a history of viral hepatitis.  
127 No patients had active viral hepatitis at the time of surgery. 14/19 (73.6%) received anti-PD-1 plus  
128 an oral tyrosine kinase inhibitor, 3/19 (15.8%) received anti-PD-1 monotherapy, 1/19 (5.2%)  
129 received combination anti-PD-1 and anti-CTLA-4 monoclonal antibody, and 1/19 (5.2%) received  
130 combination anti-PD-1/anti-CTLA-4 and oral TKI prior to resection of the primary tumor.

131

132 Since TLS are known to occur in treatment naïve HCC,<sup>16</sup> we first attempted to determine if TLS  
133 were present in the tumors of patients prior to receiving neoadjuvant ICB. 7/19 (36.8%) of patients  
134 had undergone pre-treatment fine needle biopsies prior to initiation of neoadjuvant therapy and  
135 no intratumoral TLS were identified in these specimens. Given the limited assessment of the  
136 tumor microenvironment provided by fine needle biopsy, we next identified a second cohort of  
137 HCC patients treated at our institution who had undergone surgical resection without receiving  
138 prior systemic therapy, which would serve as a control cohort. 17 patients were identified who  
139 had received upfront surgical resection for HCC between 2017 and 2022, from which 3 patients  
140 were excluded due to small tumor volume, poor tissue quality, or HCC etiology not represented  
141 by the treatment cohort. The 14 remaining patients (**Extended Data Table 2**), were similar to the  
142 neoadjuvant treatment cohort by age, sex, histologic grade, and etiology (**Table 1**).

143

144 Evaluation of TLS density in the two cohorts was performed by CD20 staining of resected FFPE  
145 tumor (**Fig. 1a**). TLS, which we defined as CD20<sup>+</sup> lymphoid aggregates with diameter greater than  
146 150  $\mu\text{m}$ , were classified as either peritumoral or intratumoral according to their location relative to  
147 the interface between tumor and normal adjacent parenchyma (**Fig. 1b**). TLS were observed in  
148 7/14 (50%) of untreated tumors and 12/19 (63.2%) treated tumors. No significant difference was  
149 identified in total TLS density ( $0.08 \pm 0.09$  TLS/ $\text{mm}^2$  versus  $0.05 \pm 0.10$  TLS/ $\text{mm}^2$ ,  $P = 0.42$ ) or  
150 peritumoral TLS density ( $0.03 \pm 0.05$  TLS/ $\text{mm}^2$  versus  $0.04 \pm 0.1$  TLS/ $\text{mm}^2$ ,  $P = 0.73$ ) (**Extended**  
151 **Fig. 1a**), but intratumoral TLS density was significantly increased in treated patients compared to  
152 untreated controls ( $0.05 \pm 0.08$  TLS/ $\text{mm}^2$  versus  $0.01 \pm 0.02$  TLS/ $\text{mm}^2$ ,  $P = 0.05$ ) (**Fig. 1c**). In  
153 untreated tumors, the majority of TLS were peritumoral, whereas in neoadjuvant treated tumors  
154 the majority were intratumoral (**Extended Data Fig 1b-c**). Taken together, these data suggest  
155 that neoadjuvant ICB induces the formation of intratumoral TLS.

156

### 157 High intratumoral TLS density after neoadjuvant ICB is associated with superior 158 pathologic response and disease-free survival

159

160 We next set out to determine if there were an association between high TLS density after  
161 neoadjuvant ICB and three clinically meaningful endpoints: pathologic response to treatment,  
162 relapse free survival, and overall survival. Tumors treated with neoadjuvant ICB were reviewed

163 and assigned to a pathologic response category (non-response [NR], partial pathologic response  
164 [pPR], or major or complete pathologic response [MPR/CR]) according to percent residual viable  
165 tumor at the time of surgery.<sup>17</sup> 8/19 (42.1%) patients had a major or complete pathologic response,  
166 of which 2 had CR and 6 had MPR; 8/19 (42.1%) had a partial pathologic response (pPR); and  
167 3/19 (15.8%) had non-response (NR). Intratumoral TLS density was significantly increased in  
168 tumors with MPR/CR compared to tumors with pPR ( $P = 0.000246$ ), NR ( $P = 0.0129$ ), or untreated  
169 patients ( $P = 0.000142$ ) by Tukey's HSD test. In addition, total TLS density was also increased in  
170 tumors with MPR/CR compared to tumors with pPR ( $P = 0.00144$ ), NR ( $P = 0.02$ ), and untreated  
171 tumors ( $P = 0.00694$ ) (**Fig. 1d** and **Extended Data Fig. 1d**). No significant difference was  
172 observed in peritumoral TLS density across pathologic response groups or untreated tumors  
173 (**Extended Data Fig. 1e**). Additional pathologic assessment was also performed according to the  
174 Immune Related Pathologic Response Criteria (irPRC), a set of categorical histopathologic  
175 criteria developed for standardized pathologic assessment of the regression bed of neoadjuvant  
176 immunotherapy treated solid tumors.<sup>17</sup> Using these criteria, we also observed a significant  
177 association between the presence of intratumoral TLS and MPR/CR ( $P = 0.02$ ), while no  
178 significant association was detected between peritumoral TLS and MPR/CR ( $P = 0.38$ ) (**Extended**  
179 **Data Table 3**). Thus, both a quantitative assessment of TLS density and a categorical evaluation  
180 of individual pathologic features suggested that intratumoral TLS density may be most correlated  
181 with response to treatment.

182  
183 We next examined relapse free survival and overall survival in the treated cohort, excluding the  
184 untreated cohort from analysis lack of follow up data for the majority of the cohort. Significantly  
185 longer relapse free survival after surgery was observed in treated patients in the upper tertile of  
186 intratumoral TLS density compared to patients in the middle and lower tertiles ( $P = 0.021$ ) (**Fig.**  
187 **1e**). At a median follow up of 38 months for patients in the upper tertile of intratumoral TLS density  
188 and 32 months for patients in the middle and lower tertiles, median RFS was not reached in the  
189 upper tertile and 9.1 months in the middle and lower group. RFS at 30 months was 100% and  
190 38.5% (95% CI, 19.3% to 76.5%), respectively. No significant difference in overall survival (OS)  
191 was observed between the two groups ( $P = 0.24$ ) (**Fig. 1f**), but at 30 months OS was 100% in the  
192 upper tertile and 76.9% (95% CI, 57.1% to 100%) in the middle and lower tertiles. In addition, we  
193 observed a trend toward improved RFS for patients in the upper tertile of total TLS density  
194 compared to the middle and lower tertiles ( $P = 0.13$ ) (**Extended Data Fig. 2a**). OS was not  
195 significantly different ( $P = 0.28$ ) (**Extended Data Fig. 2b**), but no deaths were observed in the  
196 upper tertile of total TLS density while three deaths were observed in the middle and lower tertiles.  
197 With respect to peritumoral TLS density, no difference was observed in relapse free survival ( $P =$   
198  $0.56$ ) or overall survival ( $p = 0.23$ ) when comparing the upper tertile to the middle and lower tertiles  
199 (**Extended Data Fig. 2c-d**). Notably, in this cohort MPR/CR, which was closely associated with  
200 high TLS density, was also associated with superior RFS ( $P = 0.025$ ) (**Extended Data Fig. 2e**).  
201 No significant difference was observed in OS ( $P = 0.16$ ) (**Extended Data Fig. 2f**), but no deaths  
202 were observed in the MPR/CR group while three deaths were observed in the pPR/NR group. In  
203 addition, we also evaluated outcomes according to sex and previous viral HBV or HCV infection  
204 and identified no significant differences in RFS or OS (**Extended Data Fig. 2g-l**). Finally, to  
205 compare the different clinical covariates, we used the Bayesian information criterion<sup>18</sup> to quantify  
206 the strength of each parameter in predicting relapse free survival or death after neoadjuvant ICB  
207 and surgical resection. The strongest predictors of relapse free survival by BIC analysis were  
208 intratumoral TLS density and pathologic response (**Extended Data Table 4**).

209  
210 **High TLS density after neoadjuvant ICB is associated with increased T and B cell activation**  
211 **and an expanded intratumoral T and B cell repertoire**

212

213 To identify differences in gene expression between tumors with high and low TLS density in this  
214 treatment context, we performed bulk RNA sequencing from FFPE surgical resection specimens.  
215 Tissue sections were collected from 14 tumors in the neoadjuvant treatment group, of which 2  
216 samples were excluded after quality control. The resultant 12 samples were designated as TLS  
217 high ( $n = 5$ ) or TLS low ( $n = 7$ ) according to total TLS density relative to the mean total TLS density  
218 of the treatment group. Here, total TLS density was used rather than intratumoral or peritumoral  
219 TLS density since bulk sequencing of FFPE tissue blocks did not have spatial resolution to  
220 account for these differences. By principal component analysis, the 5 TLS high tumors and 1 TLS  
221 low tumor clustered separately from the remaining TLS low tumors (**Fig. 2a**). Differential  
222 expression analysis using the R package DESeq2 identified 814 differentially expressed genes  
223 (DEG), defined as having fold change in the TLS high group greater than 2 times that of the TLS  
224 low group and false discovery rate less than 0.05 (**Fig. 2b-c** and **Extended Data Table 5**).

225  
226 Compared to TLS low tumors, TLS high tumors demonstrated significant overexpression of  
227 multiple genes belonging to the Gene Ontology Biological Pathways gene sets for T and B cell  
228 activation, cytokine production, and antigen presentation, including *CTLA4*, *IL7R*, *IL6*, the B cell  
229 activating factor *BAFF(TNFSF13B)* and its receptors *BAFF-R (TNFRSF13C)* and *TACI*  
230 (*TNFRSF13B*), and the T cell-derived cytokine *IL17C*. TLS high tumors displayed significantly  
231 greater expression of *CCL19*, a chemokine involved in T-cell and B-cell migration to secondary  
232 lymphoid organs, and *CXCR5*, the receptor for the B-cell chemoattractant *CXCL13*. TLS high  
233 tumors also demonstrated increased expression of multiple B-cell related genes such as the B  
234 cell antigen *CD79 (CD79A and CD79B)*, *CD20 (MS4A1)*, and Fc Receptor Like A protein (*FCRLA*)  
235 which is highly expressed in germinal center B cells.<sup>19</sup> In addition, we found increased expression  
236 of immunoregulatory genes including *IL10*, *IL17REL*, and the integrin  $\alpha\beta8$ -mediated *ITGB8*,  
237 which mediates TGF-beta-1 activation on the surface of regulatory T cells.<sup>20,21</sup> We also identified  
238 significantly increased expression of the gene encoding the germinal center regulatory protein  
239 *EBI2 (GPR183)*, *DOCK10*, which regulates *CD23* expression and sustains B-cell lymphopoiesis  
240 in secondary lymphoid tissue,<sup>22</sup> and *WDFY4*, a mediator of dendritic cell cross presentation.<sup>23</sup>

241  
242 Gene set enrichment analysis for human gene sets in the MSigDB collections further identified  
243 significant enrichment in TLS high tumors of pathways associated with increased adaptive  
244 immune response, including Hallmark pathways for allograft rejection and inflammatory response,  
245 and multiple pathways related to T and B cell receptor activation (**Fig. 2d-e** and **Extended Data**  
246 **Table 6**). Consistent with these findings, TLS high tumors also displayed increased expression of  
247 the 12-chemokine gene signature which has previously been found in association with TLS  
248 formation in multiple solid tumor types (**Extended Data Fig. 3a**).<sup>24</sup> Taken together, these bulk  
249 gene expression data demonstrate that tumors with high TLS density display significantly higher  
250 levels of T and B cell activation compared to TLS low tumors.

251  
252 To determine if TLS density was associated with differences in the adaptive immune repertoire,  
253 we used the Personalis Immunoid NeXT platform to extract immunoglobulin heavy chain (IGH),  
254 TCR $\beta$ , and TCR $\alpha$  repertoire data from bulk RNA sequencing data. Statistical power was limited  
255 by the small sample size, but in tumors with high TLS density there were a significant increase in  
256 total number of immunoglobulin heavy chain (IGH) clones ( $P = 0.02$ ), unique clonotypes ( $P =$   
257  $0.029$ ), and repertoire diversity ( $P = 0.043$ ) by Wilcoxon rank sum test (**Extended Data Fig. 4a-**  
258 **c**). In addition, we identified a trend toward increased median number of total clones, unique  
259 clonotypes, repertoire diversity in the TCR $\alpha$  ( $P = 0.29, 0.18, \text{ and } 0.18$ , respectively, by Wilcoxon  
260 rank sum test) (**Extended Data Fig. 4d-f**) and TCR $\beta$  repertoires ( $P = 0.22, 0.095, \text{ and } 0.095$ ,  
261 respectively, by Wilcoxon rank sum test) (**Extended Data Fig. 4g-i**). Overall, these findings  
262 suggest that high TLS density is associated with an expansion of the B and T cell repertoire in  
263 HCC treated with neoadjuvant immunotherapy.

264  
265 **In areas of tumor regression, an involuted TLS morphology is found that displays**  
266 **dissolution of the B cell germinal center, retention of the T cell zone, and increased**  
267 **expression of T cell memory markers**  
268

269 Based on these data, we hypothesized that a distinctive immunological process may occur in  
270 tumors with high intratumoral TLS density and major or complete pathologic response that  
271 contributes to long-term disease-free survival. To evaluate this hypothesis, we performed  
272 histologic examination of tumors with both viable tumor and extensive tumor regression beds. In  
273 viable tumor, the predominant phenotype observed was the canonical 'mature' stage of TLS  
274 characterized by a CD20<sup>+</sup> B cell germinal center surrounded by CD4<sup>+</sup> and CD8<sup>+</sup> T cells.<sup>25</sup> TLS of  
275 this morphology showed characteristically high expression of the follicular dendritic cell marker  
276 CD21 and the proliferation marker Ki67. In contrast, in areas of tumor regression bed we observed  
277 an 'involved' TLS morphology characterized by CD20<sup>+</sup> B cells in a halo-like ring surrounding a  
278 central core of CD4<sup>+</sup> and CD8<sup>+</sup> T cells. CD21 and Ki67 expression were low to absent (**Fig. 3a**).  
279 To confirm that this involuted morphology was not an artifact of sectioning, we performed serial  
280 sectioning and anti-CD20 staining of FFPE tissue sections and confirmed the absence of a dense  
281 B cell core as is seen in mature TLS (**Extended Data Fig. 5a**). These involuted TLS were highly  
282 associated with tumors with complete pathologic response, and in several tumors were found in  
283 series (**Extended Data Fig 5b**), suggesting a shared lymphatic supply. No TLS of this morphology  
284 were detected in untreated tumors.

285  
286 Given the location of the latter morphology within areas of nonviable tumor and the dispersed  
287 appearance of B cells in these lymphoid aggregates, we hypothesized that this morphology may  
288 represent TLS undergoing shutdown of the germinal center.<sup>26,27</sup> To characterize the features of  
289 this stage of TLS, we developed a 38-marker imaging mass cytometry antibody panel. Markers  
290 included in this panel were selected to identify different T cell subsets (CD3, CD4, CD8, FOXP3,  
291 CXCR3, CXCR5, ICOS), B cells subsets (CD20, BCL6, AID, CD138), follicular dendritic cells  
292 (CD21, CD23), dendritic cells (CD11c, DC-LAMP, CCR7), high endothelial venules (PNA<sup>d</sup>),  
293 macrophages (CD68), fibroblasts (Podoplanin [PDPN], αSMA), and tumor (CK). We included  
294 markers for T cell activation and exhaustion (CD25, CD69, CD137, PD-1, LAG3, TOX), co-  
295 stimulatory or antigen presenting molecules (CD86, HLA-DR), and markers of cell proliferation  
296 (Ki67) (**Extended Data Tables 7 and 8**). FFPE sections were obtained from the tumors of 9  
297 patients treated with neoadjuvant ICB, in 8 of which the involuted morphology was identified, and,  
298 after whole-slide staining, 31 regions of interest (ROI) were captured by laser ablation (**Extended**  
299 **Data Fig. 6a**) from which 38 TLS areas ( $n = 20$  mature and 18 involuted) were identified.

300  
301 Consistent with previously published data, imaging mass cytometry of mature TLS (**Fig. 3b**)  
302 demonstrated dense B cell follicle-like structures surrounded by peripherally located CD4<sup>+</sup> and  
303 CD8<sup>+</sup> T cells with associated high endothelial venules (HEV) with a cuboidal morphology.<sup>28,29</sup> In  
304 multiple HEV, we observed CD8<sup>+</sup> T cells in transit through these structures (**Fig. 3b, far left inset**).  
305 Mature TLS were also notable for an extensive CD21 and CD23 follicular dendritic cell network  
306 (**3b, middle left inset**), a distinct T cell zone with densely concentrated DCLAMP<sup>+</sup> mature  
307 dendritic cells in close contact with T cells (**3b, middle right inset**), and a dense PDPN<sup>+</sup> stromal  
308 network, similar to the fibroblastic reticular cell networks seen in secondary lymphoid organs<sup>15,30</sup>  
309 (**3b, far right inset**). Involved TLS (**Fig. 3c**) showed no detectable HEV with a cuboidal  
310 morphology, scattered CD21 and CD23 expression, and diminished PDPN expression, consistent  
311 with attenuation of the TLS structure. Notably, the center of involuted TLS demonstrated apparent  
312 persistence of the T cell zone with co-location of DCLAMP<sup>+</sup> mature dendritic cells and CD4<sup>+</sup> and  
313 CD8<sup>+</sup> T cells.

314

315 Further quantitative analysis of these structures supported these initial observations. After cell  
316 segmentation, we identified 61,371 single cells which were assigned to 16 distinct cell clusters  
317 (**Fig. 3d-f** and **Extended Data Fig. 6b-c**). In mature TLS we observed significantly higher density  
318 of a BCL6<sup>high</sup> population of B cells (B\_BCL6<sup>high</sup>), which was consistent with a germinal center B  
319 cell population ( $P = 0.00023$ ). In mature TLS, this cluster localized to the center of the B cell  
320 germinal center in close proximity to CD21<sup>+</sup>CD23<sup>+</sup> follicular dendritic cells and demonstrated high  
321 expression of HLADR, a marker of antigen presentation, and CD86, a B cell activation marker,  
322 consistent with an activate B cell population. A second B cell cluster was identified on the  
323 periphery of the B cell follicle which displayed lower expression of BCL6 (B\_BCL6<sup>low</sup>) and  
324 decreased expression of HLADR and CD86. This cluster was also found in significantly higher  
325 density in mature TLS ( $P = 0.038$ ). In contrast, in involuted TLS we observed significantly  
326 increased density of a third B cell cluster (B\_AID<sup>+</sup>) ( $P = 0.0026$ ), which was characterized by high  
327 expression of activation-induced cytidine deaminase (AID), the B cell enzyme which drives  
328 somatic hypermutation and class switch recombination. AID is induced by BCR cross-linking and  
329 has a half-life of 2.5 hours in the nucleus and 18-20 hours in its cytoplasmic form,<sup>31,32</sup> thus this  
330 population may correspond to B cells undergoing somatic hypermutation or memory B cells which  
331 had recently undergone immunoglobulin class switching, the latter of which we felt to be more  
332 likely given the context. No difference was observed in plasma cell densities between the two  
333 morphologies.

334  
335 In the T cell compartment, we identified a single cytotoxic CD8<sup>+</sup> T cell population (Tc) and two  
336 major CD4 T helper populations, a CD4<sup>+</sup>CXCR5<sup>-</sup>CXCR3<sup>+</sup> T peripheral helper (Tph) cluster, which  
337 was located around the peripheral of the B cell germinal center in mature TLS and at the center  
338 of involuted TLS, and a CD4<sup>+</sup>CXCR3<sup>-</sup> T helper (Th\_CXCR3<sup>low</sup>) clusters. In location and marker  
339 expression, Tph in these data were consistent with CD4<sup>+</sup> Tph that have been identified in patients  
340 with autoimmune disease, where they are thought to play a T follicular helper (Tfh)-like role in  
341 promoting pathogenic B cell responses in non-lymphoid tissue.<sup>33-35</sup> In contrast to changes  
342 observed in the B cell compartment, no significant difference was observed in density of CD4<sup>+</sup> T  
343 cell clusters or the cytotoxic Tc cluster.

344  
345 Clustering analysis also identified a CD4<sup>+</sup>CD57<sup>+</sup> cluster (Th\_CD57<sup>+</sup>) within the germinal center of  
346 mature TLS, which may provide help to B cells and induce class switch recombination,<sup>36-38</sup> a  
347 cluster of CD4<sup>+</sup>FOXP3<sup>+</sup> regulatory T cells (Th\_FOXP3<sup>+</sup>), a cluster of cytotoxic T cells (Tc); CD4<sup>+</sup>  
348 and CD8<sup>+</sup> T cells defined by high expression of granzyme B (GZMB<sup>+</sup> T cell); proliferating T and B  
349 cells defined by high expression of Ki67 (Proliferating T and B); a macrophage cluster with high  
350 expression of CD68; a mature dendritic cell cluster defined by the presence of high expression of  
351 DCLAMP and CCR7<sup>39</sup>; a high endothelial venule (HEV) cluster defined by expression of the  
352 protein peripheral node addressin (PNA<sup>d</sup>); and a tumor cluster with high expression of Cytokeratin  
353 (CK) and PDL1. In mature TLS compared to involuted TLS, there was significantly higher density  
354 of proliferating T and B cells ( $P = 0.022$ ), HEV ( $P = 0.00028$ ), and tumor ( $P = 0.0026$ ). On the  
355 other hand, density of mature dendritic cells was increased in involuted TLS ( $P = 0.025$ ).

356  
357 To further evaluate the spatial relationships between different cell types in the mature and  
358 involuted morphologies, we performed nearest neighbor analysis of the top 2 most frequent cell  
359 neighbors for each cell cluster (**Fig. 3g**). As in previous the above analyses, neighborhood  
360 analysis showed that the primary differences in spatial relationships between the two  
361 morphologies occurred in B cell clusters. In particular, in the mature morphology BCL6<sup>high</sup> germinal  
362 center B cell cluster were first and second nearest neighbors for themselves, consistent with a  
363 highly concentrated germinal center. In contrast, in the involuted TLS morphology the most  
364 common first neighbor of this cluster was the BCL6<sup>low</sup> cluster, consistent with a more dispersed  
365 germinal center in the involuted TLS. On the other hand, Tph were the most common non-self



366 neighbors for GZMB T cells, mature dendritic cells, proliferating T cells, and FOXP3<sup>+</sup> Tregs in  
367 both mature and involuted TLS, suggesting that the spatial relationships of these clusters was  
368 preserved across the two morphologies despite changes occurring in the B cell germinal center.  
369 Network analysis, which we used to visualize the average distances between cell clusters and  
370 cell cluster abundance across the two TLS morphologies, demonstrated similar changes to the  
371 two B cell clusters (B\_BCL6<sup>high</sup> and B\_BCL6<sup>low</sup>) occupying the germinal center and preservation  
372 of spatial relationships between mature dendritic cells, Tph, FOXP3<sup>+</sup> T cells, proliferating T and  
373 B cells, and GZMB<sup>+</sup> T cells in mature and involuted TLS (**Fig. 3h**). Overall, these neighborhood  
374 and network analyses suggested that while the B cell germinal center appeared to undergo  
375 dissolution in involuted TLS, the T cell zone was preserved.

376  
377 Finally, evaluation of individual marker expression by cluster supported these observations  
378 regarding persistence of the T cell zone (**Fig. 3i**). In the mature dendritic cell cluster, expression  
379 of CCR7, HLADR, and CD86 were significantly increased, implying ongoing antigen presentation  
380 in these structures, and both the Tph and Tc clusters demonstrated increased expression of  
381 markers of antigen experience, including CD45RO, CD25, PD1, and TOX expression. While the  
382 precise role of TOX in T peripheral helper cells is not established, TOX2 has previously been  
383 shown to be involved in the establishment of durable GC Tfh memory.<sup>40</sup> Taken together, these  
384 data suggest that the involuted morphology may be a site of persistent antigen presentation by  
385 mature dendritic cells, which drive the formation of antigen-experienced memory T cell  
386 populations.

### 387 388 **Expanded T cell clonotypes are shared across TLS within a tumor, while B cell repertoires** 389 **of individual TLS are highly distinct**

390  
391 Based on these data, we next sought to determine whether there were differences in the T and B  
392 cell repertoires of TLS of these two morphologies. We microdissected 38 individual TLS (32  
393 mature and 6 involuted) from 7 treated tumors and performed bulk sequencing using the Adaptive  
394 ImmunoSEQ TCR $\beta$  and IGH assays (**Fig. 4a, Extended Data Fig. 7a, Extended Data Table 9**).  
395 After filtering to remove repertoires with low counts, 35 TCR $\beta$  repertoires and 32 IGH repertoires  
396 were analyzed. Across all samples, the repertoire size was variable with a mean total TCR $\beta$   
397 clonotypes of 7171 $\pm$ 8472 (**Extended Data Fig. 7b**). Singleton clonotypes comprised 68.7 $\pm$ 13.4%  
398 of the TCR $\beta$  repertoire in all TLS sampled. In mature TLS, singleton clonotypes comprised  
399 72.02 $\pm$ 9.83% of the T cell repertoire, while in involuted TLS the singleton compartment constituted  
400 48.98 $\pm$ 16.1%. Across TLS microdissected from the same tumors, a mean of 32.3 $\pm$ 12.3% of  
401 unique TCR $\beta$  clonotypes could be identified in other TLS from the same tumor. TCR $\beta$  clonotypes  
402 identified in all TLS from the same tumor were highly expanded, while those found in only one  
403 TLS were predominantly singletons (**Fig. 4b-c and Extended Data Fig. 7c-h**), suggesting a high  
404 degree of T cell trafficking as well as significant local T cell repertoire diversity at each individual  
405 TLS.

406  
407 Across all microdissected TLS, the mean total number of IGH clonotypes was 922 $\pm$ 1188  
408 (**Extended Data Fig. 8a**). Singleton clonotypes comprised 95.3 $\pm$ 3.9% of IGH repertoire of all TLS  
409 sampled. In mature TLS, singleton clonotypes comprised 95.7 $\pm$ 4.0% of the IGH repertoire, while  
410 in involuted TLS the singleton compartment constituted 93.4 $\pm$ 3.1%. IGH repertoire sharing was  
411 significantly lower across TLS microdissected from the same tumor ( $P = 7.6e-15$ ), with only  
412 6.7 $\pm$ 5.6% of unique IGH clonotypes of each TLS detected in other TLS from the same tumor (**Fig.**  
413 **4d-f and Extended Figure 7b-g**). These B cell repertoire characteristics are consistent with highly  
414 distinct, independent germinal center reactions.

415

416 In three patients (P12, OT1, and OT6) in which mature and involuted TLS were present in the  
417 same tissue block, we compared the immune repertoires of these two morphologies. TCR $\beta$   
418 clonality was significantly increased in mature TLS compared to involuted TLS ( $P = 0.023$ ) (**Fig.**  
419 **4g**), although this difference was primarily observed in a single patient OT6 (**Extended Data Fig.**  
420 **7i**). No difference was observed in IGH clonality (**Extended Data Fig. 7g**), but the IGH repertoire  
421 of involuted TLS did demonstrate a significantly higher number of V gene substitutions, a  
422 surrogate for somatic hypermutation ( $P < 2.22e-16$ ) (**Fig. 4h** and **Extended Fig. 8i**). Taken  
423 together, these comparisons suggest that B cell populations in involuted TLS have undergone  
424 greater antigen-driven positive selection, consistent with a late-stage germinal center, and that  
425 there is associated T cell repertoire contraction and clonal expansion at these structures.

426  
427 Given the extensive sharing of expanded T cell clonotypes observed within TLS from the same  
428 tumor, we also evaluated the peripheral blood to determine the extent of T cell trafficking between  
429 TLS and peripheral blood. We performed TCR $\beta$  sequencing of pre- and post-treatment peripheral  
430 blood mononuclear cells from 5 of the 7 patients whose TLS were microdissected. In TLS from  
431 these 5 patients, a mean of  $44.0 \pm 8.4\%$  of unique TCR $\beta$  clonotypes and  $52.7 \pm 8.5\%$  of total  
432 clonotypes in TLS were also identified in post-treatment peripheral blood. Similar overlap was  
433 observed between TLS repertoires and pre-treatment peripheral TCR $\beta$  repertoires, where a mean  
434 of  $40.4 \pm 11.5\%$  of unique TCR $\beta$  clonotypes and  $48.7 \pm 11.0\%$  total clonotypes in TLS were  
435 identified in pre-treatment peripheral blood (**Extended Data Fig. 9a-b**). In 3 of the 5 patients, 13  
436 unique TCR $\beta$  were significantly expanded after neoadjuvant treatment and 9/13 (69.2%) were  
437 detected in at least one TLS (**Extended Data Table 10**). Together, these data provide evidence  
438 for a high degree of overlap between T cells within TLS and T cells in the peripheral blood.

439  
440 **The top expanded T cell clonotypes in mature TLS are cytotoxic granzyme K and granzyme**  
441 **B-expressing CD8<sup>+</sup> T cells**

442  
443 To further characterize T and B cell populations identified in TLS, we performed single cell  
444 RNA/TCR/BCR sequencing of post-treatment peripheral blood from the 7 patients from whose  
445 tumors TLS were microdissected. Sequencing of tumor infiltrating lymphocytes (TIL) was also  
446 performed for all 7 patients, but in only one sample (patient OT6) was sequencing data of sufficient  
447 quality for further analysis. Peripheral blood and TIL samples were processed by fluorescence-  
448 activated cell sorting (FACS) after labeling with antibodies to CD3 and CD19. After pre-processing  
449 and filtering to remove low quality sequencing data, 28,694 single cells were identified in the  
450 peripheral blood and 620 in the TIL. After performing preliminary cluster annotation using a  
451 reference annotated dataset, we attempted to match the TCR $\beta$  and IGH CDR3 amino acid  
452 sequences identified in microdissected TLS with sequences identified in the single cell dataset.  
453 TCR $\beta$  in the microdissection and single cell datasets were successfully matched (described  
454 below), but no matching IGH were identified between the bulk sequencing performed on  
455 microdissected TLS and single cell sequencing data, therefore B cells were excluded from  
456 subsequent analysis.

457  
458 The resultant 23,172 T cells in the post-treatment peripheral blood samples and 562 T cells in the  
459 TIL of patient OT6 were clustered into 16 distinct cell clusters based on expression of canonical  
460 genes associated with specific T cell subsets. The CD4 compartment of the single cell dataset  
461 was divided into a naïve CD4<sup>+</sup> T cell cluster (CD4 Naïve) expressing high levels of *CCR7* and  
462 *LEF1*; a CD4 Naïve-like cluster (CD4 Naïve-like) characterized by expression of *CCR7* and *TCF7*;  
463 a CD4 T central memory cluster (CD4 TCM) with high expression of *LTB* and *S100A4*; a CD4 T  
464 peripheral helper cluster (Tph) characterized by low expression of *CXCR5*, high expression of  
465 *CXCR3*, and high expression of *ICOS*; and two CD4 T effector memory clusters notable for high  
466 expression of granzyme K (CD4 TEM\_GZMK) and granzyme B (CD4 TEM\_GZMB). CD8 T cells

467 were divided into the following clusters: a naïve cluster (CD8 Naïve) highly expressing *CD8B*,  
468 *CCR7*, *LEF1*; a CD8 T central memory cluster (CD8 TCM) with elevated expression of *CD8B* and  
469 *LINC02446*; two CD8 T effector memory clusters distinguished by high expression of granzyme  
470 K (CD8 TEM\_GZMK) and high expression of granzyme B (CD8 TEM\_GZMB); and a CD8 tissue  
471 resident memory-like cluster (CD8 TRM) with increased expression of *NR4A2*, *DUSP2*, and  
472 *ZNF683*. In addition, we identified a CD4 regulatory T cell cluster (Treg) with high expression of  
473 *FOXP3* and *RTKN2*; an NK-T cell cluster (NK-T) highly expressing *PRF1* and *GZMB*; a double  
474 negative T cell cluster (dnT) with high expression of *SYNE* and *MALAT1*; a gamma delta T cells  
475 (gdT) with high expression of *TRDV2* and *TRGV9*; and mucosal invariant T cells cluster (MAIT)  
476 highly expressing *KLRB1* and *SLC4A10* (**Fig. 5a-c** and **Extended Data Fig. 10a-b**). In the TIL  
477 of patient OT6, 11 of 16 clusters were identified: CD4 Naïve-like, CD4 TCM, CD4 Tph, CD4  
478 TEM\_GZMK, CD8 TCM, CD8 TEM\_GZMK, CD8 TEM\_GZMB, CD8 TRM, Treg, dnT, and MAIT  
479 (**Extended Data Fig. 11a-c**).

480  
481 19,546/23,172 (84.3%) single cells in the peripheral blood dataset and 346/562 (61.6%) cells in  
482 the TIL had a partial or completely sequenced TCR $\alpha\beta$  chain identified by single cell TCR  
483 sequencing, of which there were 15,016 and 256 unique TCRs, respectively (**Extended Data**  
484 **Table 11**). In the peripheral blood single cell dataset, clonal expansion was most strongly  
485 associated with the CD4 TEM\_GZMB (Odds Ratio 31.48,  $P < 0.001$ ) and CD8 TEM\_GZMB  
486 clusters (Odds Ratio 17.99,  $P < 0.001$ ) by Fisher's Exact test (**Fig. 5d** and **Extended Data Table**  
487 **12**). In TIL, clonal expansion was most strongly associated with the CD8 TEM\_GZMB (Odds Ratio  
488 3.49,  $P = 0.003$ ), CD8 TRM (Odds Ratio 2.57,  $P = 0.041$ ), and CD8 TEM\_GZMK (Odds Ratio  
489 1.94,  $P = 0.013$ ) clusters (**Extended Data Fig. 11d** and **Extended Data Table 12**).

490  
491 T cells belonging to the CD8 TEM\_GZMK cluster were notable for increased expression of the  
492 gene associated with cytotoxicity, including Granzyme K (*GZMK*) and the chemokine ligand *CCL5*  
493 (*CCL5*) and decreased expression of Granulysin (*GNLV*). The CD8 TEM\_GZMB clusters also  
494 demonstrated hallmarks of cytotoxicity, including elevated expression of granzyme B (*GZMB*) and  
495 granzyme H (*GZMH*), as well as elevated expression of perforin (*PRF1*), and *GNLV* (**Extended**  
496 **Data Fig. 10c-d**).<sup>41</sup> *GZMK* expression was low in the latter cluster. These two transcriptional  
497 phenotypes were consistent with T progenitor exhausted and cytotoxic/terminally differentiated  
498 CD8 T cell states, respectively, which have been previously identified in the peripheral blood and  
499 tumors of patients treated with ICB.<sup>41</sup> Consistent with this identity, in the TIL from patient OT6,  
500 both *GZMK* and *GZMB* expressing CD8 clusters showed increased expression of multiple T cell  
501 exhaustion markers, including *PDCD1*, *CTLA4*, *LAG3*, *TIGIT*, and *TOX*, which were more highly  
502 expressed in CD8 TEM\_GZMB compared to CD8 TEM\_GZMK. *NKG7* and *CCL5*, which are  
503 associated with cytotoxic CD8 T cells, were also increased in both clusters, with higher expression  
504 in the GZMB high cluster (**Extended Data Fig 11h-i**). Notably, both clusters in the single cell TIL  
505 from patient OT6 demonstrated elevated expression of the B cell chemoattractant *CXCL13*, which  
506 has been associated with tumor-specific T cells in single cell sequencing studies of TIL from  
507 patients treated with ICB and is involved in the formation of TLS.<sup>42,43</sup>

508  
509 No CD4<sup>+</sup> T cell cluster was observed in the single cell data that displayed a transcriptional  
510 phenotype consistent with a CD4<sup>+</sup> T follicular helper (Tfh) population, which are defined by high  
511 expression of *CXCR5*, *CXCR3*, and *ICOS*. Instead, we identified a CD4<sup>+</sup> T cell cluster consistent  
512 with the T peripheral helper cluster identified by imaging mass cytometry. In the peripheral blood,  
513 cells belonging to this cluster demonstrated low *CXCR5* expression, increased *CXCR3*  
514 expression, and elevated expression of *CTLA4*, *TIGIT*, and *TOX* (**Extended Data Fig. 10e**). Cells  
515 belonging to this cluster in the single cell TIL demonstrated increased expression of *CXCL13*,  
516 *ICOS*, *PD1*, *MAF*, *TOX* and high expression of multiple exhaustion markers including *CTLA4*,  
517 *LAG3*, *TIGIT*, *HAVCR2*, and *TNFRSF18* (*GITR*) (**Extended Data Fig 11j**). Based on these data

518 and the imaging mass cytometry above, we conclude that Tph constitute a major CD4<sup>+</sup> T cell  
519 subset found in TLS in the context of neoadjuvant immunotherapy.

520  
521 Approximately one-third, or 6349/19546 (32.5%), of single cells with a TCR $\beta$  in the peripheral T  
522 cell dataset and 199/346 (77.7%) single cells with a TCR $\beta$  in the TIL were identified in at least  
523 one TLS (**Extended Data Table 11**). TCR $\beta$  identified in TLS were detected in all clusters of the  
524 peripheral and TIL single cell dataset. Among peripheral blood T cells, the clusters most strongly  
525 associated with TLS were CD4 TEM\_GZMB (Odds Ratio 10.72, P < 0.001), CD8 TEM\_GZMB  
526 (Odds Ratio 9.73, P < 0.001), and CD8 TEM\_GZMK (Odds Ratio 9.46, P < 0.001) (**Fig. 5e-f** and  
527 **Extended Data Table 13**), suggesting that TLS specifically promote the trafficking of effector  
528 memory CD4<sup>+</sup> and CD8<sup>+</sup> T cell populations from the peripheral blood to tumor. In the TIL, no  
529 cluster was significantly correlated with TLS but the Treg cluster was inversely correlated with  
530 presence in TLS (Odds Ratio 0.22, P = 0.003) (**Extended Data Fig. 11e-f** and **Extended Data**  
531 **Table 13**). The proportion of all TCR $\beta$  identified in TLS that were matched to single cell data was  
532 low overall (2,908/135,909 unique clonotypes or 2.1%), but a higher proportion of clonotypes were  
533 successfully matched for the most expanded clones, with 369/1359 (27.2%) of the top 1% of  
534 TCR $\beta$  that had been identified in TLS being successfully matched to the single cell data, and  
535 63/137 (46%) of the top 0.1% of TCR $\beta$  (**Extended Data Table 14**). Thus, this approach, while  
536 providing a limited view of singleton TCR $\beta$  identified in TLS, could be used to provide additional  
537 transcriptional information about expanded T cell populations trafficking to TLS.

538  
539 We next used these data to infer the transcriptional phenotype of T cells trafficking through TLS.  
540 Since our single cell dataset contained peripheral blood and TIL data, we first evaluated the  
541 correlation between peripheral blood and TIL phenotypes, and the reliability of using data from  
542 single cell sequencing from one compartment to infer the properties of single cells with the same  
543 TCR $\beta$  in the other compartment. To carry this out, we examined the correlation between single  
544 cell cluster identity for TCR $\beta$  which were found in both peripheral blood and TIL in patient OT6. In  
545 total, 16 unique TCR $\beta$  sequences were present in both peripheral blood and TIL (**Extended Data**  
546 **Fig. 11a**). 7/16 TCR $\beta$  clonotypes had the same single cell identity for all cells with the same TCR $\beta$   
547 in the peripheral blood and TIL, and an additional 5/16 TCR $\beta$  had the same cluster identity  
548 assigned to at least half of the cells in both peripheral blood and TIL. In only 4/16 TCR $\beta$  were the  
549 cluster identities of cells with the same TCR $\beta$  entirely discordant (**Extended Data Fig. 11b**).  
550 Based on these data, we concluded that the peripheral blood transcriptional phenotype closely  
551 recapitulates the cluster assignment of TIL, and thus both identities may be used to determine a  
552 putative phenotype for T cells identified in TLS by TCR $\beta$  sequencing. These findings were  
553 consistent with previous work demonstrating that in circulating TILs, gene signatures of effector  
554 functions, but not terminal exhaustion, reflect those observed in the tumor.<sup>44</sup>

555  
556 Across all 7 patients, the majority of T cells identified by matching of the TCR $\beta$  were GZMK and  
557 GZMB expressing CD8 T effector memory cells, but we also observed CD4 TEM\_GZMK, CD4  
558 CTL, and CD4 T peripheral helper clusters among the putative phenotypes of T cells trafficking  
559 through TLS (**Fig. 5g**). Notably, in the involuted TLS from the tumor of patient OT6, where we had  
560 previously noted significant increase in clonality relative to mature TLS, clonal expansion was  
561 greatest in the of CD8 TEM\_GZMK, CD8 TEM\_GZMB, and CD8 TRM clusters (**Fig. 5h** and  
562 **Extended Data Fig. 11k**). Overall, these data provide single cell resolution to the top expanded  
563 clonotypes in TLS and show that highly expanded T cell populations in TLS are CD8<sup>+</sup> T cell  
564 effector memory, which may undergo clonal expansion and repertoire contraction in concert with  
565 expansion of resident memory populations in areas of tumor regression.

566  
567 **DISCUSSION**

568

569 Neoadjuvant immunotherapy aims to use the primary tumor as a source of antigens to enhance  
570 antitumor immunity and prevent cancer recurrence after surgery.<sup>4</sup> Preclinical and clinical data  
571 suggest that this approach induces more durable immunologic memory than adjuvant  
572 immunotherapy alone,<sup>3</sup> but the mechanism by which this occurs and the contribution of TLS to  
573 this process are not well understood. The data presented here show that in HCC treated with  
574 neoadjuvant immunotherapy, intratumoral TLS are associated with superior pathologic responses  
575 and improved relapse free survival. These findings are consistent with data reported in other solid  
576 tumors treated with ICB,<sup>9-12</sup> as well as studies of the prognostic significance of intratumoral TLS  
577 in treatment-naïve early stage HCC treated with surgical resection.<sup>16</sup> In tumors with high TLS  
578 density and significant regression of the tumor, we further identified an involuted morphology of  
579 TLS in areas of nonviable tumor whose location, histologic, and immunologic features, and  
580 similarity to late stage germinal centers observed in murine secondary lymphoid organs,<sup>26</sup> are  
581 consistent with a terminal stage of the TLS life cycle. Using laser capture microdissection, bulk  
582 immune repertoire sequencing, and matched single cell sequencing, we identify and characterize  
583 expanded T cell populations trafficking through TLS and find evidence for significant immune  
584 repertoire changes associated with TLS dissolution.

585  
586 While TLS are thought to mature from a loosely organized lymphoid aggregate to a CD21<sup>+</sup> primary  
587 follicle and reach full maturity as a CD21<sup>+</sup>CD23<sup>+</sup> secondary follicle,<sup>16,45,46</sup> which have distinct T  
588 and B cell zones,<sup>25</sup> the circumstances of TLS resolution are not known.<sup>47</sup> These data suggest that  
589 TLS dissolution may be driven by elimination of tumor and may occur dyssynchronously, with  
590 dissolution of the B cell germinal center accompanied by persistence of a T cell zone enriched for  
591 interactions between DCLAMP<sup>+</sup>CCR7<sup>+</sup>HLADR<sup>+</sup> mature dendritic cells and CD4<sup>+</sup> and CD8<sup>+</sup> T cells.  
592 Furthermore, the changes observed in T cell repertoire at these structures, including increase in  
593 clonality and expansion of cytotoxic and tissue resident memory-like CD8<sup>+</sup> T cell clonotypes,  
594 suggest that late-stage TLS may play a functional role in supporting the contraction and memory  
595 phase of the intratumoral adaptive immune response through persistent antigen presentation in  
596 the T cell zone (**Fig. 6**). Such a role would also be consistent with recent data suggesting that  
597 tonic antigenic stimulation drives programs of T cell residency in tumors, and would identify a  
598 specific place where such interactions may occur.<sup>48</sup>

599  
600 Notably, in neoadjuvant treated tumors we did not detect a CXCR5<sup>+</sup>CXCR3<sup>+</sup>CD4<sup>+</sup> T follicular  
601 helper population, which have been reported in tumor associated TLS.<sup>49,50</sup> Rather, in both the  
602 imaging mass cytometry analysis and single cell datasets we identified a CXCR5<sup>+</sup>CXCR3<sup>+</sup> CD4<sup>+</sup>  
603 T cell population, which expressed CXCL13 in the single cell TIL of patient OT6 and was also  
604 detectable in post-treatment peripheral blood single cell sequencing. CXCR5<sup>+</sup>CXCL13-producing  
605 CD4<sup>+</sup> T cells have been identified in untreated human breast cancer under the name TFHX13<sup>51,52</sup>  
606 and in autoimmune disease, where they are termed CD4<sup>+</sup> T peripheral helper cells and have been  
607 shown to provide help to B cells in an IL-21 dependent manner.<sup>34,35,53</sup> This population was present  
608 in both the mature and involuted morphologies observed in these patients. Additional studies are  
609 required to determine whether this population of CD4<sup>+</sup> T cells provides help to B cells in this  
610 treatment setting, and to determine their role in involuted TLS, where they were found in  
611 association with mature dendritic cells.

612  
613 We recognize several limitations of the findings reported here. First, samples were obtained from  
614 a single institution and may not represent the full diversity of HCC etiologies and subtypes.  
615 Additionally, while the untreated cohort in this study was similar to the treatment cohort in age,  
616 sex, and HCC etiology and received treatment at the same primary institution, we cannot exclude  
617 the possibility that the different pathologic findings between the untreated and neoadjuvant  
618 cohorts arose as a consequence of differences in the patient populations rather than treatment  
619 status. We infer the transcriptional phenotype of T cells infiltrating TLS based on matching TCRs

620 identified by microdissection with peripheral T cells and/or TIL subjected to single cell sequencing.  
621 In our data, we demonstrate a correlation between the cluster identity for 16 TCRs shared  
622 between the peripheral blood and TIL of patient OT6, and others have reported correlation  
623 between gene signatures of effector functions in circulating TILs and tumor;<sup>44</sup> however, it is  
624 possible that the phenotype of these T cells are not fully conserved outside of TLS. Finally, our  
625 analyses throughout are limited by small sample size. However, clinical samples from  
626 neoadjuvant studies are rare, and as we have shown here even small samples can provide  
627 important insights into the constituent immune populations in tumors arising in human subjects.

628  
629 Finally, these data raise several important questions which future studies should address. First,  
630 the role of FOXP3<sup>+</sup> T follicular regulatory cells, which have been shown to regulate germinal  
631 center reactions,<sup>54,55</sup> is not completely understood in this context and this population could not be  
632 resolved in our imaging mass cytometry analysis. Second, while dispersion of the B cell follicle  
633 was associated with attenuation of the PDPN<sup>+</sup> fibroblastic reticular cell and the CD21<sup>+</sup>CD23<sup>+</sup>  
634 follicular dendritic cell network in our data, other changes occurring in the fibroblast populations  
635 involved in this process remain unclear and it is not known what permits retention of mature  
636 dendritic cells within the T cell zone. Third, since all tumors in which involuted TLS were observed  
637 were treated with neoadjuvant ICB and these structures were not seen in untreated tumors, the  
638 contribution of therapy to their formation cannot be established from our data. In murine studies,  
639 both the PD-1 and CTLA-4 pathways have been shown to be involved in regulation of T follicular  
640 regulatory populations,<sup>56-58</sup> suggesting that therapeutic blockade may affect the dynamics of  
641 germinal center formation and dissolution. Nonetheless, these data shed light on the  
642 circumstances of TLS resolution and suggest that this terminal stage, about which nothing was  
643 previously known, may play a functional role in the formation of intratumoral T cell memory after  
644 elimination of viable tumor.

## 645 646 **METHODS**

### 647 648 **Study design**

649 The aim of this study was to characterize tertiary lymphoid structures (TLS) in patients with  
650 hepatocellular carcinoma (HCC) treated with neoadjuvant ICB-based therapy prior to surgical  
651 resection of the primary tumors. To understand the clinical significance of TLS, we analyzed TLS  
652 density in treated patients and untreated controls and correlated TLS density in treated patients  
653 against pathologic response and post-surgical clinical outcomes. We performed bulk RNA  
654 sequencing of tumors with high and low TLS density after neoadjuvant treatment to understand  
655 the gene expression programs of tumors with high TLS density. We then characterized the  
656 morphological and functional properties using bulk immune repertoire sequencing of TCR $\beta$  and  
657 IGH, imaging mass cytometry, matched single cell TCR and RNA sequencing of peripheral blood  
658 and tumor infiltrating lymphocytes.

### 659 660 **Patient identification and data collection**

661 Patients were identified for inclusion in this study if they received surgical resection for locally  
662 advanced, non-metastatic hepatocellular carcinoma after neoadjuvant ICB-based therapy  
663 between October 1, 2019 and January 31, 2022 at the Johns Hopkins Sidney Kimmel Cancer  
664 Center. Retrospective chart review was performed to collect clinical data from the electronic  
665 medical record regarding age at surgery, sex, date of resection, HCC etiology, histologic grade of  
666 tumor, neoadjuvant treatment, relapse free survival, and overall survival. A cohort of untreated  
667 control patients who had undergone surgical resection for HCC without prior systemic treatment  
668 were also identified via a search of the electronic medical record. Review of the electronic medical  
669 record was performed to confirm absence of prior systemic treatment. For both cohorts, histologic  
670 grade was based on pathologic assessment at the time of resection if there was discordance with

671 grade reported for pre-treatment biopsy. Patients in both cohorts were excluded from analysis if  
672 there was evidence of active hepatitis B (defined by a positive HBsAg or detectable HBV DNA)  
673 prior to surgery. Patients were excluded from the control group if the etiology of their HCC was  
674 not represented in the treatment group (e.g. hepatic adenoma and hereditary hemochromatosis).  
675 This study was conducted in accordance with the Declaration of Helsinki and was approved by  
676 the Johns Hopkins University Institutional Review Board (IRB00149350, IRB00138853,  
677 NA\_00085595). Informed consent or waiver of consent was obtained from all patients. Treated  
678 patients identified with the letter P were accrued as participants in the phase I clinical trial  
679 NCT03299946.<sup>8</sup>

680

### 681 **Histopathologic assessment of TLS density and pathologic response**

682 Evaluation of pathologic response was performed by a hepatopathologist (RA). Pathologic  
683 response designations were assigned according to percent residual viable tumor in surgically  
684 resected tumors. Complete response (CR) was defined as 0% residual viable tumor, major  
685 pathologic response (MPR) as less than 10% residual viable tumor, partial pathologic response  
686 (pPR) as 10-90% residual viable tumor, and non-response (NR) as >90% residual viable tumor.<sup>17</sup>  
687 12 of the 19 patients had previously undergone assignment of pathologic response according  
688 binary categorization of major or complete pathologic response versus non-response,<sup>8</sup> and for  
689 this group non-responders were categorized as NR or pPR as described above. To determine  
690 TLS density, formalin fixed paraffin embedded (FFPE) tumors were sectioned, mounted on glass  
691 slides, and stained with anti-CD20 antibody as described below. Whole slide images were  
692 obtained at 0.49  $\mu\text{m}$  per pixel using the Hamamatsu NanoZoomer. The presence of CD20  
693 positivity was determined by digital image analysis software (HALO v3.0.311 Indica Labs), with  
694 TLS defined as CD20 positive cell aggregates greater than 150 $\mu\text{m}$  in diameter located among  
695 tumor cells or at the invasive margin in areas of viable and nonviable tumor. TLS density was  
696 determined by calculating the number of TLS per  $\text{mm}^2$  of viable and nonviable tumor. TLS were  
697 classified as peritumoral if they were found within 200  $\mu\text{m}$  of the interface between normal  
698 adjacent parenchyma and tumor and intratumoral if they were found within the tumor or tumor  
699 regression bed.

700

### 701 **Survival analyses**

702 The Kaplan–Meier method was used to estimate relapse-free survival (PFS) and overall survival  
703 (OS). Relapse free survival (RFS) was defined as the time from surgical resection to radiographic  
704 relapse. Overall survival (OS) was defined as the time from surgical resection to death from any  
705 cause. If a patient was not known to have had either event, RFS and OS were censored at the  
706 last date of known healthcare contact. RFS and OS analyses were limited to patients treated with  
707 neoadjuvant therapy and were not performed in the untreated controls due to limited follow up in  
708 this cohort. Survival analyses using the Kaplan-Meier method were performed using the R  
709 package survminer. Bayesian information criterion (BIC) analysis was performed using the R  
710 package stats. A linear regression model was used to evaluate the effect of each marker,  
711 dichotomized by the mean, as a predictor of each distance measure. For each binary outcome,  
712 logistic regression was employed, with each marker treated as continuous. A meaningful  
713 difference in BIC between the two models is 2 at a minimum, and a difference between 5-10 and  
714 above 10 is considered to be strong and very strong, respectively.<sup>59</sup>

715

### 716 **Immunohistochemistry**

717 Automated single and dual staining was performed on the Leica Bond RX (Leica Biosystems).  
718 Single staining for CD20 was employed for determination of TLS density. Dual staining for CD3  
719 and CD21, CD8 and CD4, Ki67 and CD20 was performed prior to laser capture microdissection  
720 of TLS. Slides were baked and dewaxed online followed by antigen retrieval for 20 min at 100°C.  
721 Endogenous peroxidase was blocked using Peroxidase block (Refine Kit) followed by Protein

722 block (X090930-2, Agilent Technologies Inc., Santa Clara, CA). Primary antibodies were applied  
723 at room temperature. Detection was performed using the Bond Polymer Refine Kit (DS9800, Leica  
724 Biosystems). For dual staining, a second round of antigen retrieval was performed for 20 min at  
725 95°C followed by application of a second primary antibody. Detection of the second primary  
726 antibody was performed using the Bond Polymer Red Refine Kit (DS9390, Leica Biosystems).  
727 Slides were counterstained, baked and coverslipped using Ecomount (5082832, Biocare Medical,  
728 Walnut Creek, CA). Antigen retrieval buffers and concentrations of all antibodies are listed in  
729 **Extended Data Table 15**. Antibodies were diluted to appropriate working concentration using  
730 Antibody Diluent (S302283-2, Agilent Technologies Inc).

731

### 732 **Bulk RNA sequencing and TCR $\beta$ /BCR immune repertoire profiling of FFPE tumor**

733 RNA was extracted from FFPE tumor from the treatment cohort and sequenced using the  
734 commercial platform Immunoid NeXT with 200 million paired end reads (150 base pair). Reads  
735 were aligned in accordance with the Personalis Cancer RNA pipeline and transcript per million  
736 (TPM) values were extracted.<sup>60</sup> Bulk RNA sequencing was performed on 14 tumors in two  
737 batches. No batch correction was applied due to lack of clear batch-to-batch differences by  
738 principal component analysis. 2 samples were excluded due to poor sequencing depth, as defined  
739 by a median of the log<sub>2</sub> transformed count data being equal to 0 for those samples. The remaining  
740 12 samples were filtered to include only genes for which the sum of raw counts across all samples  
741 was greater than 1. Variance stabilizing transformation was performed on the resultant data and  
742 differentially expressed genes were identified using DESeq2.<sup>61</sup> Genes with an adjusted P value  
743 of < 0.05, and a minimum log<sub>2</sub> fold change of 1 were considered differentially expressed. Pathway  
744 analysis was performed using the R package fsgsea to identify biologically enriched pathways  
745 from the MSigDB hallmark gene sets.<sup>62,63</sup> For pathway analyses, adjusted P values of < 0.05 were  
746 considered statistically significant. TCR $\beta$  and BCR repertoire profiling was performed using the  
747 Immunoid NeXT transcriptome, which provides augmented (approximately a 100x increase over  
748 a standard transcriptome) coverage of TCR $\beta$  and BCR.<sup>60,64</sup> Clones were identified using MiXCR<sup>65</sup>  
749 and repertoire analysis was performed using the R package immunarch.<sup>66</sup> Clonality was  
750 calculated as 1-Shannon's equitability<sup>67</sup> with clonality values ranging from 0-1, with 0 indicating  
751 equal representation of all clones within a repertoire and 1 being a repertoire consisting of only  
752 one clone.

753

### 754 **IMC staining and acquisition**

755 IMC Staining was done as previously described.<sup>8,68</sup> Briefly, formalin-fixed paraffin-embedded  
756 (FFPE) resected liver tissue sections were baked, deparaffinized in xylene, then rehydrated in an  
757 alcohol gradient. Slides were incubated in Antigen Retrieval Agent pH 9 (Agilent PN S2367) at  
758 96 °C for 1 hour then blocked with 3% BSA in PBS for 45 min at room temperature followed by  
759 overnight staining at 4°C with the antibody cocktail. Antibodies, metal isotopes, and their titrations  
760 are listed in **Extended Data Table 8**. Images were acquired using a Hyperion Imaging System  
761 (Standard BioTools) at the Johns Hopkins Mass Cytometry Facility. Upon image acquisition,  
762 representative images were visualized and generated through MCD™ Viewer (Standard  
763 BioTools).

764

### 765 **IMC data analysis**

766 Images were segmented into a single-cell dataset using the publicly available software pipeline  
767 based on CellProfiler, ilastik, and HistoCAT.<sup>69-72</sup> Since multiple images contained more than one  
768 TLS, images were subset for distinct TLS regions by manual gating using FlowJo™v10.9.0  
769 Software (BD Life Sciences), which identified the xy coordinates of cells belonging to distinct  
770 lymphoid aggregates (**Extended Data Fig. 6b-c**). This resulted in 38 unique TLS matching either  
771 the mature ( $n = 20$ ) or involuted morphology ( $n = 18$ ). The resulting 61,371 single cells were  
772 clustered using FlowSOM<sup>73</sup> into metaclusters, which were manually annotated into final cell types.



773 Density of each cell type was determined by calculating the number of cells per unit area as  
774 determined by ImageJ v1.53.<sup>74</sup> For network visualization, the mean distance between each cell  
775 type was computed and visualized using the R package qgraph.<sup>75</sup> Neighborhood analysis was  
776 performed by using data generated by HistoCAT summarizing the top neighboring cell types for  
777 every cell type.

778

### 779 **Laser capture microdissection and TCR $\beta$ /IGH sequencing of microdissected TLS**

780 10-14  $\mu\text{m}$  serial tissue sections were obtained from formalin-fixed paraffin embedded (FFPE)  
781 tumor tissue blocks and mounted on UV activated PEN membrane glass slides (Applied  
782 Biosystems Cat. No. LCM0522) with additional 4- $\mu\text{m}$  tissue sections cut every 150  $\mu\text{m}$  for staining  
783 with hematoxylin and eosin (H&E) and dual IHC for CD3/CD21, CD8/CD4, and Ki67/CD20 as  
784 described above. Stained sections were scanned at 20x objective equivalent (0.49  $\mu\text{m pixel}^{-1}$ ) on  
785 a digital slidescanner (Hamamatsu Nanozoomer) in advance of microdissection and annotated  
786 using NDP.view2 viewing software in order to identify areas for microdissection. On the day of  
787 microdissection, unstained tissue sections mounted on PEN membrane slides were  
788 deparaffinized using xylene and graded alcohol washes and stained with H&E. Laser capture  
789 microdissection of individual TLS was performed on the LMD 7000 system (Leica) and genomic  
790 DNA was extracted using the Qiagen QIAamp DNA FFPE Tissue Kit following the manufacturer's  
791 protocol (Qiagen). DNA concentrations were quantified with a Qubit 4 Fluorometer using the Qubit  
792 dsDNA high sensitivity assay (Invitrogen). Sequencing of the TCR $\beta$  and IGH CDR3 regions was  
793 performed using the immunoSEQ platform (Adaptive Biotechnologies).<sup>76,77</sup> TCR $\beta$  and IGH  
794 repertoire data were downloaded from the Adaptive ImmunoSEQ analyzer web interface after  
795 filtering to remove non-productive reads. After exclusion of repertoires with fewer than 500 TCR $\beta$   
796 clones and 50 IGH clones, subsequent analysis was performed using the R package immunarch<sup>66</sup>  
797 and the Python package Change-O,<sup>78</sup> which was used to assign clonal families to IGH data. J  
798 gene, and greater than 90% identical CDR3 sequence according to nucleotide hamming distance.  
799 Clonality was calculated as described above using 1-Shannon's equitability. To compare clonality  
800 across multiple TLS from the same tumor, we used the median clonality of 1000 iterations of  
801 downsampling to the number of productive CDR3 sequences in the smallest TCR $\beta$  or IGH  
802 repertoire for that patient.<sup>79</sup>

803

### 804 **Peripheral blood and fresh tumor collection and processing**

805 Processing of peripheral and cryopreservation was completed as previously described.<sup>8</sup> Fresh  
806 tumor tissue was diced with a sterile scalpel and dissociated in 0.1% collagenase in RPMI 1640  
807 for 60 minutes at 37°C using the gentleMACS OctoDissociator (Miltenyi Biotec) according to the  
808 manufacturer's instructions. Supernatant was collected and centrifuged at 1500 rpm for 10  
809 minutes. Supernatant was removed and discarded, and the cell pellet was resuspended in ACK  
810 Lysing buffer (Quality Biological, cat# 118-156-721) and incubated at room temperature for 5  
811 minutes before centrifugation at 1500 rpm for 10 minutes. Cells were resuspended in PBS,  
812 counted using a manual hemacytometer, and cryopreserved in 10% DMSO/AIM-V freezing  
813 media.

814

### 815 **Single cell RNA/TCR/BCR-sequencing**

816 For all 7 patients from whose tumors TLS were microdissected, single cell sequencing was  
817 obtained for peripheral blood T and B cells isolated by Fluorescent Activated Cell Sorting (FACS).  
818 For 6 of 7 patients, the peripheral blood sample was obtained following completion of neoadjuvant  
819 ICB and prior to surgical resection; for 1 of the patients, the peripheral blood sample was drawn  
820 4 weeks after resection. In addition, in the latter patient, single cell sequencing was performed for  
821 tumor infiltrating T and B cells isolated by FACS from tumor specimen. Cryopreserved PBMC and  
822 tumor suspension were thawed and washed with pre-warmed RPMI with 10% FBS. Cells were  
823 resuspended 0.04% BSA in PBS and stained with a viability marker (Zombie NIR, BioLegend)

824 and Fc block (Biolegend, Cat. no. 422302) for 10 minutes at room temperature in the dark. Cells  
825 were then stained with antibodies against CD3 (FITC, clone HIT3a), for 20 minutes on ice and  
826 CD19 (PE/dazzle, clone SJ25C1) (**Extended Data Table 16**). After staining, viable CD3<sup>+</sup> and  
827 CD19<sup>+</sup> cells were sorted into 0.04% BSA in PBS using a BD FACS Aria II Cell Sorter at a 4:1  
828 ratio. Sorted cells were counted and resuspended at a concentration of 1000 cells per  $\mu$ l. The  
829 single-cell library preparations for gene expression and V(D)J were performed with the Chromium  
830 Next GEM Single Cell 5' GEM Kit v2 (10x Genomics) and Chromium Single Cell V(D)J  
831 Amplification Kit (human TCR) (10x Genomics), respectively. The cells were partitioned into  
832 nanoliter-scale Gel Beads in-emulsion (GEMs) and cells were barcoded. The cDNA synthesis  
833 and amplification was performed prior to sample split for the gene expression and for V(D)J  
834 libraries. Single cell libraries were sequenced on an Illumina NovaSeq instrument using 2 × 150-  
835 bp paired end sequencing. 5' VDJ libraries were sequenced to a depth of 5,000 reads per cell. 5'  
836 DGE libraries were sequenced to a depth of 50,000 reads per cell.

837

### 838 **Single cell data pre-processing, quality control, clustering and integration**

839 Cell Ranger v6.1.2 was used to demultiplex FASTQ reads, perform sequence alignment to the  
840 GRCh38 transcriptome, and extract unique molecular identifier (UMI) barcodes. Single cell gene  
841 expression matrices were analyzed using the R package Seurat v4.1.1 as a single Seurat object.  
842 Cells were filtered to include only cells with less than 25% mitochondrial RNA content and  
843 between 200 and 4000 genes detected. For single-cell VDJ sequencing, only cells with full-length  
844 sequences were retained. Raw count data were normalized using the Seurat function  
845 SCTransform to normalize raw count data to a Gamma-Poisson Generalized Linear Model,  
846 perform variance stabilization, identify highly variable features, and scale features.<sup>80,81</sup> Cells were  
847 projected into their first 50 principal components using the RunPCA function in Seurat, and further  
848 reduced into a 2-dimensional visualization space using the RunUMAP function. Initial cell cluster  
849 identification was performed using the Seurat function FindClusters at a resolution of 0.7. Initial  
850 cell type assignment was performed by reference mapping to the human PBMC dataset  
851 associated with the R package Azimuth.<sup>82</sup> Cluster identities were then manually assigned by  
852 identification of differentially expressed genes using the MAST hurdle model as implemented in  
853 the Seurat FindAllMarkers function with a log fold change threshold of 0.25 and minimum  
854 fractional expression threshold of 0.25.<sup>83</sup> Integration of single cell TCR-seq and BCR-seq data  
855 into the scRNA-seq data was performed using the R package scRepertoire.<sup>84</sup> For each patient,  
856 TCR $\beta$  sequences identified in single cell data were compared against TCR $\beta$  identified in  
857 microdissected TLS to identify T cells present in TLS. In cases where single cells with the same  
858 TCR occupied multiple clusters, a putative transcriptional phenotype was assigned to a T cell in  
859 the TLS repertoire according to the most common T cell subset to which the single cells with the  
860 same TCR belonged. No matches were identified between IGH sequences identified by Adaptive  
861 sequencing and IGH sequences in the single cell dataset, and thus we excluded B cells in the  
862 single cell dataset from further analysis.

863

### 864 **Data availability**

865 Bulk RNA-seq, single cell RNA/TCR-seq data, and imaging mass cytometry data from this study  
866 are deposited in dbGap under \*\*\* and the Gene Expression Omnibus (GEO) under accession  
867 number GSE \*\*\*. Bulk TCR $\beta$  and IGH data from microdissected TLS are available on the Adaptive  
868 ImmunoSEQ web analyzer portal at \*\*\*. All other relevant data are available from the  
869 corresponding authors upon request.

870

### 871 **Code availability**

872 All custom code used to generate the results in this study has been deposited in a GitHub  
873 repository at <https://github.com/FertigLab/HCC TLS>.

874

875 **Acknowledgements**

876 This work was supported by the Johns Hopkins SPORE in Gastrointestinal Cancer and the  
877 National Institutes of Health (NIH) U01CA253403 and U01CA212007 grants to M.Y. and E.J.F.  
878 Additional research support was provided by the Breeden-Adams Foundation and Conquer  
879 Cancer to M.Y.; the Johns Hopkins School of Medicine J. Mario Molina Physician Scientist Fund,  
880 Linda Rubin Fellowship, and Bernice Garchik Fellowship to D.S; and the Maryland Cancer  
881 Moonshot Research Grant to the Johns Hopkins Medical Institutions to D.J.Z. We thank  
882 Theinmozhi Arulraj for reviewing the final manuscript.

883

884 **Author contributions**

885 D.S., M.Y., and E.J.F. conceived and designed this study. D.S., L.K., M.Y., and L.D. performed  
886 data analysis and interpreted results. Q.Z. and R.A. performed the pathologic review. D.S., K.M.,  
887 Q.Z., and R.A. performed the histologic analysis. All authors assisted with the data analysis,  
888 provided valuable discussion, and reviewed and edited the final manuscript draft. D.S. and M.Y.  
889 wrote the manuscript with input from all the authors.

890

891 **Competing interests**

892 M.Y. reports grant/research support from Bristol-Myers Squibb, Incyte, Genentech (to Johns  
893 Hopkins) and honoraria from Genentech, Exelixis, Eisai, AstraZeneca, Replimune, Hepion, and  
894 equity in Adventris Pharmaceuticals. E.J.F is on the Scientific Advisory Board of  
895 Viosera/Reistance Bio, is a paid consultant for Merck and Mestag Therapeutics, and receives  
896 research funds from Abbvie. W.J.H. has received patent royalties from Rodeo/Amgen and is the  
897 recipient of grants from Sanofi, NeoTX, and CirclePharma. He has received speaking/travel  
898 honoraria from Exelixis and Standard BioTools. E.M.J. reports grant/research support from the  
899 Lustgarten Foundation, Break Through Cancer, Genentech, Bristol-Meyers Squibb; honoraria  
900 from Achilles, DragonFly, Parker Institute, Cancer Prevention and Research Institute of Texas,  
901 Surge, HDT Bio, Mestag Therapeutics, Medical Home Group; and equity in AbMeta Therapeutics  
902 and Adventris Pharmaceuticals. D.J.Z. reports grant/research support from Roche/Genentech.

903 **REFERENCES**

- 904 1. Garon EB, Hellmann MD, Rizvi NA, et al. Five-Year Overall Survival for Patients With Advanced Non-  
905 Small-Cell Lung Cancer Treated With Pembrolizumab: Results From the Phase I KEYNOTE-001 Study.  
906 *J Clin Oncol Off J Am Soc Clin Oncol*. 2019;37(28):2518-2527. doi:10.1200/JCO.19.00934
- 907 2. Larkin J, Chiarion-Sileni V, Gonzalez R, et al. Five-Year Survival with Combined Nivolumab and  
908 Ipilimumab in Advanced Melanoma. *N Engl J Med*. Published online September 27, 2019.  
909 doi:10.1056/NEJMoa1910836
- 910 3. Patel SP, Othus M, Chen Y, et al. Neoadjuvant–Adjuvant or Adjuvant-Only Pembrolizumab in  
911 Advanced Melanoma. *N Engl J Med*. 2023;388(9):813-823. doi:10.1056/NEJMoa2211437
- 912 4. Topalian SL, Forde PM, Emens LA, Yarchoan M, Smith KN, Pardoll DM. Neoadjuvant immune  
913 checkpoint blockade: A window of opportunity to advance cancer immunotherapy. *Cancer Cell*.  
914 Published online August 17, 2023. doi:10.1016/j.ccell.2023.07.011
- 915 5. Liu J, Blake SJ, Yong MCR, et al. Improved Efficacy of Neoadjuvant Compared to Adjuvant  
916 Immunotherapy to Eradicate Metastatic Disease. *Cancer Discov*. 2016;6(12):1382-1399.  
917 doi:10.1158/2159-8290.CD-16-0577
- 918 6. Liu J, O’Donnell JS, Yan J, et al. Timing of neoadjuvant immunotherapy in relation to surgery is  
919 crucial for outcome. *Oncoimmunology*. 2019;8(5):e1581530. doi:10.1080/2162402X.2019.1581530
- 920 7. Chalabi M, Fanchi LF, Dijkstra KK, et al. Neoadjuvant immunotherapy leads to pathological  
921 responses in MMR-proficient and MMR-deficient early-stage colon cancers. *Nat Med*.  
922 2020;26(4):566-576. doi:10.1038/s41591-020-0805-8
- 923 8. Ho WJ, Zhu Q, Durham J, et al. Neoadjuvant cabozantinib and nivolumab convert locally advanced  
924 hepatocellular carcinoma into resectable disease with enhanced antitumor immunity. *Nat Cancer*.  
925 Published online July 29, 2021:1-13. doi:10.1038/s43018-021-00234-4
- 926 9. Cabrita R, Lauss M, Sanna A, et al. Tertiary lymphoid structures improve immunotherapy and  
927 survival in melanoma. *Nature*. 2020;577(7791):561-565. doi:10.1038/s41586-019-1914-8
- 928 10. Petitprez F, de Reyniès A, Keung EZ, et al. B cells are associated with survival and immunotherapy  
929 response in sarcoma. *Nature*. 2020;577(7791):556-560. doi:10.1038/s41586-019-1906-8
- 930 11. Helmink BA, Reddy SM, Gao J, et al. B cells and tertiary lymphoid structures promote  
931 immunotherapy response. *Nature*. 2020;577(7791):549-555. doi:10.1038/s41586-019-1922-8
- 932 12. Vanhersecke L, Brunet M, Guégan JP, et al. Mature tertiary lymphoid structures predict immune  
933 checkpoint inhibitor efficacy in solid tumors independently of PD-L1 expression. *Nat Cancer*.  
934 2021;2(8):794-802. doi:10.1038/s43018-021-00232-6
- 935 13. Italiano A, Bessede A, Pulido M, et al. Pembrolizumab in soft-tissue sarcomas with tertiary lymphoid  
936 structures: a phase 2 PEMBROSARC trial cohort. *Nat Med*. Published online May 26, 2022.  
937 doi:10.1038/s41591-022-01821-3

- 938 14. Joshi NS, Akama-Garren EH, Lu Y, et al. Regulatory T Cells in Tumor-Associated Tertiary Lymphoid  
939 Structures Suppress Anti-tumor T Cell Responses. *Immunity*. 2015;43(3):579-590.  
940 doi:10.1016/j.immuni.2015.08.006
- 941 15. Rodriguez AB, Peske JD, Woods AN, et al. Immune mechanisms orchestrate tertiary lymphoid  
942 structures in tumors via cancer-associated fibroblasts. *Cell Rep*. 2021;36(3):109422.  
943 doi:10.1016/j.celrep.2021.109422
- 944 16. Calderaro J, Petitprez F, Becht E, et al. Intra-tumoral tertiary lymphoid structures are associated  
945 with a low risk of early recurrence of hepatocellular carcinoma. *J Hepatol*. 2019;70(1):58-65.  
946 doi:10.1016/j.jhep.2018.09.003
- 947 17. Cottrell TR, Thompson ED, Forde PM, et al. Pathologic features of response to neoadjuvant anti-PD-  
948 1 in resected non-small-cell lung carcinoma: a proposal for quantitative immune-related pathologic  
949 response criteria (irPRC). *Ann Oncol*. 2018;29(8):1853-1860. doi:10.1093/annonc/mdy218
- 950 18. Claeskens G, Hjort NL. *Model Selection and Model Averaging*. Cambridge University Press; 2008.  
951 doi:10.1017/CBO9780511790485
- 952 19. Santiago T, Kulemzin SV, Reshetnikova ES, et al. FCRLA is a resident endoplasmic reticulum protein  
953 that associates with intracellular Igs, IgM, IgG and IgA. *Int Immunol*. 2011;23(1):43-53.  
954 doi:10.1093/intimm/dxq456
- 955 20. Lainé A, Labiad O, Hernandez-Vargas H, et al. Regulatory T cells promote cancer immune-escape  
956 through integrin  $\alpha\beta 8$ -mediated TGF- $\beta$  activation. *Nat Commun*. 2021;12(1):6228.  
957 doi:10.1038/s41467-021-26352-2
- 958 21. Dodagatta-Marri E, Ma HY, Liang B, et al. Integrin  $\alpha\beta 8$  on T cells suppresses anti-tumor immunity in  
959 multiple models and is a promising target for tumor immunotherapy. *Cell Rep*. 2021;36(1):109309.  
960 doi:10.1016/j.celrep.2021.109309
- 961 22. García-Serna AM, Alcaraz-García MJ, Ruiz-Lafuente N, et al. Dock10 regulates CD23 expression and  
962 sustains B-cell lymphopoiesis in secondary lymphoid tissue. *Immunobiology*. 2016;221(12):1343-  
963 1350. doi:10.1016/j.imbio.2016.07.015
- 964 23. Theisen DJ, Davidson JT, Briseño CG, et al. WDFY4 is required for cross-presentation in response to  
965 viral and tumor antigens. *Science*. 2018;362(6415):694-699. doi:10.1126/science.aat5030
- 966 24. Coppola D, Nebozhyn M, Khalil F, et al. Unique Ectopic Lymph Node-Like Structures Present in  
967 Human Primary Colorectal Carcinoma Are Identified by Immune Gene Array Profiling. *Am J Pathol*.  
968 2011;179(1):37-45. doi:10.1016/j.ajpath.2011.03.007
- 969 25. Schumacher TN, Thommen DS. Tertiary lymphoid structures in cancer. *Science*. 375(6576):eabf9419.  
970 doi:10.1126/science.abf9419
- 971 26. Jacobsen JT, Hu W, R. Castro TB, et al. Expression of Foxp3 by T follicular helper cells in end-stage  
972 germinal centers. *Science*. 2021;373(6552):eabe5146. doi:10.1126/science.abe5146

- 973 27. Arulraj T, Binder SC, Meyer-Hermann M. Investigating the Mechanism of Germinal Center  
974 Shutdown. *Front Immunol*. 2022;13. Accessed March 4, 2023.  
975 <https://www.frontiersin.org/articles/10.3389/fimmu.2022.922318>
- 976 28. Milutinovic S, Abe J, Godkin A, Stein JV, Gallimore A. The Dual Role of High Endothelial Venules in  
977 Cancer Progression versus Immunity. *Trends Cancer*. 2021;7(3):214-225.  
978 doi:10.1016/j.trecan.2020.10.001
- 979 29. Asrir A, Tardiveau C, Coudert J, et al. Tumor-associated high endothelial venules mediate  
980 lymphocyte entry into tumors and predict response to PD-1 plus CTLA-4 combination  
981 immunotherapy. *Cancer Cell*. 2022;40(3):318-334.e9. doi:10.1016/j.ccell.2022.01.002
- 982 30. Astarita JL, Cremasco V, Fu J, et al. The CLEC-2–podoplanin axis controls fibroblastic reticular cell  
983 contractility and lymph node microarchitecture. *Nat Immunol*. 2015;16(1):75-84.  
984 doi:10.1038/ni.3035
- 985 31. Aoufouchi S, Faili A, Zober C, et al. Proteasomal degradation restricts the nuclear lifespan of AID. *J*  
986 *Exp Med*. 2008;205(6):1357-1368. doi:10.1084/jem.20070950
- 987 32. ZAN H, CASALI P. Regulation of Aicda expression and AID activity. *Autoimmunity*. 2013;46(2):83-101.  
988 doi:10.3109/08916934.2012.749244
- 989 33. Yoshitomi H, Ueno H. Shared and distinct roles of T peripheral helper and T follicular helper cells in  
990 human diseases. *Cell Mol Immunol*. 2021;18(3):523-527. doi:10.1038/s41423-020-00529-z
- 991 34. Rao DA, Gurish MF, Marshall JL, et al. Pathologically expanded peripheral T helper cell subset drives  
992 B cells in rheumatoid arthritis. *Nature*. 2017;542(7639):110-114. doi:10.1038/nature20810
- 993 35. Bocharnikov AV, Keegan J, Wacleche VS, et al. PD-1<sup>hi</sup>CXCR5<sup>+</sup> T peripheral helper cells promote B cell  
994 responses in lupus via MAF and IL-21. *JCI Insight*. 2019;4(20). doi:10.1172/jci.insight.130062
- 995 36. Kim JR, Lim HW, Kang SG, Hillsamer P, Kim CH. Human CD57+ germinal center-T cells are the major  
996 helpers for GC-B cells and induce class switch recombination. *BMC Immunol*. 2005;6:3.  
997 doi:10.1186/1471-2172-6-3
- 998 37. Marinova E, Han S, Zheng B. Germinal Center Helper T Cells Are Dual Functional Regulatory Cells  
999 with Suppressive Activity to Conventional CD4+ T Cells. *J Immunol*. 2007;178(8):5010-5017.  
1000 doi:10.4049/jimmunol.178.8.5010
- 1001 38. Palmer BE, Blyveis N, Fontenot AP, Wilson CC. Functional and Phenotypic Characterization of  
1002 CD57+CD4+ T Cells and Their Association with HIV-1-Induced T Cell Dysfunction1. *J Immunol*.  
1003 2005;175(12):8415-8423. doi:10.4049/jimmunol.175.12.8415
- 1004 39. Hong W, Yang B, He Q, Wang J, Weng Q. New Insights of CCR7 Signaling in Dendritic Cell Migration  
1005 and Inflammatory Diseases. *Front Pharmacol*. 2022;13. Accessed January 30, 2023.  
1006 <https://www.frontiersin.org/articles/10.3389/fphar.2022.841687>
- 1007 40. Horiuchi S, Wu H, Liu WC, et al. Tox2 is required for the maintenance of GC TFH cells and the  
1008 generation of memory TFH cells. *Sci Adv*. 2021;7(41):eabj1249. doi:10.1126/sciadv.abj1249

- 1009 41. van der Leun AM, Thommen DS, Schumacher TN. CD8+ T cell states in human cancer: insights from  
1010 single-cell analysis. *Nat Rev Cancer*. 2020;20(4):218-232. doi:10.1038/s41568-019-0235-4
- 1011 42. Caushi JX, Zhang J, Ji Z, et al. Transcriptional programs of neoantigen-specific TIL in anti-PD-1-  
1012 treated lung cancers. *Nature*. 2021;596(7870):126-132. doi:10.1038/s41586-021-03752-4
- 1013 43. Liu B, Zhang Y, Wang D, Hu X, Zhang Z. Single-cell meta-analyses reveal responses of tumor-reactive  
1014 CXCL13+ T cells to immune-checkpoint blockade. *Nat Cancer*. 2022;3(9):1123-1136.  
1015 doi:10.1038/s43018-022-00433-7
- 1016 44. Lucca LE, Axisa PP, Lu B, et al. Circulating clonally expanded T cells reflect functions of tumor-  
1017 infiltrating T cells. *J Exp Med*. 2021;218(4):e20200921. doi:10.1084/jem.20200921
- 1018 45. Posch F, Silina K, Leibl S, et al. Maturation of tertiary lymphoid structures and recurrence of stage II  
1019 and III colorectal cancer. *Oncoimmunology*. 2017;7(2):e1378844.  
1020 doi:10.1080/2162402X.2017.1378844
- 1021 46. Siliņa K, Soltermann A, Attar FM, et al. Germinal Centers Determine the Prognostic Relevance of  
1022 Tertiary Lymphoid Structures and Are Impaired by Corticosteroids in Lung Squamous Cell  
1023 Carcinoma. *Cancer Res*. 2018;78(5):1308-1320. doi:10.1158/0008-5472.CAN-17-1987
- 1024 47. Arulraj T, Binder SC, Robert PA, Meyer-Hermann M. Germinal Centre Shutdown. *Front Immunol*.  
1025 2021;12. Accessed March 4, 2023.  
1026 <https://www.frontiersin.org/articles/10.3389/fimmu.2021.705240>
- 1027 48. Gavil NV, Scott MC, Weyu E, et al. Chronic antigen in solid tumors drives a distinct program of T cell  
1028 residence. *Sci Immunol*. 2023;8(84):eadd5976. doi:10.1126/sciimmunol.add5976
- 1029 49. Garaud S, Dieu-Nosjean MC, Willard-Gallo K. T follicular helper and B cell crosstalk in tertiary  
1030 lymphoid structures and cancer immunotherapy. *Nat Commun*. 2022;13(1):2259.  
1031 doi:10.1038/s41467-022-29753-z
- 1032 50. Gutiérrez-Melo N, Baumjohann D. T follicular helper cells in cancer. *Trends Cancer*. 2023;9(4):309-  
1033 325. doi:10.1016/j.trecan.2022.12.007
- 1034 51. Gu-Trantien C, Loi S, Garaud S, et al. CD4<sup>+</sup> follicular helper T cell infiltration predicts breast cancer  
1035 survival. *J Clin Invest*. 2013;123(7):2873-2892. doi:10.1172/JCI67428
- 1036 52. Gu-Trantien C, Migliori E, Buisseret L, et al. CXCL13-producing TFH cells link immune suppression  
1037 and adaptive memory in human breast cancer. *JCI Insight*. 2017;2(11):e91487, 91487.  
1038 doi:10.1172/jci.insight.91487
- 1039 53. Argyriou A, Wadsworth MH, Lendvai A, et al. Single cell sequencing identifies clonally expanded  
1040 synovial CD4<sup>+</sup> T<sub>H</sub>17 cells expressing GPR56 in rheumatoid arthritis. *Nat Commun*. 2022;13(1):4046.  
1041 doi:10.1038/s41467-022-31519-6
- 1042 54. Chung Y, Tanaka S, Chu F, et al. Follicular regulatory T cells expressing Foxp3 and Bcl-6 suppress  
1043 germinal center reactions. *Nat Med*. 2011;17(8):983-988. doi:10.1038/nm.2426

- 1044 55. Linterman MA, Pierson W, Lee SK, et al. Foxp3+ follicular regulatory T cells control the germinal  
1045 center response. *Nat Med*. 2011;17(8):975-982. doi:10.1038/nm.2425
- 1046 56. Sage PT, Francisco LM, Carman CV, Sharpe AH. The receptor PD-1 controls follicular regulatory T  
1047 cells in the lymph nodes and blood. *Nat Immunol*. 2013;14(2):152-161. doi:10.1038/ni.2496
- 1048 57. Sage PT, Paterson AM, Lovitch SB, Sharpe AH. The coinhibitory receptor CTLA-4 controls B cell  
1049 responses by modulating T follicular helper, T follicular regulatory, and T regulatory cells. *Immunity*.  
1050 2014;41(6):1026-1039. doi:10.1016/j.immuni.2014.12.005
- 1051 58. Wing JB, Ise W, Kurosaki T, Sakaguchi S. Regulatory T cells control antigen-specific expansion of Tfh  
1052 cell number and humoral immune responses via the coreceptor CTLA-4. *Immunity*. 2014;41(6):1013-  
1053 1025. doi:10.1016/j.immuni.2014.12.006
- 1054 59. Raftery AE. Bayesian Model Selection in Social Research. *Sociol Methodol*. 1995;25:111-163.  
1055 doi:10.2307/271063
- 1056 60. Abbott CW, Boyle SM, Pyke RM, et al. Prediction of Immunotherapy Response in Melanoma through  
1057 Combined Modeling of Neoantigen Burden and Immune-Related Resistance Mechanisms. *Clin*  
1058 *Cancer Res Off J Am Assoc Cancer Res*. 2021;27(15):4265-4276. doi:10.1158/1078-0432.CCR-20-  
1059 4314
- 1060 61. Love MI, Huber W, Anders S. Moderated estimation of fold change and dispersion for RNA-seq data  
1061 with DESeq2. *Genome Biol*. 2014;15(12):550. doi:10.1186/s13059-014-0550-8
- 1062 62. Gene set enrichment analysis: A knowledge-based approach for interpreting genome-wide  
1063 expression profiles | PNAS. Accessed June 12, 2023.  
1064 <https://www.pnas.org/doi/10.1073/pnas.0506580102>
- 1065 63. Korotkevich G, Sukhov V, Budin N, Shpak B, Artyomov MN, Sergushichev A. Fast gene set  
1066 enrichment analysis. Published online February 1, 2021:060012. doi:10.1101/060012
- 1067 64. Levy E, Milani P, Bartha G, et al. 67 B-cell receptor heavy chain repertoire profiling using an  
1068 augmented transcriptome. *J Immunother Cancer*. 2020;8(Suppl 3). doi:10.1136/jitc-2020-  
1069 SITC2020.0067
- 1070 65. Bolotin DA, Poslavsky S, Mitrophanov I, et al. MiXCR: software for comprehensive adaptive  
1071 immunity profiling. *Nat Methods*. 2015;12(5):380-381. doi:10.1038/nmeth.3364
- 1072 66. ImmunoMind Team. immunarch: an R package for painless bioinformatics analysis of T-cell and B-  
1073 cell immune repertoires. Zenodo <https://doi.org/10.5281/zenodo.3367200> (2019).
- 1074 67. Montagne JM, Zheng XA, Pinal-Fernandez I, et al. Ultra-efficient sequencing of T Cell receptor  
1075 repertoires reveals shared responses in muscle from patients with Myositis. *EBioMedicine*.  
1076 2020;59:102972. doi:10.1016/j.ebiom.2020.102972
- 1077 68. Zabransky DJ, Danilova L, Leatherman JM, et al. Profiling of syngeneic mouse HCC tumor models as a  
1078 framework to understand anti-PD-1 sensitive tumor microenvironments. *Hepatology*.  
1079 2023;77(5):1566. doi:10.1002/hep.32707



- 1080 69. Zanotelli VRT, Bodenmiller B. ImcSegmentationPipeline: A pixelclassification based multiplexed  
1081 image segmentation pipeline. Published online September 14, 2017. doi:10.5281/zenodo.3841961
- 1082 70. Carpenter AE, Jones TR, Lamprecht MR, et al. CellProfiler: image analysis software for identifying  
1083 and quantifying cell phenotypes. *Genome Biol.* 2006;7(10):R100. doi:10.1186/gb-2006-7-10-r100
- 1084 71. Berg S, Kutra D, Kroeger T, et al. ilastik: interactive machine learning for (bio)image analysis. *Nat*  
1085 *Methods.* 2019;16(12):1226-1232. doi:10.1038/s41592-019-0582-9
- 1086 72. Schapiro D, Jackson HW, Raghuraman S, et al. histoCAT: analysis of cell phenotypes and interactions  
1087 in multiplex image cytometry data. *Nat Methods.* 2017;14(9):873-876. doi:10.1038/nmeth.4391
- 1088 73. FlowSOM: Using self-organizing maps for visualization and interpretation of cytometry data - Van  
1089 Gassen - 2015 - Cytometry Part A - Wiley Online Library. Accessed June 14, 2023.  
1090 <https://onlinelibrary.wiley.com/doi/full/10.1002/cyto.a.22625>
- 1091 74. Schneider CA, Rasband WS, Eliceiri KW. NIH Image to ImageJ: 25 years of image analysis. *Nat*  
1092 *Methods.* 2012;9(7):671-675. doi:10.1038/nmeth.2089
- 1093 75. Epskamp S, Cramer AOJ, Waldorp LJ, Schmittmann VD, Borsboom D. qgraph: Network Visualizations  
1094 of Relationships in Psychometric Data. *J Stat Softw.* 2012;48:1-18. doi:10.18637/jss.v048.i04
- 1095 76. Robins HS, Campregher PV, Srivastava SK, et al. Comprehensive assessment of T-cell receptor beta-  
1096 chain diversity in alphabeta T cells. *Blood.* 2009;114(19):4099-4107. doi:10.1182/blood-2009-04-  
1097 217604
- 1098 77. Carlson CS, Emerson RO, Sherwood AM, et al. Using synthetic templates to design an unbiased  
1099 multiplex PCR assay. *Nat Commun.* 2013;4:2680. doi:10.1038/ncomms3680
- 1100 78. Gupta NT, Vander Heiden JA, Uduman M, Gadala-Maria D, Yaari G, Kleinstein SH. Change-O: a  
1101 toolkit for analyzing large-scale B cell immunoglobulin repertoire sequencing data. *Bioinformatics.*  
1102 2015;31(20):3356-3358. doi:10.1093/bioinformatics/btv359
- 1103 79. Venturi V, Kedzierska K, Tanaka MM, Turner SJ, Doherty PC, Davenport MP. Method for assessing  
1104 the similarity between subsets of the T cell receptor repertoire. *J Immunol Methods.*  
1105 2008;329(1):67-80. doi:10.1016/j.jim.2007.09.016
- 1106 80. Hafemeister C, Satija R. Normalization and variance stabilization of single-cell RNA-seq data using  
1107 regularized negative binomial regression. *Genome Biol.* 2019;20(1):296. doi:10.1186/s13059-019-  
1108 1874-1
- 1109 81. Ahlmann-Eltze C, Huber W. glmGamPoi: fitting Gamma-Poisson generalized linear models on single  
1110 cell count data. *Bioinformatics.* 2020;36(24):5701-5702. doi:10.1093/bioinformatics/btaa1009
- 1111 82. Hao Y, Hao S, Andersen-Nissen E, et al. Integrated analysis of multimodal single-cell data. *Cell.*  
1112 2021;184(13):3573-3587.e29. doi:10.1016/j.cell.2021.04.048

- 1113 83. Finak G, McDavid A, Yajima M, et al. MAST: a flexible statistical framework for assessing  
1114 transcriptional changes and characterizing heterogeneity in single-cell RNA sequencing data.  
1115 *Genome Biol.* 2015;16:278. doi:10.1186/s13059-015-0844-5
- 1116 84. Borcharding N, Bormann NL, Kraus G. scRepertoire: An R-based toolkit for single-cell immune  
1117 receptor analysis. *F1000Research.* 2020;9:47. doi:10.12688/f1000research.22139.2
- 1118

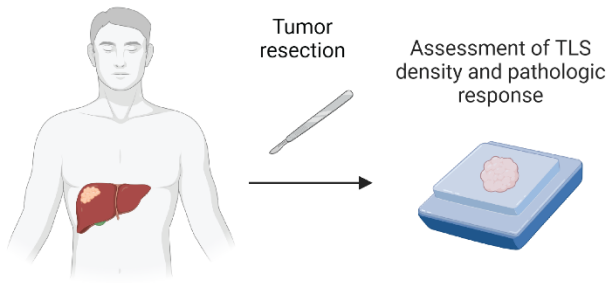
1119 **Table 1 | Characteristics of the Patients, According to Treatment Status**

	<b>Neoadjuvant (N=19)</b>	<b>Untreated (N=14)</b>	<b>Total (N=33)</b>
<b>Age at surgery — yr</b>			
Mean (SD)	64±10	66±9.0	65±9.6
Median (range)	65 (41-79)	66 (49-84)	65 (41-84)
<b>Sex — no. (%)</b>			
Male	11 (58)	11 (79)	22 (67)
Female	8 (42)	3 (21)	11 (33)
<b>Histologic grade — no. (%)</b>			
Poorly differentiated	3 (16)	1 (7)	4 (12)
Moderately differentiated	13 (68)	8 (57)	21 (64)
Well differentiated	3 (16)	5 (36)	8 (24)
<b>Etiology — no. (%)</b>			
HBV	3 (16)	1 (7)	4 (12)
HCV	7 (37)	6 (43)	13 (39)
HBV/HCV	1 (5)	1 (7)	2 (6)
NASH	2 (11)	3 (21)	5 (15)
ETOH	1 (5)	1 (7)	2 (6)
Unknown	5 (26)	2 (14)	7 (21)
<b>Neoadjuvant Treatment — no. (%)</b>			
anti-PD1 + TKI	14 (74)	0 (0)	14 (42)
anti-PD1	3 (16)	0 (0)	3 (9)
anti-PD1 + anti-CTLA4	1 (5)	0 (0)	1 (3)
anti-PD1 + anti-CTLA4 + TKI	1 (5)	0 (0)	1 (3)
None	0 (0)	14 (100)	14 (42)

1120  
1121  
1122

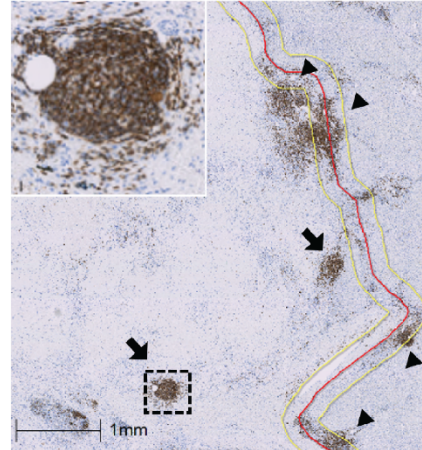
1123  
1124

**a**

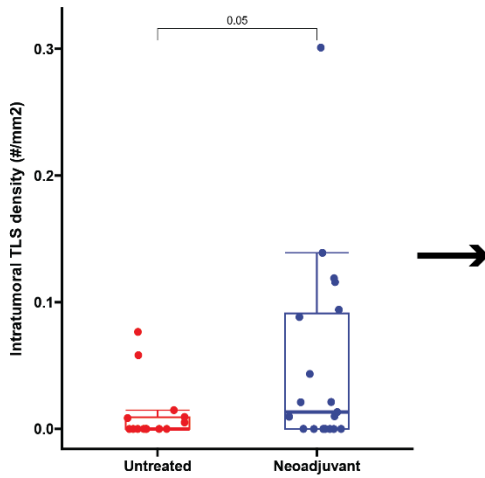


Neoadjuvant ICB ( $n = 19$ ) vs untreated ( $n = 14$ )

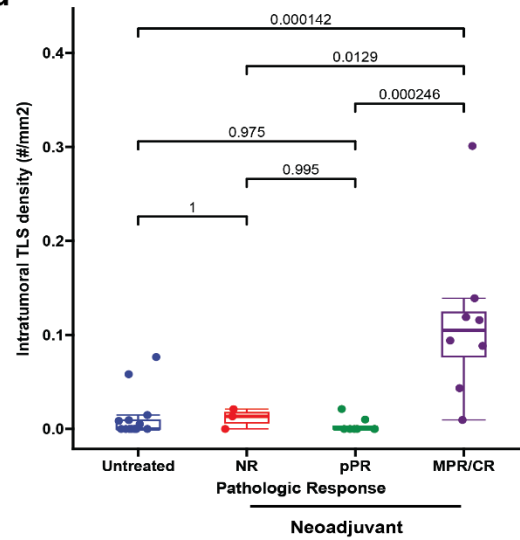
**b**



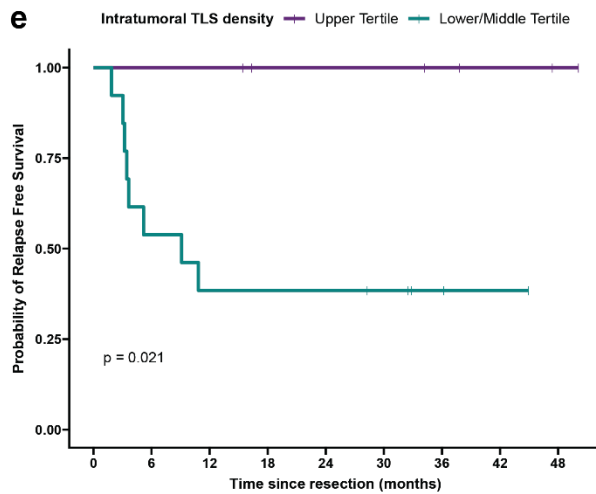
**c**



**d**



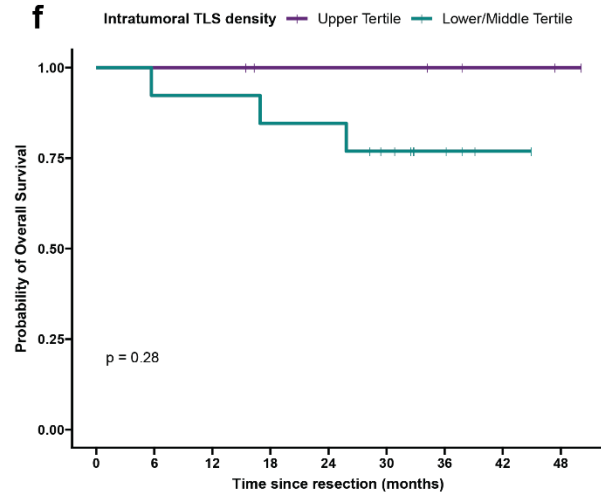
**e**



Number at risk

6	6	6	4	4	4	3	2	1
13	7	5	5	5	4	2	1	0

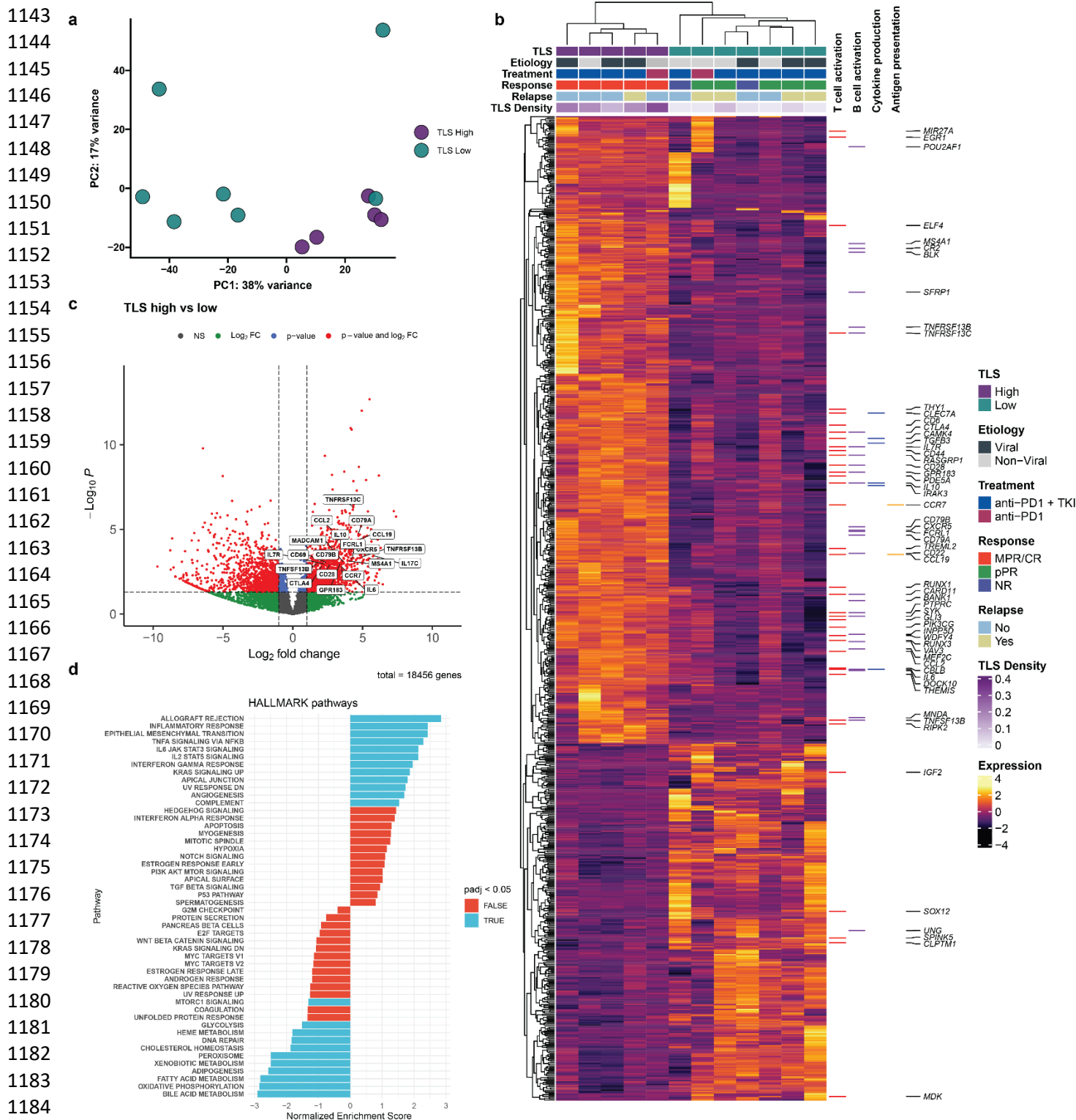
**f**



Number at risk

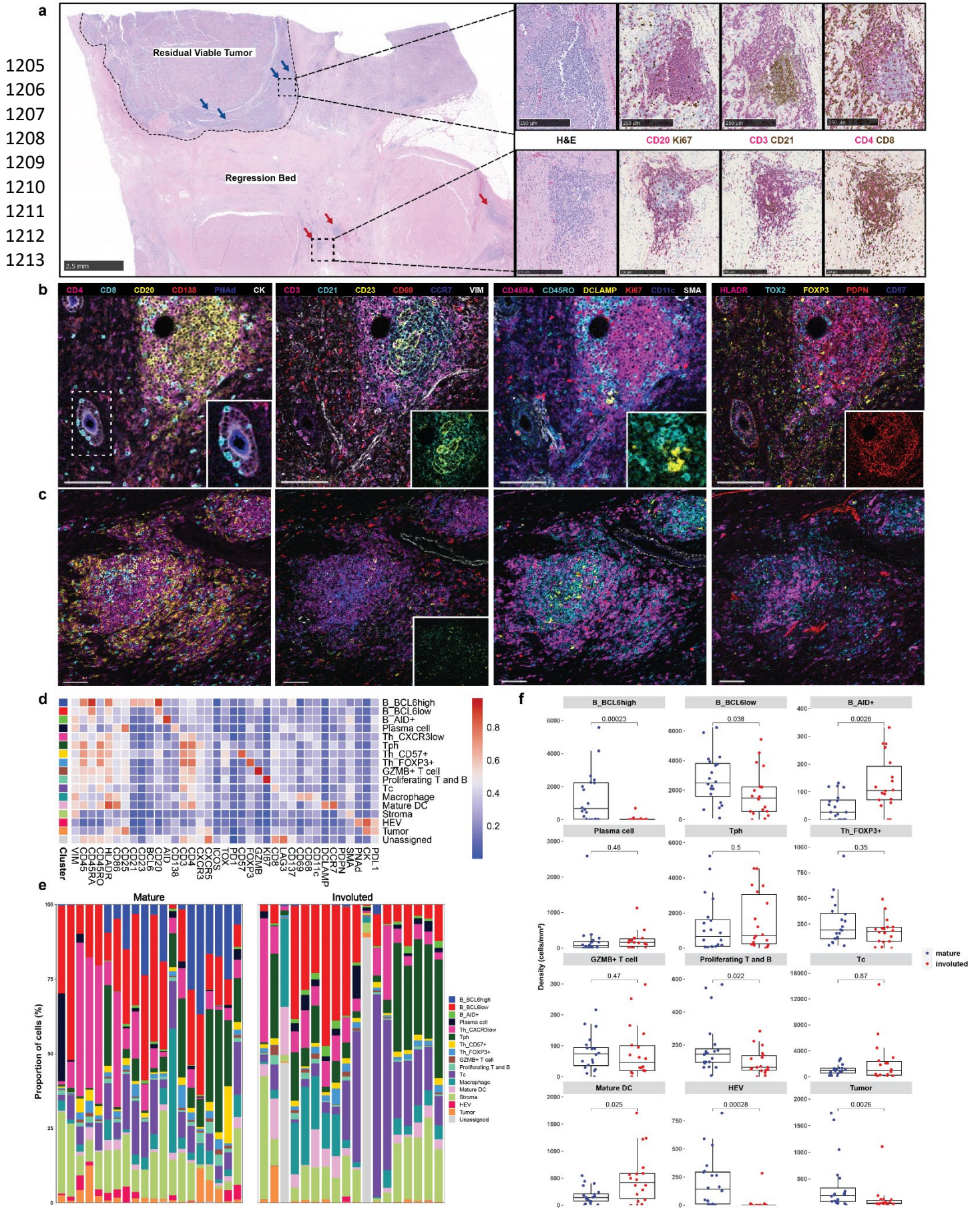
6	6	6	4	4	4	3	2	1
13	12	12	11	11	8	4	1	0

1126 **Fig. 1 | Neoadjuvant ICB induces intratumoral TLS, which are associated with superior**  
1127 **pathologic response and relapse free survival. a,** Workflow for TLS density analysis. **b,**  
1128 Representative images of formalin fixed paraffin embedded (FFPE) HCC tumors stained with anti-  
1129 CD20 antibody. Annotations indicate boundary between tumor/tumor regression bed and  
1130 adjacent normal parenchyma (red), extension of boundary by 200  $\mu\text{m}$  (yellow), intratumoral TLS  
1131 (arrow), and peritumoral TLS (arrow head). Inset shows representative TLS at high magnification.  
1132 Scale bar, 1mm. **c,** Box-and-whisker plots showing intratumoral TLS density in patients with  
1133 locally advanced HCC treated with neoadjuvant ICB ( $n = 19$ ) and untreated controls ( $n = 14$ ). **d,**  
1134 Boxplot-and-whisker plots showing intratumoral TLS density in untreated ( $n = 14$ ) and  
1135 neoadjuvant treated tumors, divided according to pathologic response ( $n = 19$ ). For each box-  
1136 and-whisker plot, the horizontal bar indicates the median, the upper and lower limits of the boxes  
1137 the interquartile range, and the ends of the whiskers 1.5 times the interquartile range. **e-f,** Kaplan-  
1138 Meier curves showing relapse free survival (**e**) and overall survival (**f**) for patients with HCC in the  
1139 highest tertile (purple) compared to the middle and lowest tertiles (green) of intratumoral TLS  
1140 density after neoadjuvant ICB. Statistical significance was determined by two-tailed t-test (**c**), one-  
1141 way ANOVA followed by Tukey's honest significant difference (HSD) test (**d**), and log-rank test (**e**  
1142 and **f**).



1185  
1186  
1187  
1188

1189 **Fig. 2 | High TLS density is associated with increased T and B cell activation in HCC treated**  
1190 **with neoadjuvant ICB. a**, Principle component analysis of bulk RNA-sequencing of resected  
1191 HCC tumors treated with neoadjuvant ICB ( $n = 12$ ), divided according to TLS density relative to  
1192 mean density of the neoadjuvant treatment group. **b**, Heatmap showing differentially expressed  
1193 genes (DEG) with a  $\log_2$  fold change  $> 1$  and  $P < 0.05$  between tumors with high ( $n = 5$ ) and low  
1194 ( $n = 7$ ) TLS density. Annotation rows indicate TLS group, HCC etiology, treatment, response,  
1195 relapse, and TLS density. Annotation columns at right identify DEG belonging to Gene Oncology  
1196 Biological Pathways gene sets for T cell activation, B cell activation, Cytokine production, and  
1197 Dendritic Cell Antigen Processing and Presentation. **c**, Volcano plot showing differentially  
1198 expressed genes between tumors with high and low TLS density. Vertical dotted lines represents  
1199  $\log_2$  fold change greater than or less than 1. Horizontal dotted line indicates adjusted P value of  
1200 0.05. 4 outlier genes are excluded from the plot for the purposes of visualization. **d**, Gene set  
1201 enrichment analysis showing differentially enriched gene sets from the HALLMARK database  
1202 between tumors with high and low TLS density. **e**, Barcode plots showing enrichment scores for  
1203 the Gene Ontology Biological Pathways gene sets for T cell activation, B cell activation, and  
1204 Dendritic Cell Antigen Processing and Presentation.





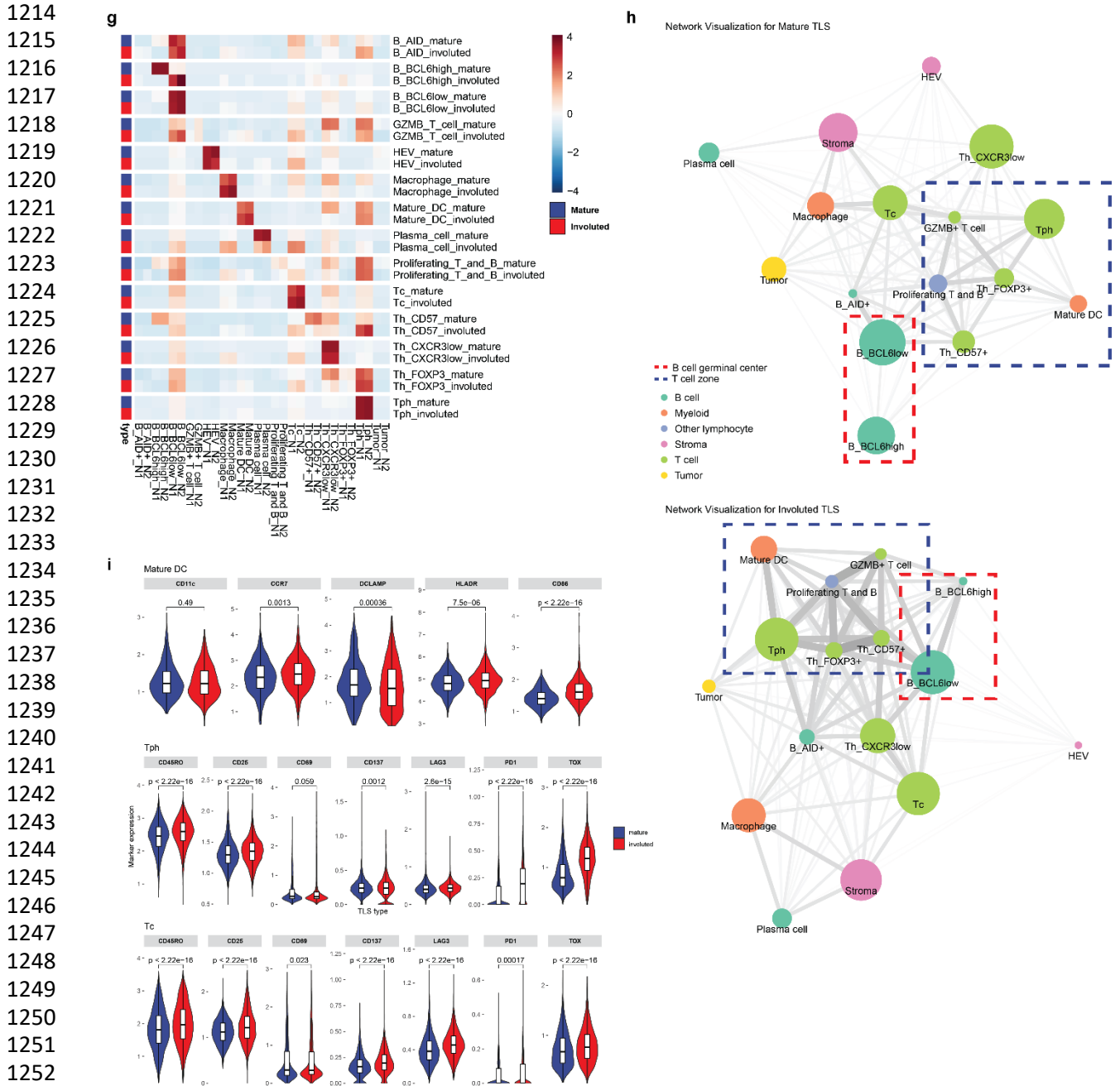
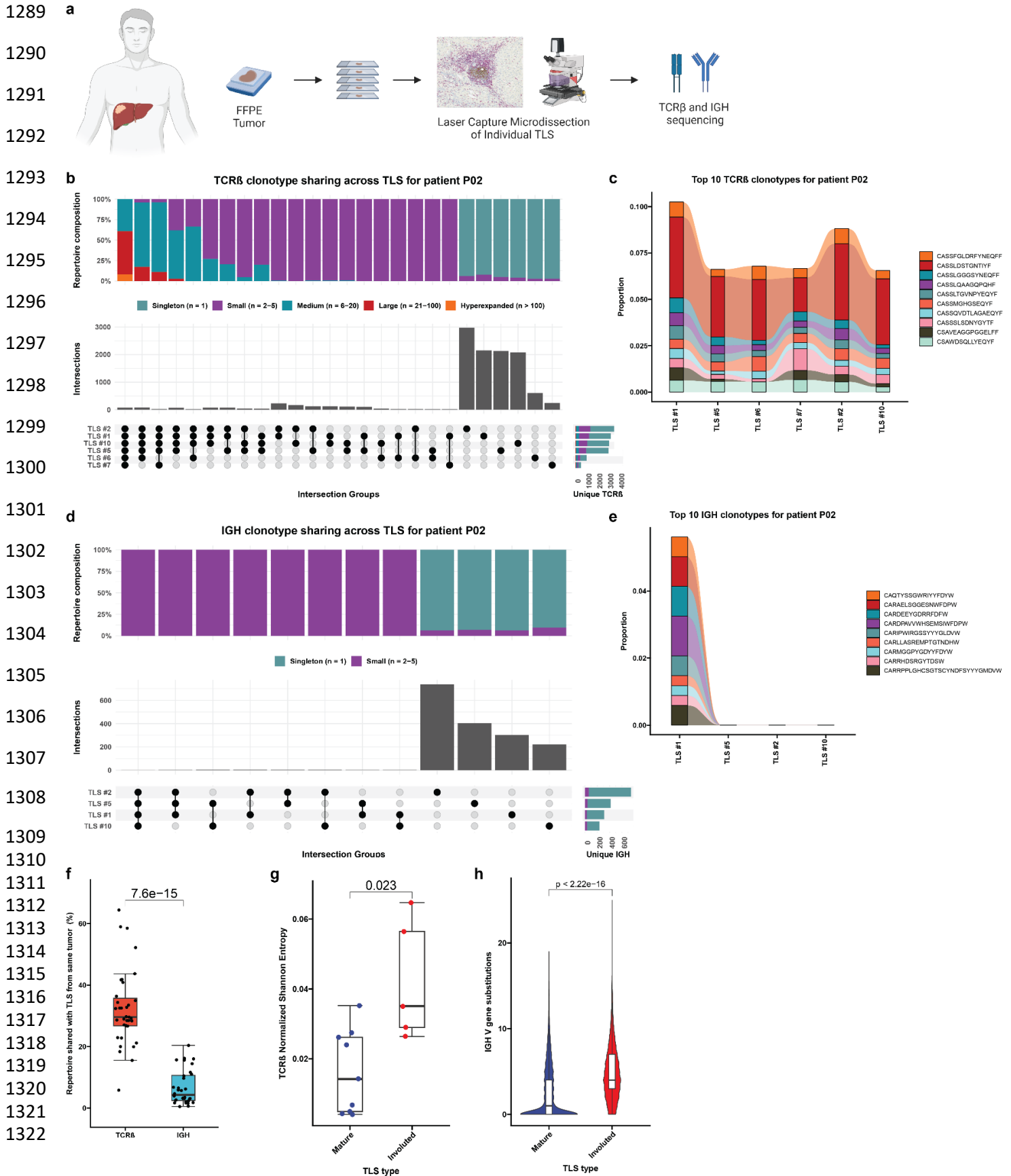
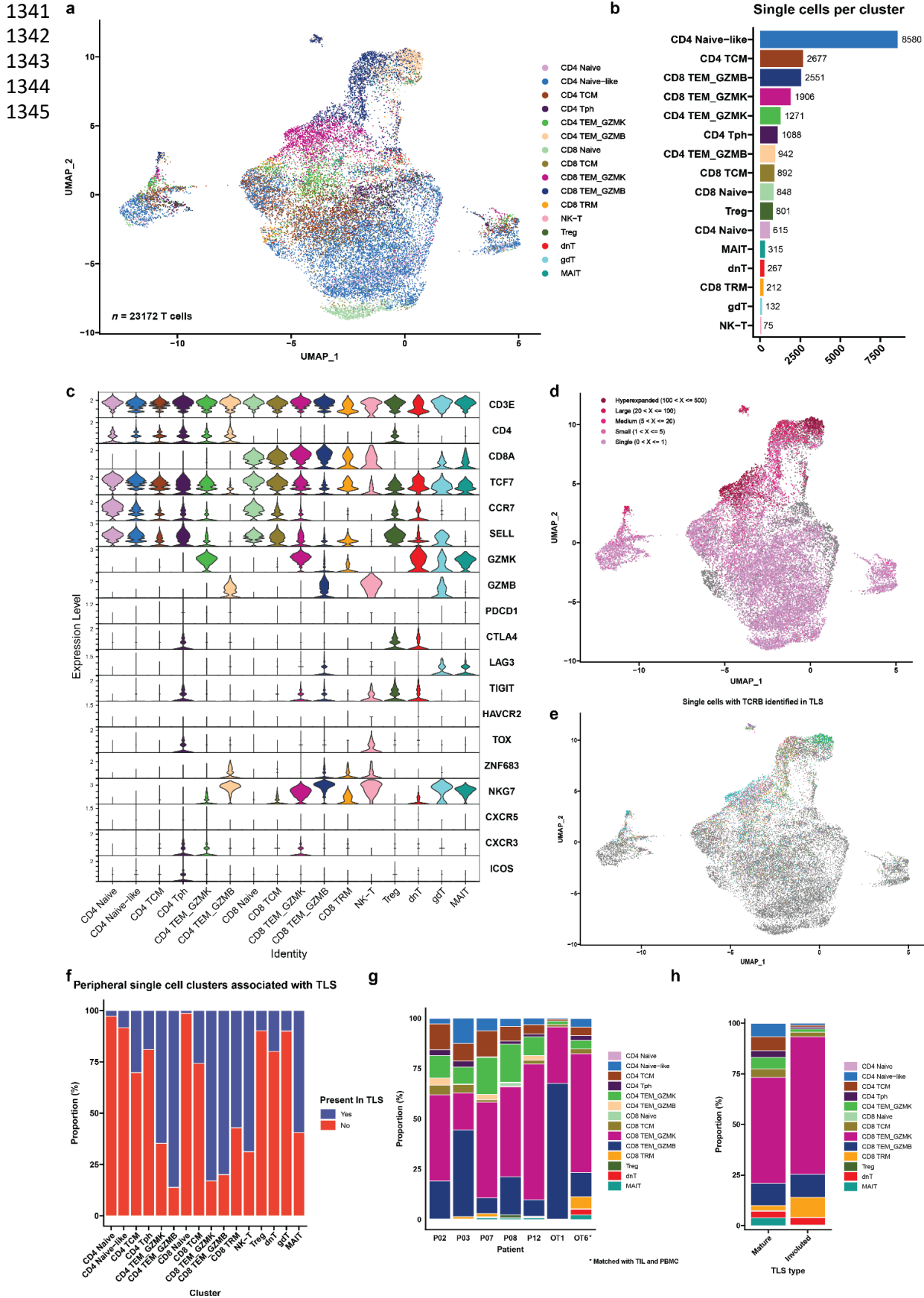


**Fig. 3 | Identification of divergent TLS morphologies and cellular spatial relationships in viable tumor and tumor regression bed.** **a**, Representative formalin-fixed, paraffin embedded (FFPE) neoadjuvant ICB-treated tumor stained with hematoxylin and eosin (H&E) showing divergent TLS morphologies (“mature” and “involved”) in viable residual viable tumor and regression bed. Dotted line shows boundary between residual viable tumor and regression bed. Blue arrows indicate mature TLS and red arrows indicate involuted TLS. Scale bar, 2.5mm. Higher magnification images of representative mature and involuted TLS are shown on right with serial sections stained with dual immunohistochemistry staining for CD20 (magenta) and Ki67 (brown), CD3 (magenta) and CD21 (brown), and CD4 (magenta) and CD8 (brown). Scale bars, 250  $\mu$ m. **b-c**, Representative images of mature (**b**) and involuted (**c**) TLS obtained by imaging mass

1265 cytometry. Insets show higher magnification images of CD8<sup>+</sup> T cells trafficking through high  
1266 endothelial venules (**b, far left**), an extensive CD21<sup>+</sup>CD23<sup>+</sup> follicular dendritic cell network in the  
1267 mature morphology (**b, middle left**) compared to scant CD21<sup>+</sup> and CD23<sup>+</sup> in the involuted  
1268 morphology (**c, middle left**), close interactions between T cells and DCLAMP<sup>+</sup> mature dendritic  
1269 cells in the T cell zone adjacent to the germinal center (**b, middle right**), and high podoplanin  
1270 expression in the germinal center of the mature TLS (**b, far right**). Scale bars, 100  $\mu$ m. **d**,  
1271 Heatmap showing average IMC marker expression in annotated cell clusters identified from  
1272 90,344 single cells from 38 TLS ( $n = 20$  mature,  $n = 18$  involuted). **e**, Composition of mature and  
1273 involuted TLS regions by cell type as a percentage of total cells per TLS. **f**, Box-and-whisker plots  
1274 showing cell cluster density in mature versus involuted TLS. For each box-and-whisker plot, the  
1275 horizontal bar indicates the median, the upper and lower limits of the boxes the interquartile range,  
1276 and the ends of the whiskers 1.5 times the interquartile range. **g**, Nearest neighbor analysis with  
1277 rows indicating individual clusters in mature and involuted TLS and columns corresponding to first  
1278 and second most common neighbors. **h**, Network analysis for cell clusters in mature and involuted  
1279 TLS. Node size corresponds to the proportion of total cells for each TLS type occupied by each  
1280 cluster. Edge length represents the shortest distance between cell clusters and thickness  
1281 corresponds to the number of measurements for each TLS type. **i**, Box and violin plots showing  
1282 expression of mature dendritic cell markers (CD11c, CCR7, DCLAMP, HLADR, and CD86) in the  
1283 mature DC cluster and markers of T cell activation and exhaustion (CD45RO, CD25, CD69,  
1284 CD137, LAG3, PD1, and TOX) in the T peripheral helper (Tph) and cytotoxic T cell (Tc) clusters,  
1285 by TLS morphology. Statistical significance was determined by pairwise two sample Wilcoxon test  
1286 (**f** and **g**).  
1287  
1288

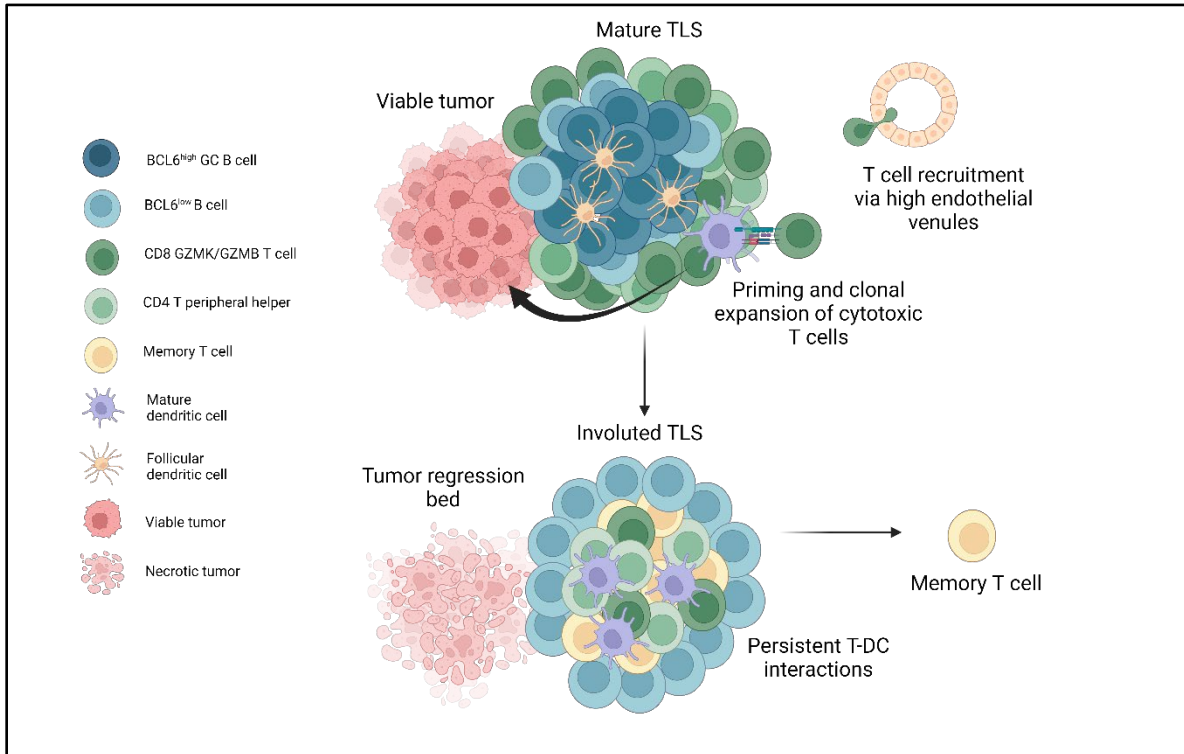


1323 **Fig. 4 | Expanded T cell clonotypes are shared across TLS within a tumor, while B cell**  
1324 **repertoires of individual TLS are highly distinct. a**, Workflow for T and B cell repertoire profiling  
1325 of microdissected TLS ( $n = 30$  mature and 5 involuted) from 7 patients. **b** and **d**, Upset plots  
1326 showing overlap in unique TCR $\beta$  (**b**) and IGH (**d**) clonotypes across microdissected TLS from the  
1327 same patient (P02). Barplots in gray and annotation row indicate distinct groups of clonotypes  
1328 shared between different TLS. Top stacked barplots indicate composition of groups according to  
1329 clonal expansion. Bottom right stacked barplots indicate total number of unique TCR $\beta$  or IGH  
1330 clonotypes identified at each TLS according to degree of clonal expansion. **c** and **e**, Alluvial plots  
1331 tracking the top 10 TCR $\beta$  (**c**) or IGH (**e**) clonotypes from TLS # 1 of patient P02 across all TLS  
1332 microdissected from the patient's tumor. **f**, Box-and-whisker plot comparing the percentage of the  
1333 TCR $\beta$  or IGH repertoire of each TLS that is shared with other TLS from the same tumor. **g**, Box-  
1334 and-whisker plots comparing TCR $\beta$  clonality (as determined by Normalized Shannon Entropy) in  
1335 mature and involuted TLS microdissected from patients P12, OT1, and OT6. Each point  
1336 represents the TCR $\beta$  of an individual TLS. **h**, Violin plots comparing number of somatic  
1337 hypermutations in IGH of mature and involuted TLS microdissected from patients P12, OT1, and  
1338 OT6. Individual data points (not shown) represent individual IGH sequences. Statistical  
1339 significance was determined by two-tailed t test (**f-h**).  
1340



1346 **Fig. 5 | Cytotoxic granzyme K and granzyme B-expressing CD8 T cells are highly**  
1347 **represented in TLS. a**, Uniform Manifold Approximation and Projection (UMAP) of 23,172 T cells  
1348 identified by single cell RNA/TCR/BCR sequencing of CD3<sup>+</sup>CD19<sup>+</sup> FACS-sorted peripheral blood  
1349 from HCC patients treated with neoadjuvant ICB ( $n = 7$ ). **b**, Barplot showing number of single cells  
1350 per cluster. **c**, Violin plots showing expression of subset specific marker genes across clusters.  
1351 **d-e**, UMAPs showing clonality of single cells with an associated T cell receptor sequence (**d**) and  
1352 single cells with a TCR $\beta$  identified in microdissected TLS (**e**). **f**, Stacked barplot showing  
1353 proportion of each single cell cluster identified in TLS. **g**, Inferred transcriptional phenotype of  
1354 TCR $\beta$  clonotypes in microdissected TLS with a matching TCR $\beta$  in single cell sequencing of post-  
1355 treatment peripheral blood ( $n = 7$ ) or tumor infiltrating lymphocytes ( $n = 1$ ). **h**, Inferred  
1356 transcriptional phenotype of TCR $\beta$  clonotypes in mature and resolving TLS of patient OT6.

1357  
1358  
1359  
1360  
1361  
1362  
1363  
1364  
1365  
1366  
1367  
1368  
1369  
1370



1371 **Fig. 6 | TLS structure and function in viable tumor and tumor regression bed in tumors**  
1372 **treated with neoadjuvant checkpoint blockade.** Mature TLS in viable tumor display a highly  
1373 organized germinal center with close interactions between germinal center B cells and CD21<sup>+</sup>  
1374 follicular dendritic cells, a T cell zone characterized by CD4<sup>+</sup> T peripheral helper cells in close  
1375 proximity to mature dendritic cells, and cytotoxic CD8<sup>+</sup> T cells trafficking to the tumor via high  
1376 endothelial venules. In areas of tumor regression, an involuted TLS morphology is found which  
1377 displays dissolution of the B cell germinal center and persistence of Tph-DC interactions in the T  
1378 cell zone, increased T cell memory marker expression, and clonal expansion of cytotoxic and  
1379 tissue resident memory CD8<sup>+</sup> T cells.

1380

1381 **Extended Data Table 1 | Clinical Characteristics of HCC cohort treated with neoadjuvant**  
 1382 **ICB.** Characteristics of treated patients. Each row represents a single patient and columns  
 1383 indicate age at surgery, sex, HCC etiology, histologic grade, treatment regimen, pathologic  
 1384 response, and whether the patient suffered relapsed or death.  
 1385

Patient	Age at surgery	Sex	Etiology	Histologic grade	Treatment	Response	Relapse	Death
P01	66	M	HCV	Moderately differentiated	α-PD1 + TKI	NR	No	No
P02	72	M	HCV	Moderately differentiated	α-PD1 + TKI	MPR	No	No
P03	76	F	Unknown	Moderately differentiated	α-PD1 + TKI	MPR	No	No
P07	64	F	HBV/HCV	Moderately differentiated	α-PD1 + TKI	pPR	Yes	Yes
P08	65	M	HCV	Moderately differentiated	α-PD1 + TKI	MPR	Yes	No
P09	47	M	HBV	Moderately differentiated	α-PD1 + TKI	CR	No	No
P10	41	F	HBV	Moderately differentiated	α-PD1 + TKI	pPR	Yes	Yes
P11	56	F	Unknown	Well differentiated	α-PD1 + TKI	pPR	No	No
P12	69	M	HCV	Moderately differentiated	α-PD1 + TKI	MPR	No	No
P13	74	F	Unknown	Poorly differentiated	α-PD1 + TKI	NR	No	No
P14	79	M	Unknown	Moderately differentiated	α-PD1 + TKI	pPR	Yes	No
P15	49	M	NASH	Moderately differentiated	α-PD1 + TKI	NR	Yes	Yes
OT1	68	M	ETOH	Poorly differentiated	α-PD1	MPR	No	No
OT2	71	F	Unknown	Well differentiated	α-PD1	pPR	No	No
OT3	63	M	HCV	Moderately differentiated	α-PD1 + TKI	pPR	Yes	No
OT4	69	F	HCV	Well differentiated	α-PD1 + TKI	pPR	Yes	No
OT5	62	M	NASH	Moderately differentiated	α-PD1	pPR	Yes	No
OT6	61	M	HCV	Moderately differentiated	α-PD1 + α-CTLA4 + TKI	MPR	No	No
OT7	56	F	HBV	Poorly differentiated	α-PD1 + α-CTLA4	CR	No	No

1386  
 1387



1388 **Extended Data Table 2 | Clinical characteristics of untreated HCC cohort.** Characteristics of  
1389 untreated patients. Each row represents a single patient and columns indicate age at surgery,  
1390 sex, HCC etiology, histologic grade, and treatment.  
1391

Patient	Age at surgery	Sex	Etiology	Histologic grade	Treatment
C2	61	M	HCV	Moderately differentiated	none
C3	60	M	HBV/HCV	Well differentiated	none
C5	75	M	HCV/NASH	Well differentiated	none
C6	63	F	HCV	Moderately differentiated	none
C7	61	M	HCV/ETOH	Well differentiated	none
C8	57	M	NASH	Well differentiated	none
C9	65	M	HBV/ETOH	Moderately differentiated	none
C10	66	M	HCV	Well differentiated	none
C11	69	F	HCV	Moderately differentiated	none
C12	71	M	NASH	Moderately differentiated	none
C13	78	M	Unknown	Moderately differentiated	none
C14	66	M	Unknown	Moderately differentiated	none
C15	84	F	NASH	Poorly differentiated	none
C16	49	M	ETOH	Moderately differentiated	none

1392

1393

1394 **Extended Data Table 3 | Immune Related Pathologic Response Criteria Scoring for HCC**  
 1395 **tumors treated with neoadjuvant anti-PD-1.**

<b>Feature, <i>n</i> (%)</b>	<b>MPR/CR (<i>n</i> = 8)</b>	<b>pPR/NR (<i>n</i> = 11)</b>	<b>P value†</b>
<b>Tumor</b>			
Fibrosis			
Immature fibrosis	8 (100%)	7 (63.6%)	0.103
Mature fibrosis	8 (100%)	7 (63.6%)	0.103
Neovascularization	1 (12.5%)	0 (0%)	0.421
Cholesterol clefts	4 (50.0%)	2 (18.2%)	0.319
Granulomas	3 (37.5%)	2 (18.2%)	0.603
Foamy histiocytes	5 (62.5%)	4 (36.4%)	0.37
Giant cells	1 (12.5%)	2 (18.2%)	1
Hemosiderin macrophages	7 (87.5%)	5 (45.5%)	0.147
Calcification	1 (12.5%)	1 (9.1%)	1
Lymphoid aggregates	8 (100%)	8 (72.7%)	0.228
Tertiary lymphoid structures	6 (75.0%)	2 (18.2%)	0.0237
Dense plasma cells	2 (25.0%)	1 (9.1%)	0.546
<b>Peritumor</b>			
Lymphoid aggregates	7 (87.5%)	8 (72.7%)	0.603
Tertiary lymphoid structures	4 (50.0%)	3 (27.3%)	0.377
Dense plasma cells	1 (12.5%)	0 (0%)	0.421

1396 † Fisher's Exact test

1397

1398 **Extended Data Table 4 | Bayesian Information Criteria results for predicting relapse and**  
1399 **death following surgical resection in HCC treated with neoadjuvant ICB.** Rows represent  
1400 different BIC calculations and columns indicate outcomes and variables evaluated and calculated  
1401 BIC.  
1402

<b>Outcome</b>	<b>Variable</b>	<b>BIC</b>
Relapse	Total TLS density	43.04
Relapse	Peritumoral TLS density	45.4
Relapse	Intratumoral TLS	37.61
Relapse	Pathologic Response	40.18
Relapse	Sex	45.58
Relapse	Prior HCV	45.68
Relapse	Prior HBV	45.63
Death	Total TLS density	15.99
Death	Peritumoral TLS density	15.63
Death	Intratumoral TLS	15.99
Death	Pathologic Response	14.89
Death	Sex	17.2
Death	Prior HCV	17.85
Death	Prior HBV	16.22

1403

1404 **Extended Data Table 5 | Differentially expressed genes in TLS high and TLS low tumors.**  
1405 Each row represents a single gene, and columns provide mean of normalized counts for all  
1406 samples, log2 fold change in mRNA expression, Wald statistic, Wald test p-value, and Benjamini  
1407 Hochberg adjusted p-values.

1408  
1409 significantGenes.csv

1410  
1411 **Extended Data Table 6 | Gene Set Enrichment Results showing enriched pathways in TLS**  
1412 **high tumors compared to TLS low tumors.** Each tab corresponds to a different gene set in the  
1413 human MSigDB. Each row represents a single pathway, and columns provide the name of the  
1414 pathway, enrichment p-values, a Benjamini Hochberg adjusted p-value, the expected error for the  
1415 standard deviation of the P-value logarithm, enrichment score, enrichment score normalized to  
1416 mean enrichment of random samples of the same size, size of the pathway after removing genes  
1417 not present, and a vector with indexes of leading-edge genes that drive the enrichment.

1418  
1419 pathwayAnalysisResultsCombined.xlsx

1420  
1421

1422 **Extended Data Table 7 | Summary of antibodies selected for imaging mass cytometry.**  
1423

<b>Lymphocyte</b>	
CD45	Pan-leukocyte
CD45RA	Naïve lymphocyte
CD45RO	Antigen-experienced lymphocyte
CD3	T cell
CD4	T helper
CD8 (CD8a)	Cytotoxic T cell
CD20	B cell
CD21	Follicular dendritic cell and B cell
CD23	Follicular dendritic cell and B cell
CD138	Plasma cell
ICOS	T follicular helper
CXCR3	T follicular vs peripheral helper
CXCR5	T follicular vs peripheral helper
CCR7	Central and effector memory T cell, mature dendritic cell
FOXP3	Treg
<b>Tumor/Structural</b>	
PNAd	Lymphatic vessel
aSMA	Myofibroblast
Podoplanin	Fibroblast
Vimentin	Mesenchymal
Cytokeratin	Epithelial/Tumor
<b>Functional</b>	
CD25 (IL2R)	Activated/memory T cell
CD69	Activated/memory T cell
CD137 (4-1BB)	T cell activation
HLADR	APC, Activated T cell
PD1	T cell activation/exhaustion
PDL1	Macrophage, activated T/B, dendritic cell, epithelial
TOX	T cell activation/exhaustion
LAG3	T cell activation/exhaustion
GZMB	CTL, NK
Ki67	Proliferation Marker
BCL6	B cell GC regulator
AID	B cell somatic hypermutation
<b>Myeloid</b>	
CD11c	cDC1, cDC2
DCLAMP	Mature dendritic cell
DCSIGN	Macrophage and dendritic cell
CD57	NK cell, T cell senescence
CD68	Macrophage
CD86	DC, Langerhans cell, macrophage, B cell, other APC

1424

1425 **Extended Data Table 8 | Summary of metal-conjugated antibodies used for imaging mass**  
 1426 **cytometry.** Rows indicates a different stain, and columns indicate the metal, antigen, clone,  
 1427 dilution factor, source, and whether the antibody was custom-conjugated for the current study.  
 1428

Mass	Metal	Antigen	Clone	Dilution Factor	Source	Custom
89	Y	CD45	D9M8I	125	Cell Signaling Technology®	X
96-104	Ru	Counterstain			Electron Microscopy Sciences	
113	In	PNAd	MECA-79	250	Biolegend®	X
115	In	AID	mAID-2	125	eBioscience™	X
141	Pr	αSMA	1A4	500	Standard BioTools™	
142	Nd	Podoplanin	D2-40	125	Biolegend®	X
143	Nd	Vimentin	D21H3	500	Standard BioTools™	
144	Nd	CD11c	EP1347Y	250	Abcam	X
145	Nd	CD45RO	UCHL1	250	Biolegend®	X
146	Nd	CXCR3	IC6	100	AbboMax	X
147	Sm	CD69	EPR21814	250	Abcam	X
148	Nd	Pan-Keratin	C11	125	Standard BioTools™	
149	Sm	CD25 (IL2R)	SP176	250	Abcam	X
150	Nd	PD-L1	E1L3N	125	Cell Signaling Technology®	X
151	Eu	CXCR5	51505	250	Novus Biologicals	X
152	Sm	DC-LAMP	1010E1.01	125	Novus Biologicals	X
153	Eu	Tox/Tox2	E6I3Q	250	Cell Signaling Technology®	X
154	Sm	CD57	HNK-1	250	Cell Signaling Technology®	X
155	Gd	Foxp3	PCH101	100	Standard BioTools™	
156	Gd	CD4	EPR6855	125	Standard BioTools™	
158	Gd	ICOS	D1K2T™	250	Cell Signaling Technology®	X
159	Tb	CD68	KP1	100	Standard BioTools™	
160	Gd	Syndecan 1 (CD138)	IHC138	125	Cell Signaling Technology®	X
161	Dy	CD20	H1	125	Standard BioTools™	
162	Dy	CD8α	C8/144B	250	Standard BioTools™	
163	Dy	CD21	Bu32	250	Biolegend®	X
164	Dy	BCL-6	K112-91	250	BD Pharmingen™	X
165	Ho	PD1	EPR4877(2)	250	Abcam	X
166	Er	CD45RA	H1100	250	Standard BioTools™	
167	Er	Granzyme B	D6E9W	125	Cell Signaling Technology®	X
168	Er	Ki-67	B56	250	Standard BioTools™	
169	Tm	CD23	MRQ-57	125	Cell Marque™	X
170	Er	CD3ε	Polyclonal, C-terminal	125	Standard BioTools™	
171	Yb	Lag3	17B4	125	GeneTex	X
172	Yb	CD137 (4-1BB)	D2Z4Y	250	Cell Signaling Technology®	X
173	Yb	DC-SIGN	DCN46	62.5	lonpath	X
174	Yb	HLA-DR	LN3	250	Standard BioTools™	
175	Lu	CD86	E2G8P	125	Cell Signaling Technology®	X
176	Yb	CCR7	EPR23192-57	250	Cell Signaling Technology®	X
191	Ir	DNA 1			Standard BioTools™	
193	Ir	DNA 2			Standard BioTools™	
195	Pt	Plasma Membrane 2	1A36	250	Standard BioTools™	
196	Pt	Plasma Membrane 3	1A37	250	Standard BioTools™	
198	Pt	Plasma Membrane 4	1A38	250	Standard BioTools™	

1429

1430 **Extended Data Table 9 | Characteristics of microdissected TLS.** Each row indicates a different  
1431 patient with HCC treated with neoadjuvant immunotherapy. Columns indicate number of TLS  
1432 microdissected per patient according to location (tumor or normal adjacent) and morphology  
1433 (mature or involuted). Sample number shown differs from the final number of TCR $\beta$  and IGH  
1434 repertoires analyzed due to filtering to remove TCR $\beta$  repertoires with fewer than 500 clones and  
1435 IGH repertoires with fewer than 50 clones.  
1436

Patient	Tumor		Normal adjacent	
	Mature	Involuted	Mature	Involuted
P02	2		4	
P03	5	1		
P07			5	
P08	5			
P12	3	1		
OT1	4	1		
OT6	4	3		
<i>Total</i>	23	6	9	

1437

1438 **Extended Data Table 10 | Expanded TCR $\beta$  clones in peripheral blood after neoadjuvant**  
 1439 **ICB.**  
 1440

Patient	TCR $\beta$ sequence	pre-PBMC count	post-PBMC count	pre-PBMC freq	post-PBMC freq	pValue	fold change	present TLS
P02	CASSSLSDNYGYTF	1412	3064	0.011764608	0.025459289	2.1E-13	2.16	1
P02	CAISLDRGGGEAFF	314	687	0.002616209	0.005708398	2.8E-08	2.18	1
P02	CASKPLVWNTGELFF	0	26	0	0.000216038	2.1E-06	Inf	0
P07	CASSEPPQGQLTEAFF	0	44	0	0.000261729	2.3E-08	Inf	1
P12	CASSFGTSRRSEFF	9	127	6.6405E-05	0.000723144	7.8E-13	10.89	1
P12	CAISVDRGYSGANVLTF	9	114	6.6405E-05	0.000649121	1.9E-11	9.78	1
P12	CASSFLETQYF	16	124	0.000118053	0.000706062	1.8E-09	5.98	1
P12	CAWSRAAGGPNEQFF	63	250	0.000464835	0.001423512	5.4E-08	3.06	1
P12	CASSPGLAGDEQYF	1	33	7.37833E-06	0.000187904	7.4E-06	25.47	0
P12	CASSYTVGEYNEQFF	9873	17927	0.072846265	0.102077189	5.1E-05	1.40	1
P12	CASSLDAGASSYNSPLHF	35	125	0.000258242	0.000711756	7.1E-05	2.76	1
P12	CASSPEGQIRETQYF	1501	2954	0.011074875	0.016820216	8.5E-05	1.52	0
P12	CASSSDGAYLGTEAFF	0	21	0	0.000119575	1.0E-04	Inf	0

1441  
 1442



1443 **Extended Data Table 11 | TCR repertoire characteristics of peripheral blood and TIL single**  
 1444 **cell RNA/TCR-seq data**  
 1445 **Peripheral blood**

Cluster	Cells, <i>n</i>	Cells with TCR, <i>n</i>	Cells with expanded TCR, <i>n</i> (%)	Cells with TCR $\beta$ in TLS, <i>n</i> (%)
CD4 Naive	615	590	47 (8)	16 (2.7)
CD8 Naive	848	807	88 (10.9)	11 (1.4)
MAIT	315	217	108 (49.8)	129 (59.4)
CD4 Naive-like	8580	7224	806 (11.2)	604 (8.4)
CD4 TCM	2677	2531	464 (18.3)	767 (30.3)
CD4 Tph	1088	988	113 (11.4)	188 (19)
CD4 TEM_GZMK	1271	1086	384 (35.4)	702 (64.6)
CD4 TEM_GZMB	942	698	660 (94.6)	601 (86.1)
CD8 TCM	892	785	164 (20.9)	202 (25.7)
CD8 TEM_GZMK	1906	1676	1147 (68.4)	1390 (82.9)
CD8 TEM_GZMB	2551	1963	1682 (85.7)	1569 (79.9)
CD8 TRM	212	91	41 (45.1)	52 (57.1)
NK-T	75	32	25 (78.1)	22 (68.8)
Treg	801	712	106 (14.9)	70 (9.8)
dnT	267	116	23 (19.8)	23 (19.8)
gdT	132	30	7 (23.3)	3 (10)
<b>Total</b>	<b>23172</b>	<b>19546</b>	<b>5865 (30)</b>	<b>6349 (32.5)</b>

1446 **TIL**  
 1447

Cluster	Cells, <i>n</i>	Cells with TCR, <i>n</i>	Cells with expanded TCRs, <i>n</i> (%)	Cells with TCR $\beta$ in TLS, <i>n</i> (%)
CD4 Naive-like	38	11	3 (27.3)	8 (72.7)
CD4 TCM	28	14	1 (7.1)	10 (71.4)
CD4 Tph	31	29	7 (24.1)	24 (82.8)
CD4 TEM_GZMK	76	48	10 (20.8)	40 (83.3)
CD8 TCM	53	10	3 (30)	7 (70)
CD8 TEM_GZMK	194	147	68 (46.3)	121 (82.3)
CD8 TEM_GZMB	37	28	16 (57.1)	24 (85.7)
CD8 TRM	36	25	14 (56)	18 (72)
Treg	22	17	3 (17.6)	8 (47.1)
dnT	28	3	1 (33.3)	3 (100)
MAIT	19	14	10 (71.4)	10 (71.4)
<b>Total</b>	<b>562</b>	<b>346</b>	<b>136 (39.3)</b>	<b>273 (78.9)</b>

1448

1449

1450 **Extended Data Table 12 | Association of peripheral blood and TIL single cell clusters with**  
 1451 **clonal expansion.<sup>°†</sup>**

1452  
 1453 **Peripheral blood**

<b>Cluster</b>	<b>P value</b>	<b>OR</b>	<b>95%_CI_Lower</b>	<b>95%_CI_Upper</b>
CD4 TEM_GZMB	< 0.001	31.48	25.72	38.83
CD8 TEM_GZMB	< 0.001	17.99	16.17	20.04
NK-T	< 0.001	10.27	4.73	23.62
Treg	< 0.001	9.02	5.42	16.23
CD8 TEM_GZMK	< 0.001	6.27	5.63	6.97
MAIT	0.398	0.82	0.54	1.22
CD8 TRM	0.389	0.73	0.35	1.39
gdT	0.614	0.59	0.12	1.93
CD4 TEM_GZMK	< 0.001	0.4	0.32	0.51
dnT	0.002	0.34	0.13	0.73
CD8 TCM	< 0.001	0.28	0.2	0.38
CD4 TCM	< 0.001	0.13	0.1	0.17
CD8 Naive	< 0.001	0.08	0.04	0.14
CD4 Naive	< 0.001	0.05	0.02	0.12
CD4 Naive-like	< 0.001	0.04	0.03	0.05
CD4 Tph	< 0.001	0.04	0.01	0.07

1454  
 1455 **TIL**

<b>Cluster</b>	<b>P value</b>	<b>OR</b>	<b>95%_CI_Lower</b>	<b>95%_CI_Upper</b>
Treg	0.03	Inf	1.2	Inf
CD8 TEM_GZMB	0.003	3.49	1.45	8.32
CD8 TRM	0.056	2.25	0.88	5.49
CD8 TEM_GZMK	0.013	1.94	1.12	3.36
MAIT	0.518	1.44	0.32	5.19
CD8 TCM	0.689	1.19	0.12	6.83
CD4 Tph	0.159	0.39	0.07	1.32
CD4 TEM_GZMK	< 0.001	0.13	0.02	0.53
CD4 TCM	0.046	0	0	1.05
CD4 Naive-like	0.131	0	0	1.4
dnT	1	0	0	8.64

1456 <sup>°</sup>Clonal expansion defined as greater than 5 cells per unique TCRαβ in the peripheral blood

1457 dataset and greater than 2 in TIL.

1458 † Fisher's Exact test

1459

1460 **Extended Data Table 13 | Association of peripheral blood and TIL single cell clusters with**  
 1461 **detection in TLS.†**

1462  
 1463 **Peripheral blood**

Cluster	P value	OR	95%_CI_Lower	95%_CI_Upper
CD4 TEM_GZMB	< 0.001	14.12	11.35	17.72
CD8 TEM_GZMK	< 0.001	12.65	11.08	14.48
CD8 TEM_GZMB	< 0.001	10.66	9.49	12
Treg	< 0.001	4.59	3.57	5.97
NK-T	< 0.001	4.58	2.08	10.85
CD4 TEM_GZMK	< 0.001	4.15	3.64	4.73
MAIT	< 0.001	3.09	2.33	4.11
CD8 TRM	< 0.001	2.79	1.8	4.34
CD4 TCM	0.012	0.89	0.81	0.98
CD8 TCM	< 0.001	0.71	0.6	0.84
dnT	0.003	0.51	0.31	0.82
CD4 Tph	< 0.001	0.47	0.4	0.56
gdT	0.006	0.23	0.04	0.75
CD4 Naive-like	< 0.001	0.1	0.1	0.11
CD4 Naive	< 0.001	0.06	0.03	0.09
CD8 Naive	< 0.001	0.03	0.01	0.05

1464  
 1465 **TIL**

Cluster	P value	OR	95%_CI_Lower	95%_CI_Upper
CD8 TCM	0.445	1.63	0.26	7.35
CD4 TCM	0.505	1.52	0.34	5.48
MAIT	0.505	1.52	0.34	5.48
CD8 TRM	0.444	1.5	0.51	3.96
CD4 Naive-like	0.706	1.42	0.24	6.11
CD4 Tph	0.812	0.76	0.22	2.15
CD4 TEM_GZMK	0.567	0.72	0.28	1.66
CD8 TEM_GZMK	0.23	0.7	0.39	1.22
CD8 TEM_GZMB	0.472	0.6	0.15	1.84
Treg	0.003	0.22	0.07	0.66
dnT	1	0	0	9.1

1466 † Fisher's Exact test

1467

1468

1469

1470 **Extended Data Table 14 | Match rate of TLS TCR $\beta$  in single cell sequencing of post-**  
 1471 **treatment peripheral blood and TIL.**

1472  
 1473 **Peripheral Blood**

Patient	Total TCR $\beta$ , <i>n</i> (%)	Top 10% of TCR $\beta$ , <i>n</i> (%)	Top 1% of TCR $\beta$ , <i>n</i> (%)	Top 0.1% of TCR $\beta$ , <i>n</i> (%)
P02	274/11783 (2.3)	130/1178 (11)	52/118 (44.1)	8/12 (67)
P03	114/10872 (1)	39/1087 (3.6)	15/109 (13.8)	2/11 (18)
P07	624/11623 (5.4)	276/1162 (24)	61/116 (52.6)	11/12 (92)
P08	742/33681 (2.2)	374/3368 (11)	123/337 (36.5)	20/34 (59)
P12	422/7025 (6)	161/702 (23)	38/70 (54.3)	6/7 (86)
OT1	58/2740 (2.1)	39/274 (14)	9/27 (33.3)	1/3 (33)
OT6	674/58185 (1.2)	237/5818 (4.1)	71/582 (12.2)	15/58 (26)
Total	2908 / 135909 (2.1)	1256/13589 (9.2)	369/1359 (27.2)	63/137 (46)

1474  
 1475 **TIL**

Patient	Total TCR $\beta$ , <i>n</i> (%)	Top 10% of TCR $\beta$ , <i>n</i> (%)	Top 1% of TCR $\beta$ , <i>n</i> (%)	Top 0.1% of TCR $\beta$ , <i>n</i> (%)
OT6	196/58185 (0.34)	135/5818 (2.3)	76/582 (13.1)	24/58 (41)

1476

1477 **Extended Data Table 15 | Summary of antibodies used for immunohistochemistry.** Each  
1478 row indicates a different stain, and columns indicate the target, antigen retrieval buffer used,  
1479 clone, vendor, product ID and concentration. For dual IHC stains, first and second antibody are  
1480 indicated.  
1481

Target	Antigen retrieval buffer	First antibody			Second antibody		
		Clone	Vendor	Conc. (µg/mL)	Clone	Vendor	Conc. (µg/mL)
CD20	low pH sodium citrate	L26	Leica	0.114			
CD21/CD3	low pH sodium citrate	2G9	Leica	4.075	LN10	Leica	0.213
CD8/CD4	high pH EDTA	4B11	Leica	0.114	ER204	Millipore Sigma	0.096
Ki67/CD20	high pH EDTA	MM1	Leica	0.42	L26	Leica	0.19

1482

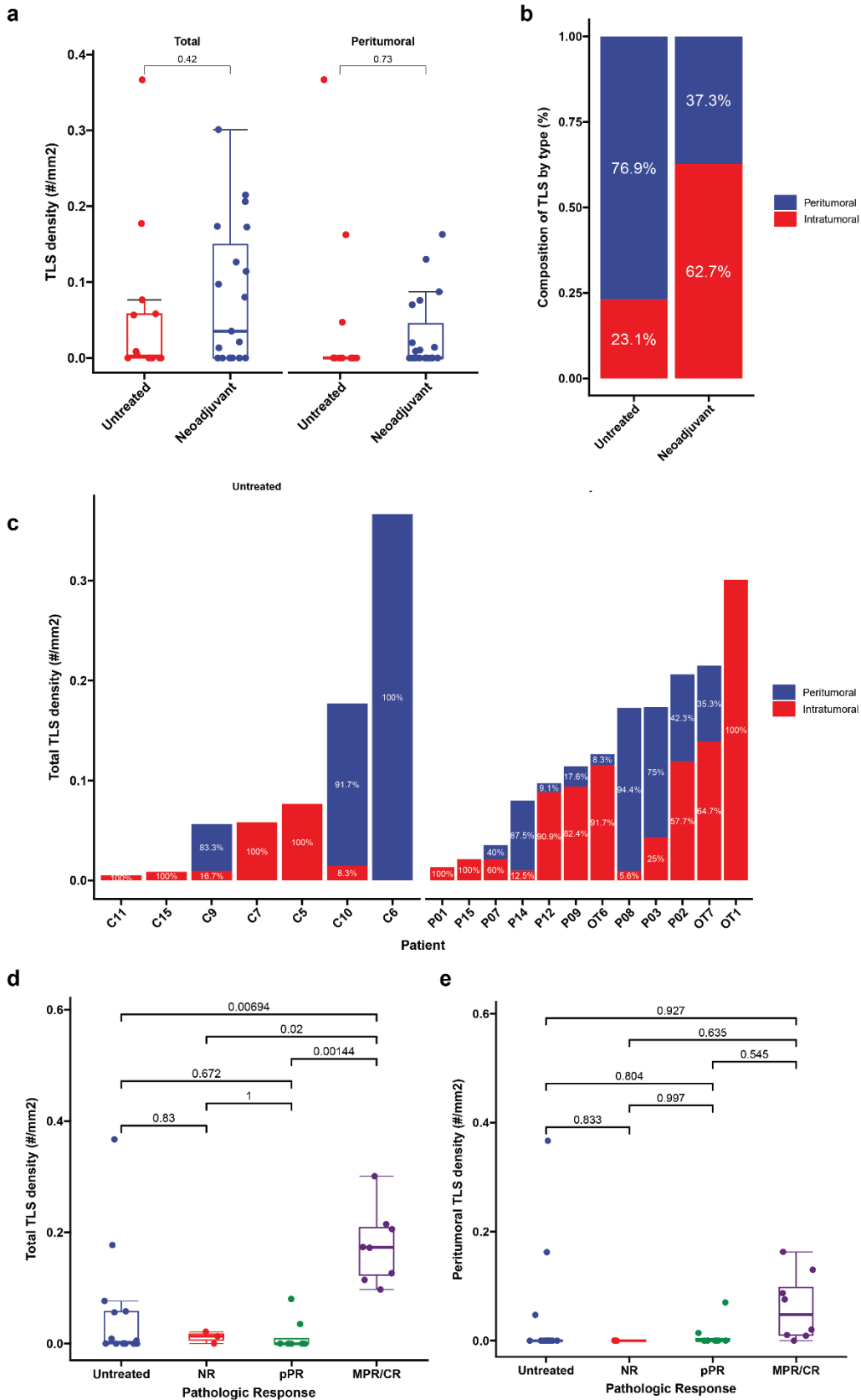
1483 **Extended Data Table 16 | Summary of antibodies used for FACS.**  
1484

<b>Antibody</b>	<b>Clone</b>	<b>Vendor</b>	<b>Dilution</b>
Live/Dead	Zombie NIR	Biologend	1:1000
CD3-FITC	HIT3a	Biologend	1:100
CD19-PE/dazzle	SJ25C1	Biologend	1:200
Fc Block	N/A	Biologend	1:100

1485

1486

1487 **EXTENDED DATA**

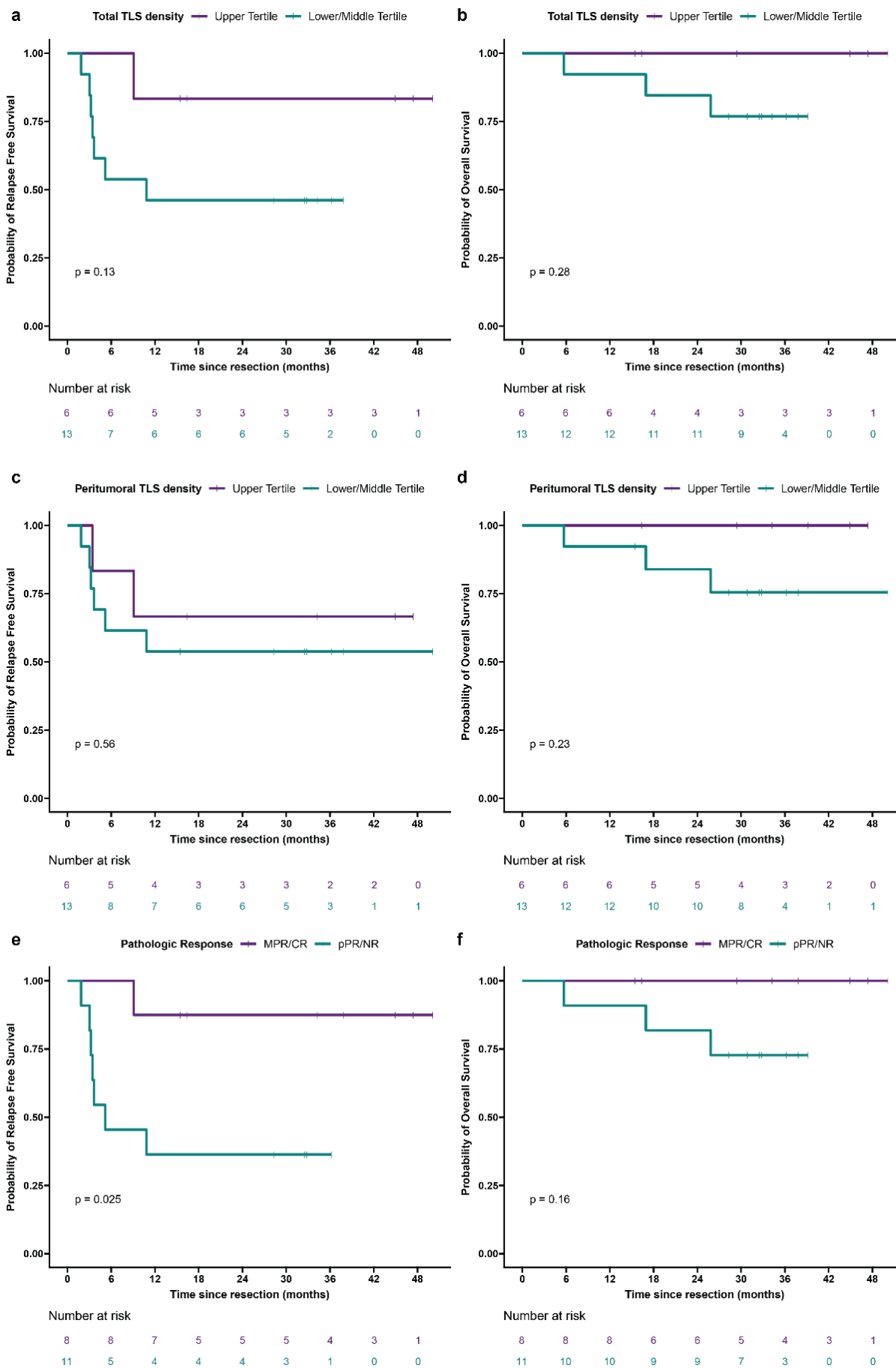


1488

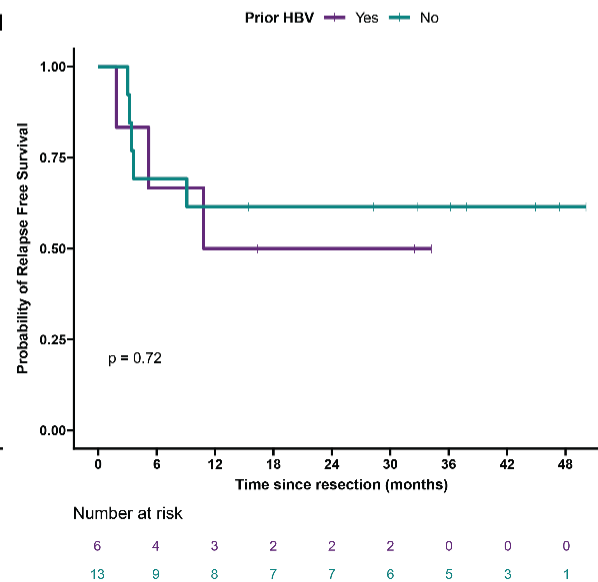
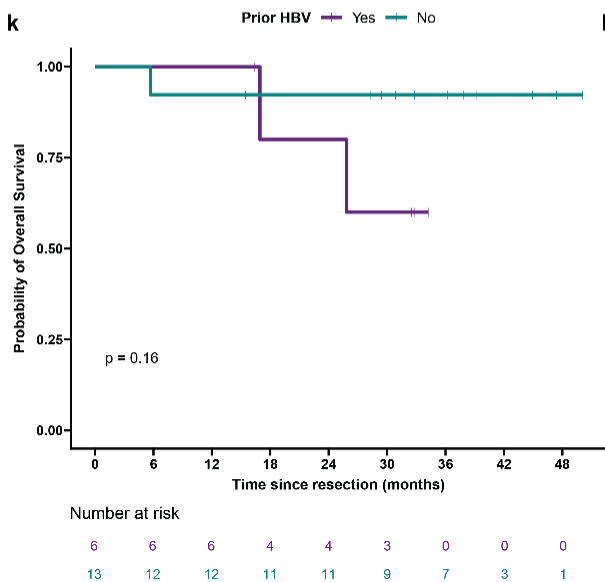
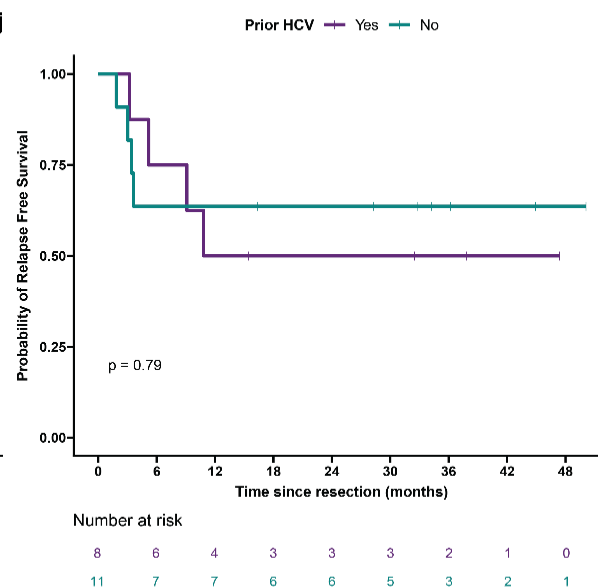
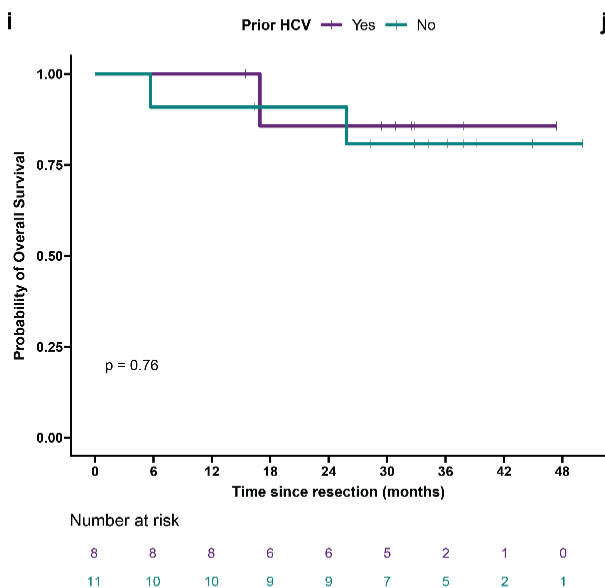
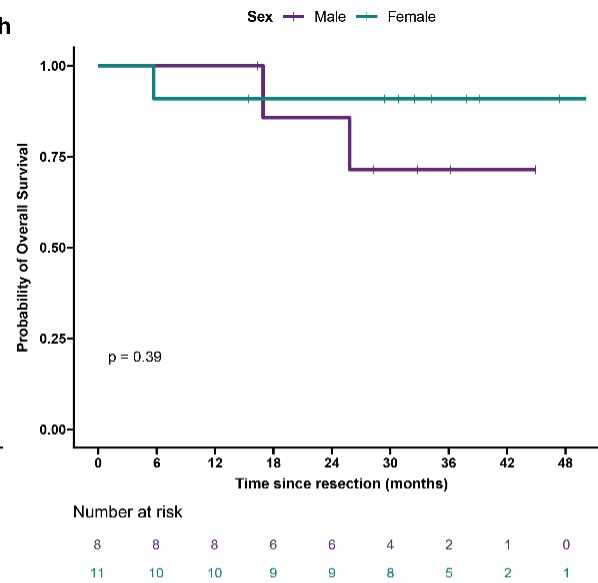
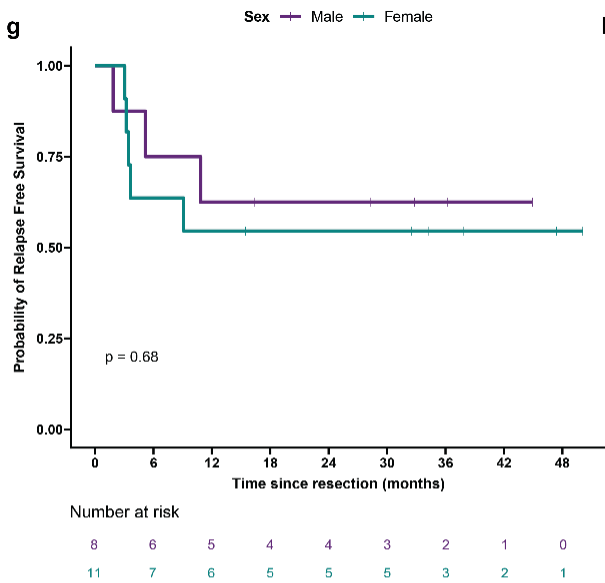
1489 **Extended Data Fig. 1 | TLS density in HCC tumors treated with neoadjuvant ICB and**  
1490 **untreated controls. a,** Box-and-whisker plots showing total and peritumoral TLS density in  
1491 patients with locally advanced HCC treated with neoadjuvant ICB ( $n = 19$ ) and untreated controls  
1492 ( $n = 14$ ). **b-c,** Stacked barplots showing proportion of TLS comprised of peritumoral versus  
1493 intratumoral TLS location neoadjuvant treated and untreated HCC tumors (**b**) and by patient (**c**).  
1494 Labels indicate proportion of total TLS comprised of peritumoral or intratumoral TLS. In **c**, patients  
1495 with no observed TLS are not shown. **d-e,** Box-and-whisker plots showing total (**d**) and  
1496 peritumoral (**e**) TLS density in untreated ( $n = 14$ ) and neoadjuvant treated tumors, divided  
1497 according to pathologic response ( $n = 19$ ). Statistical significance was determined by two-tailed  
1498 t-test (**a**) and one-way ANOVA followed by Tukey's honest significant difference (HSD) test (**d**  
1499 and **e**).  
1500



1501  
1502



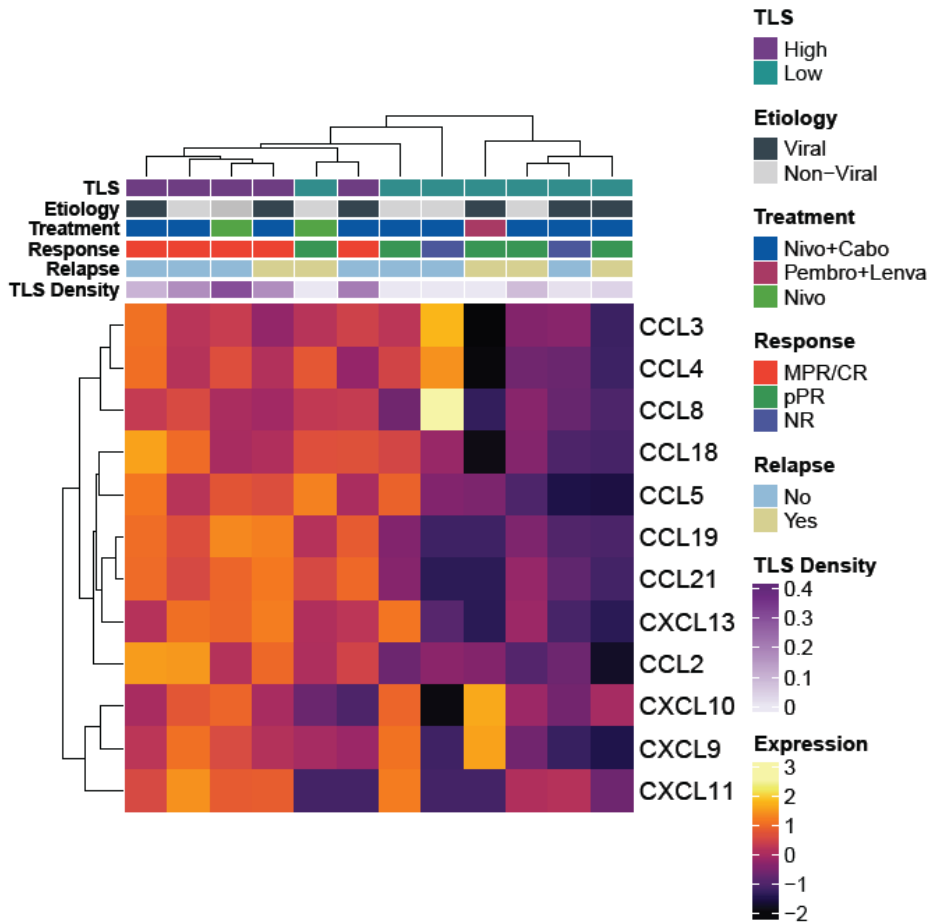
1503



1504 **Extended Data Fig. 2 | Relapse free survival and overall survival in HCC cohort treated with**  
1505 **neoadjuvant ICB, according to clinical covariates. a—l,** Kaplan-Meier curves showing relapse  
1506 free survival and overall survival after surgical resection for HCC patients treated with neoadjuvant  
1507 ICB ( $n = 19$ ), according to total TLS density (**a** and **b**), peritumoral TLS density (**c** and **d**),  
1508 pathologic response (**e** and **f**), sex (**g** and **h**), prior hepatitis C (HCV) infection (**i** and **j**), and prior  
1509 hepatitis B (HBV) infection (**k** and **l**). Statistical significance was determined by log-rank test.  
1510

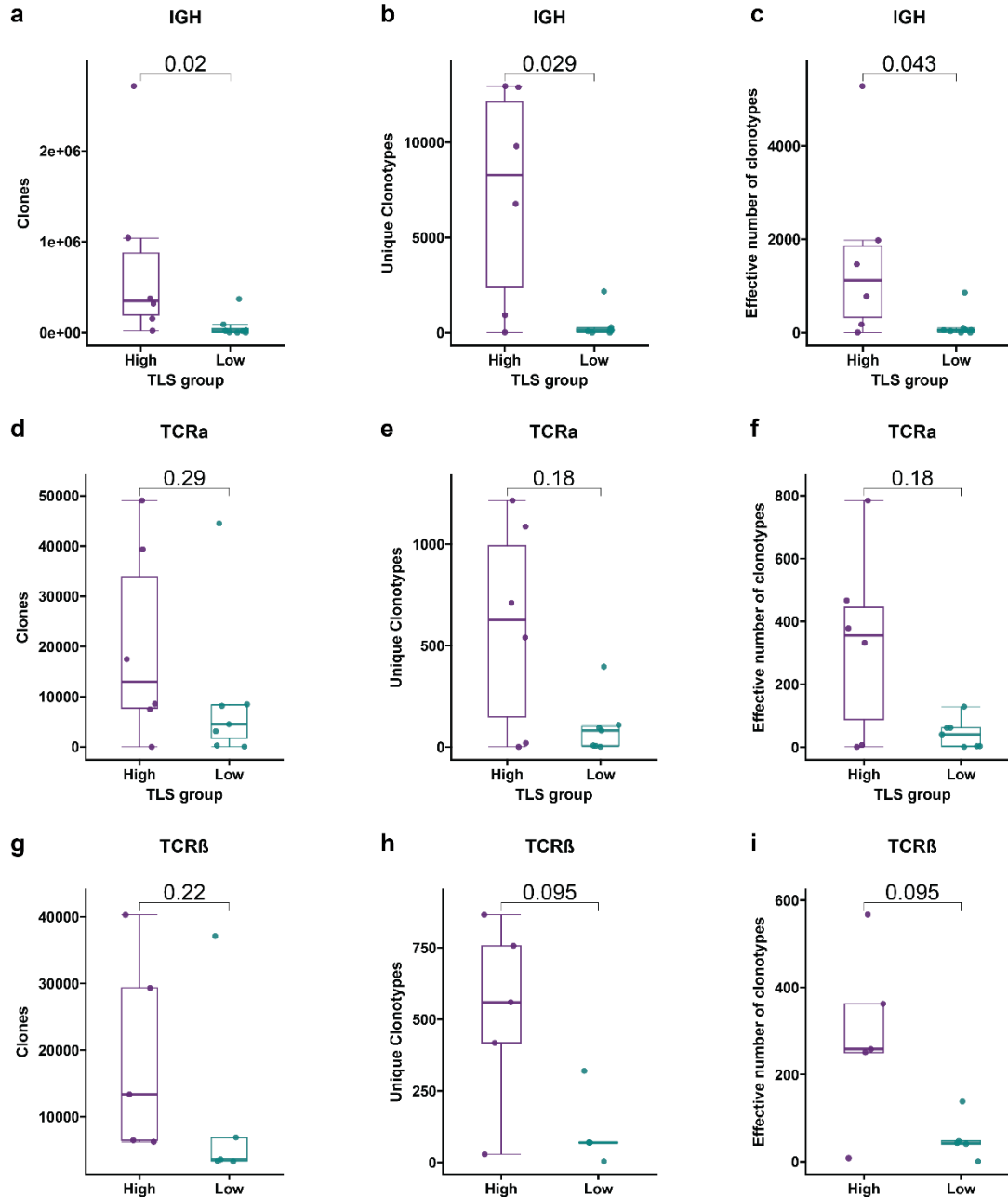
1511  
1512  
1513  
1514  
1515  
1516  
1517  
1518  
1519  
1520  
1521  
1522  
1523  
1524  
1525  
1526  
1527  
1528  
1529  
1530  
1531  
1532  
1533  
1534  
1535  
1536  
1537  
1538  
1539  
1540  
1541  
1542  
1543  
1544  
1545

**a**



**Extended Data Fig. 3 | High TLS density after neoadjuvant ICB is associated with increased expression of the 12-chemokine TLS gene signature. a,** Heatmap showing expression of the 12-chemokine gene signature in tumors with high TLS density ( $n = 5$ ) and low TLS density ( $n = 7$ ). Annotation rows indicate TLS group, HCC etiology, neoadjuvant treatment, pathologic response, relapse, and TLS density.

1546



1547

1548

1549

1550 **Extended Data Fig. 4 | HCC tumors with high TLS density after neoadjuvant ICB have**

1551 **expanded T and B cell repertoires compared to tumors with low TLS density.** Box-and-

1552 whisker plots showing the total clones, unique clonotypes, and effective number of clonotypes

1553 (i.e. true diversity index) for the immunoglobulin heavy chain (IGH) (a-c), TCRα (d-f), and TCRβ

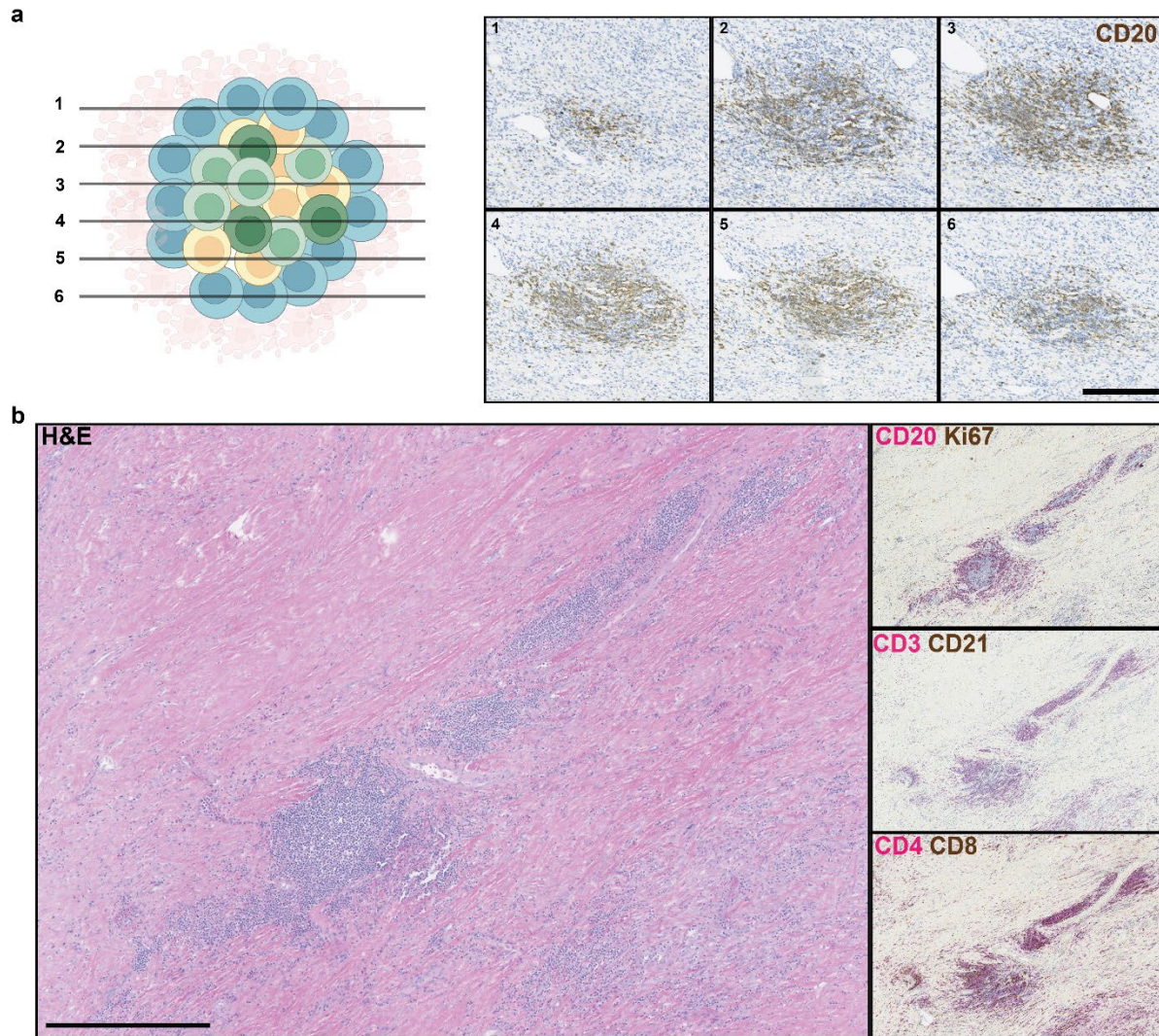
1554 (g-i) repertoires of HCC tumors with high and low TLS density after neoadjuvant ICB. For each

1555 box-and-whisker plot, the horizontal bar indicates the median, the upper and lower limits of the

1556 boxes the interquartile range, and the ends of the whiskers 1.5 times the interquartile range.

1557 Statistical significance was determined by Wilcoxon rank sum test.

1558



1559

1560

1561

1562

1563

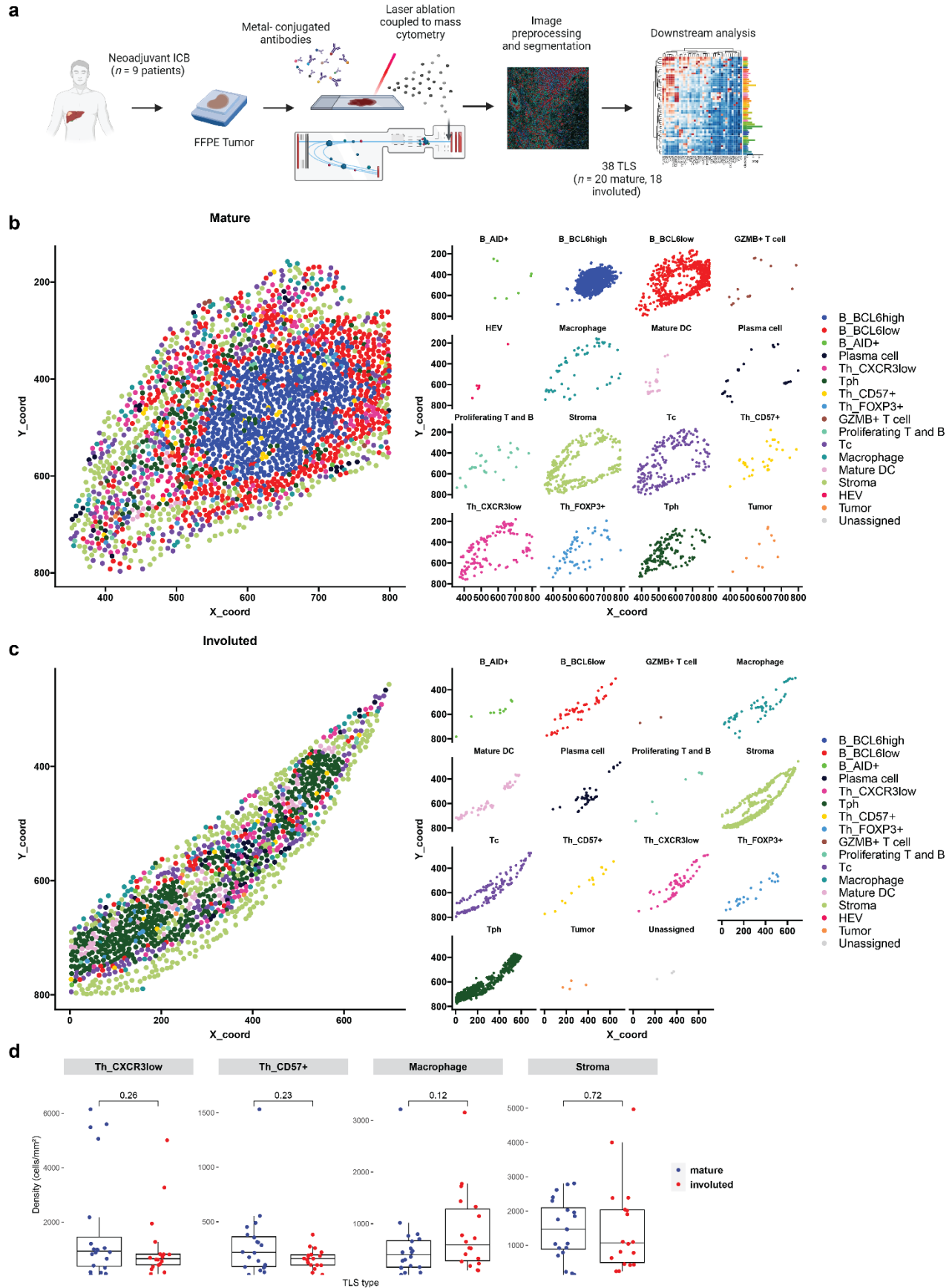
1564

1565

1566

1567

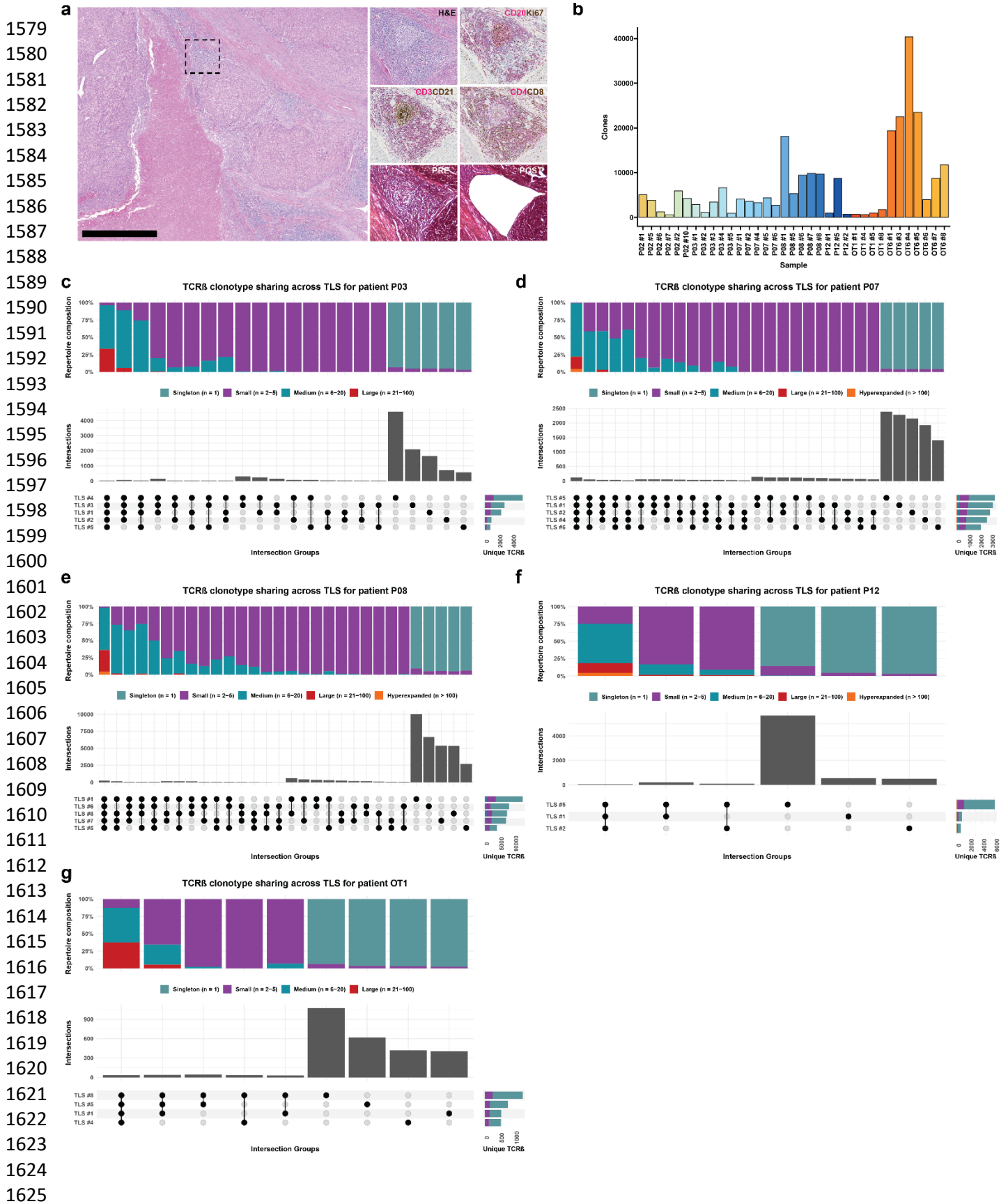
**Extended Data Fig. 5 | Involved TLS in an HCC tumor with complete pathologic response after neoadjuvant ICB (OT7).** **a**, Serial FFPE sections of an involuted TLS stained with anti-CD20 antibody (brown). Numbered images indicate the order in which the sections were cut from the tissue block. Scale bar, 250  $\mu$ m. **b**, Representative images of multiple involuted TLS (red arrows) stained with hematoxylin and eosin (H&E), anti-CD20 (magenta) and anti-Ki67 (brown) (right middle), anti-CD3 (magenta) and anti-CD21 (brown) (middle right), and anti-CD4 and anti-CD8 (bottom right).

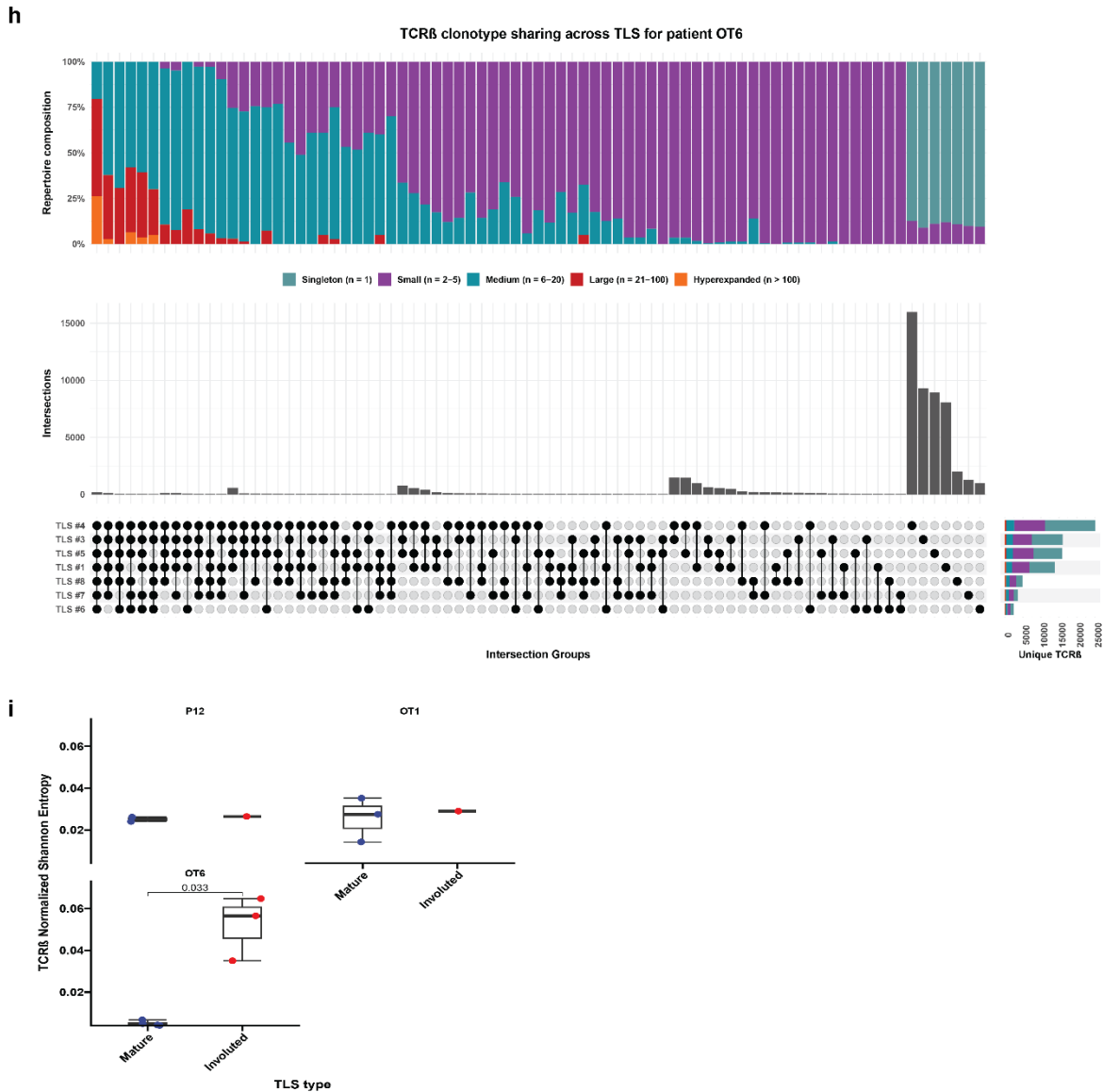


1569 **Extended Data Fig. 6 | Characterization of divergent TLS morphologies in viable tumor and**  
1570 **tumor regression bed by imaging mass cytometry. a,** Imaging mass cytometry workflow. **b-c,**  
1571 Dot plots showing representative mature **(b)** and involuted **(c)** TLS, colored according to cluster  
1572 assignment of individual cells after cell segmentation. **(d)** Box-and-whisker plots showing cell  
1573 cluster density in mature versus involuted TLS for CXCR3<sup>low</sup> CD4 T cells, CD57<sup>+</sup> CD4 T cells,  
1574 Macrophages, and Stroma. For each box-and-whisker plot, the horizontal bar indicates the  
1575 median, the upper and lower limits of the boxes the interquartile range, and the ends of the  
1576 whiskers 1.5 times the interquartile range. Statistical significance was determined by pairwise two  
1577 sample Wilcoxon test **(d)**.

1578



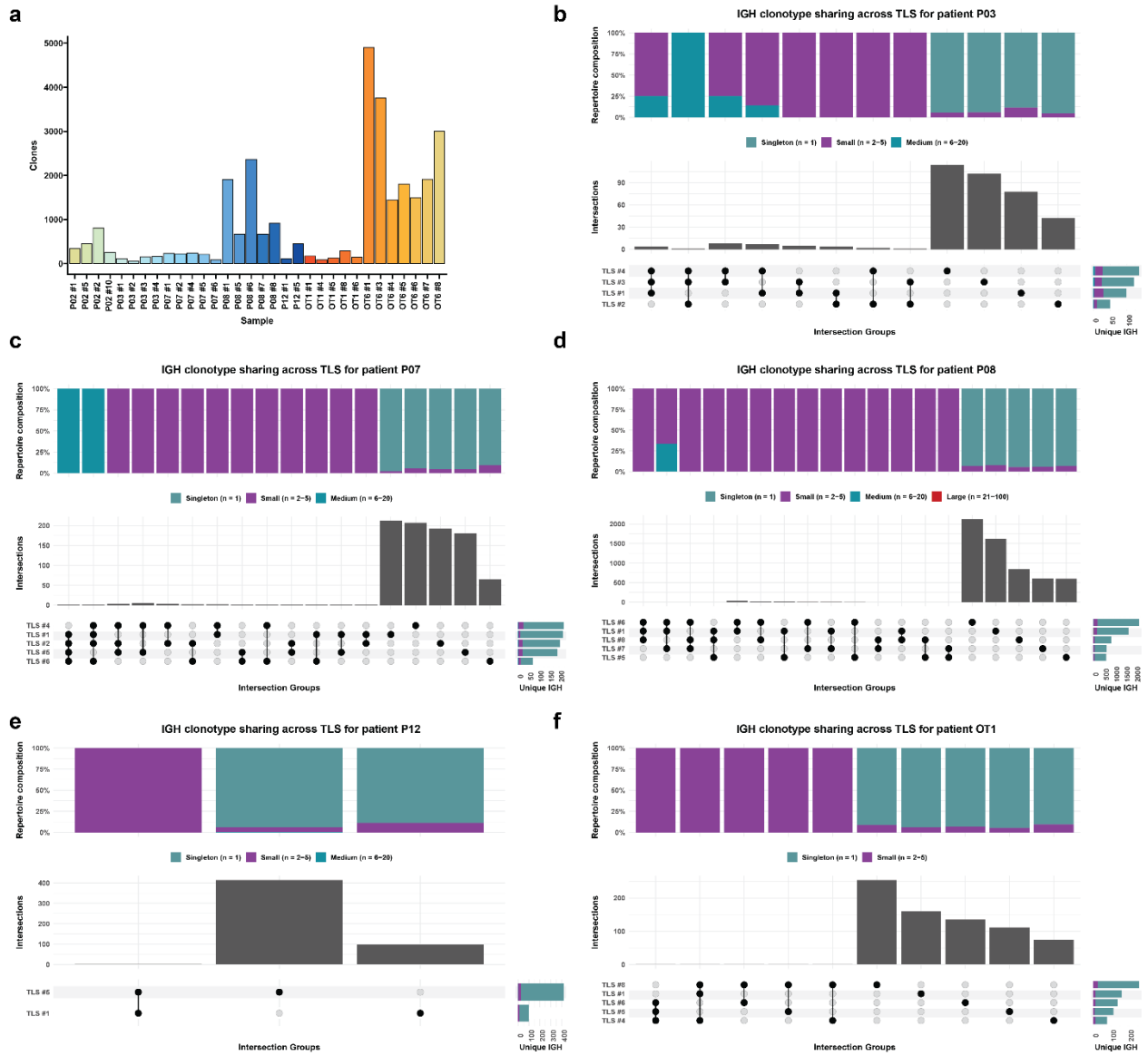




1626  
1627  
1628  
1629  
1630  
1631  
1632  
1633  
1634  
1635  
1636  
1637  
1638  
1639  
1640  
1641

**Extended Data Fig. 7 | TCR $\beta$  repertoire features of microdissected TLS.** **a**, Representative images showing method of identification and microdissection of individual TLS. Image on left shows HCC tumor stained with hematoxylin and eosin (H&E) at low magnification. Insets show higher magnification of staining with H&E, anti-CD20 (magenta) and anti-Ki67 (brown), anti-CD3 (magenta) and anti-CD21 (brown), anti-CD4 and anti-CD8 (bottom right), and corresponding pre- and post-microdissection images. Scale bar, 1mm. **b**, Barplot showing total clone count across all microdissected TLS. **c-h**, Representative upset plots showing overlap in TCR $\beta$  clonotypes across microdissected TLS from patients P03 (**c**), P07 (**d**), P08 (**e**), P12 (**f**), OT1 (**g**), and OT6 (**h**). For each upset plot, barplots in gray and row below indicate number of overlapping clonotypes between different combinations of TCR $\beta$  repertoires. Stacked barplots at top indicate repertoire composition of different groups of TCR $\beta$  and at bottom right indicate total number of unique TCR $\beta$  clonotypes identified in each TLS, colored according to clonal expansion. Intersections with fewer than 20 unique clonotypes are not shown. **i**, Dotplot showing TCR $\beta$  repertoire clonality (as determined by Normalized Shannon Entropy) for matched mature and involuted TLS. Statistical significance was determined by two-tailed t test (**i**).

1642  
1643  
1644  
1645  
1646  
1647  
1648  
1649  
1650  
1651  
1652  
1653



1654

1655

1656

1657

1658

1659

1660

1661

1662

1663

1664

1665

1666

1667

1668

1669

1670

1671

1672

1673

1674

1675

1676

1677

1678

1679

1680

1681

1682

1683

1684

1685

1686

1687

1688

1689

1690

1691

1692

1693

1694

1695

1696

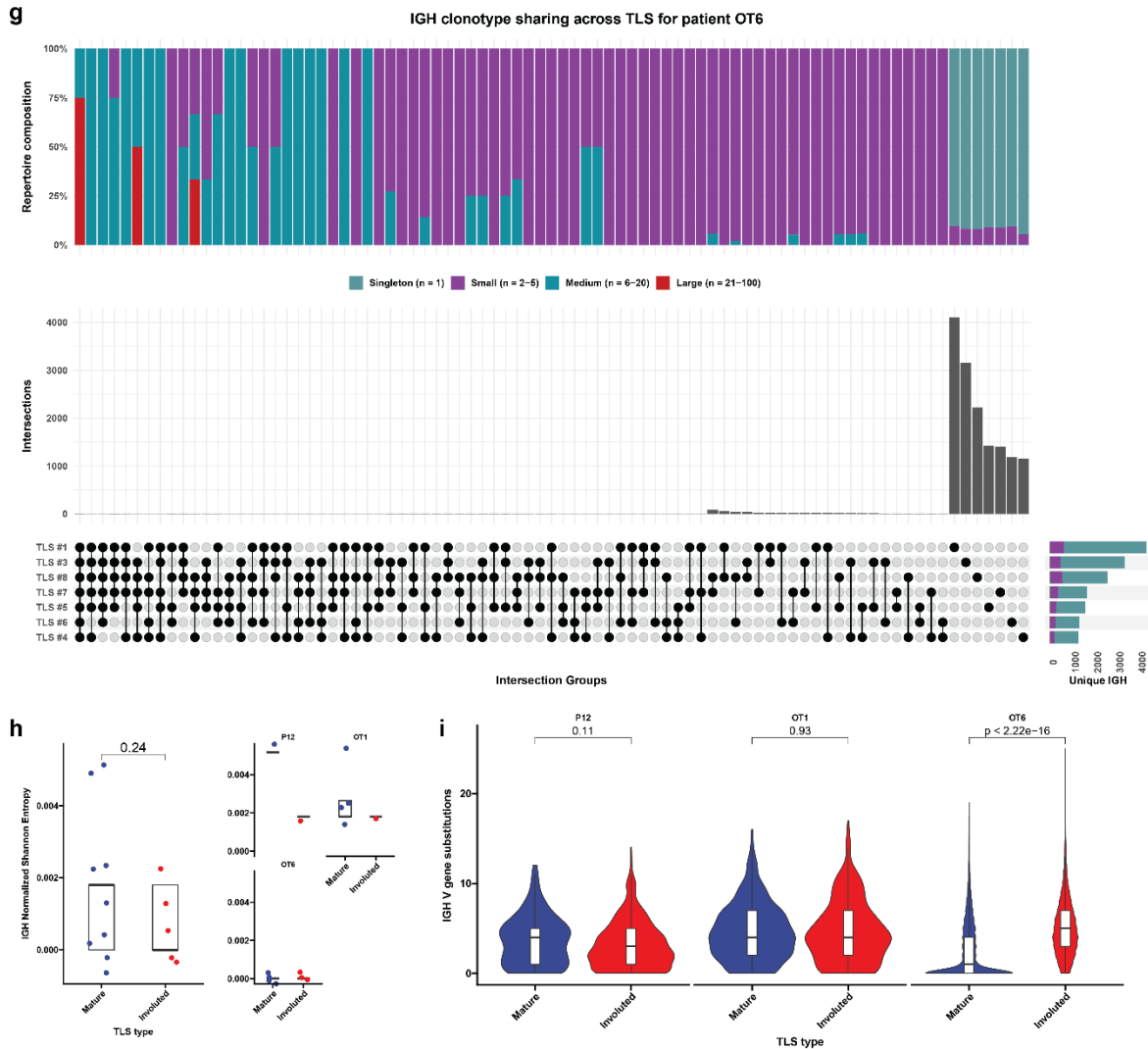
1697

1698

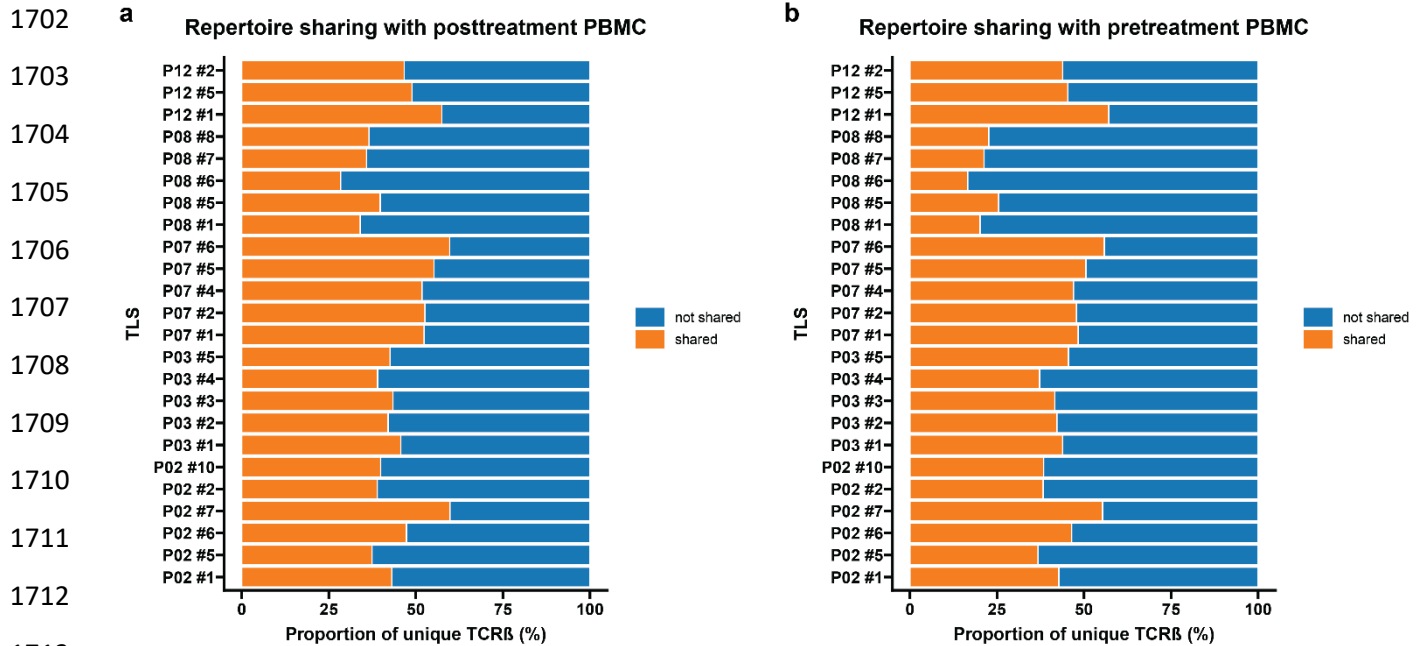
1699

1700

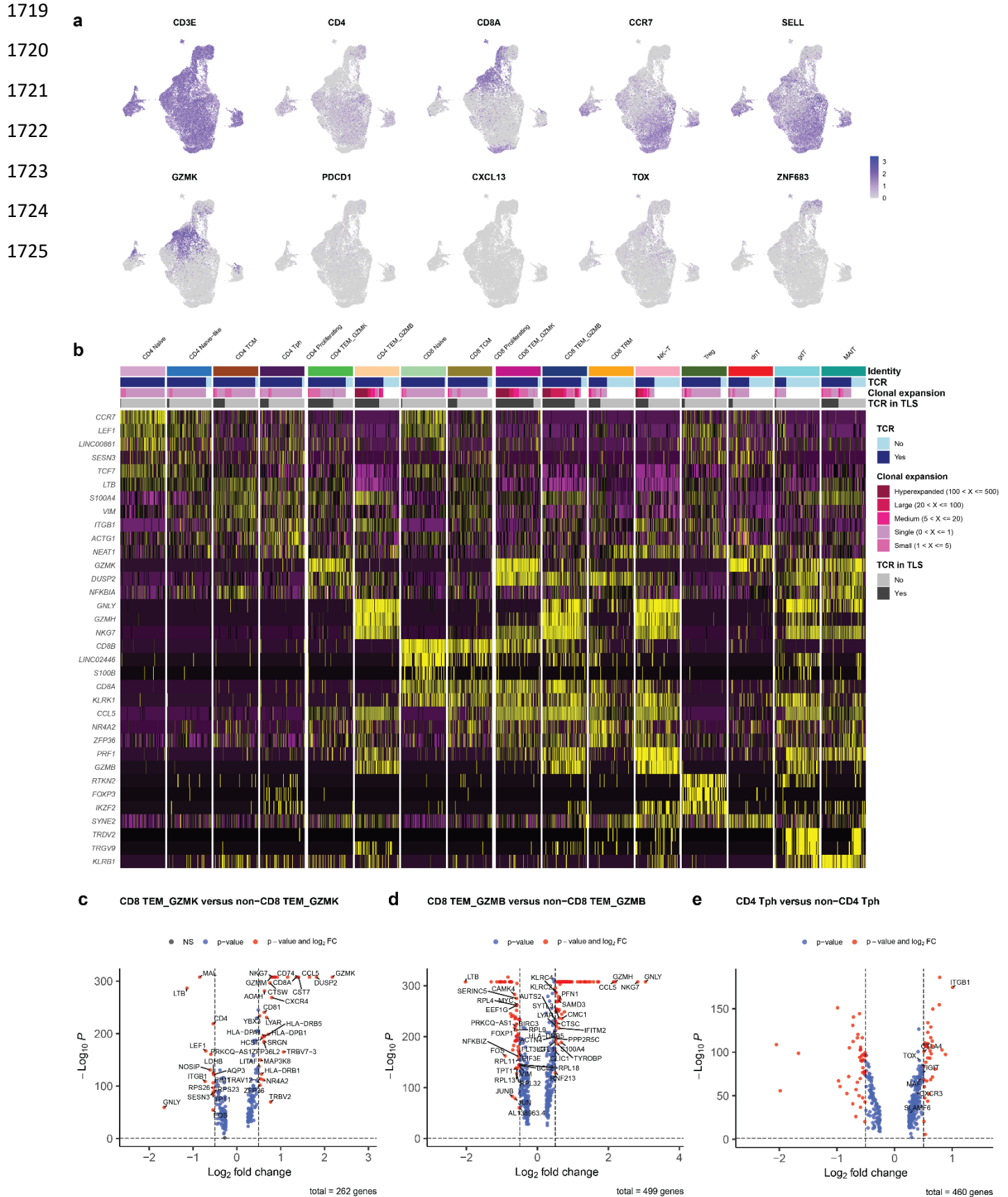
1701



**Extended Data Fig. 8 | IGH repertoire features of microdissected TLS.** **a**, Stacked barplot showing IGH repertoire composition across all TLS. **b-f**, Representative upset plots showing overlap in unique IGH clonotypes across microdissected TLS from patients P03 (**b**), P07 (**c**), P08 (**d**), P12 (**e**), OT1 (**f**), and OT7 (**g**). Bottom barplots and annotation row indicate number of overlapping clonotypes between different TLS repertoires. Top stacked barplots indicate clonal composition of overlapping (“public IGH”) and nonoverlapping (“Private IGH”). Bottom right stacked barplots indicate total number of unique IGH clonotypes identified at each TLS and overall clonal composition. **h**, Dotplot showing IGH repertoire clonality (as determined by Normalized Shannon Entropy) for microdissected TLS, according to TLS morphology. Statistical significance was determined by two-tailed t test (**h** and **i**).

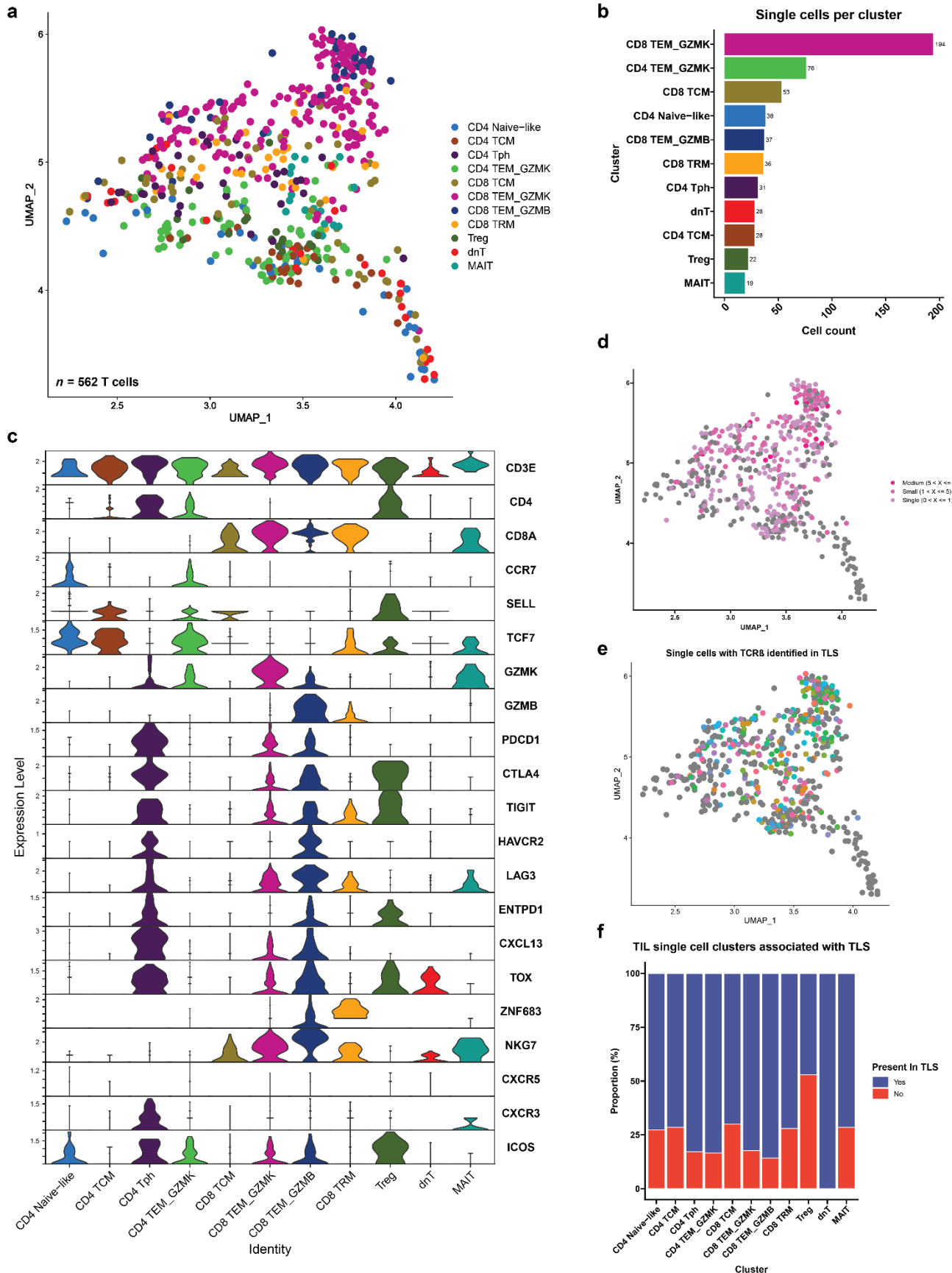


**Extended Data Fig. 9 | TLS display a high degree of T cell repertoire overlap with pre- and post-treatment peripheral blood. a-b,** Barplots showing proportion of unique TCR $\beta$  clonotypes at each TLS that also identified in matched pre-treatment (a) and post-treatment (b) peripheral blood.



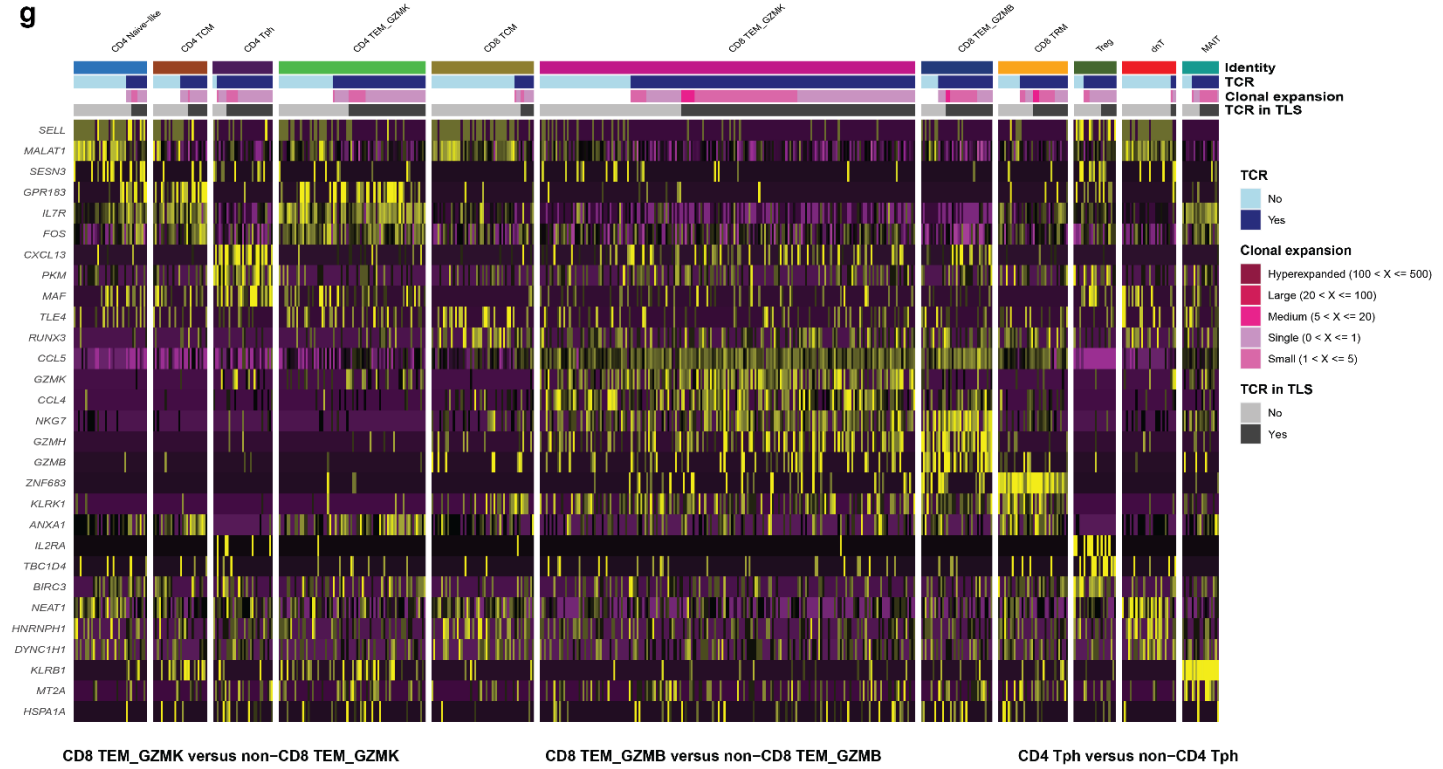
1726 **Extended Data Fig. 10 | Single cell sequencing of post-treatment peripheral blood. a,**  
1727 UMAPs showing gene expression of *CD3E*, *CD4*, *CD8A*, *CCR7*, *SELL*, *GZMK*, *PDCD1*, *CXCL13*,  
1728 *TOX*, and *ZNF683* across all single cells sequenced from post-treatment peripheral blood of 7  
1729 HCC patients treated with neoadjuvant ICB. **b,** Heatmap showing gene expression of the top 3  
1730 differentially expressed genes per cluster. Rows represent single genes and columns represent  
1731 individual cells. Annotation bar indicates cluster identity, whether each cell had a sequenced TCR,  
1732 the clonality of the TCR, and whether the TCR was identified in microdissected TLS from the  
1733 same patient. Clusters were downsampled to 75 cells per cluster for visualization. **c-e,** Volcano  
1734 plots showing differentially expressed genes in the CD8 TEM\_GZMK (**b**), CD8 TEM\_GZMB (**c**),  
1735 and CD4 Tph (**d**) clusters compared to all other cells. Vertical dotted lines indicates a fold change  
1736 of greater or less than 1.4 and horizontal line indicates a P value of 0.05. Labeled genes in **c** and  
1737 **d** indicate genes with the highest differential expression. Labeled genes in **e** indicate genes known  
1738 to be highly expressed in CD4 Tph.  
1739

1740  
1741  
1742

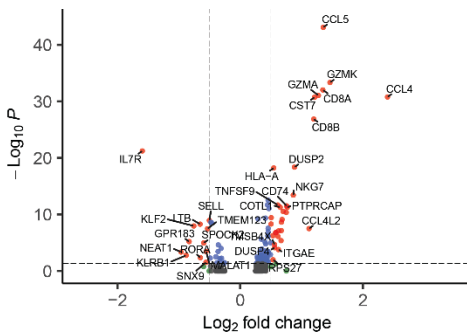




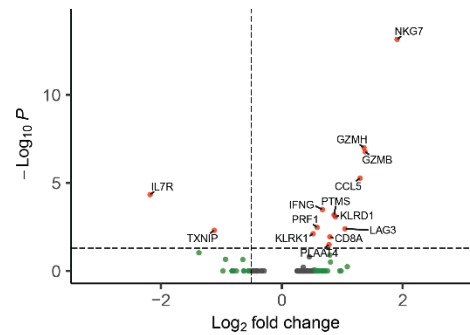
1743 **g**



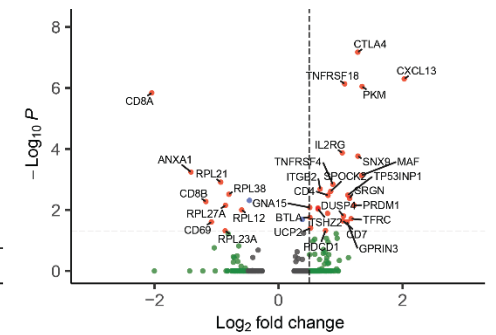
**h**      • NS    • Log<sub>2</sub> FC    • p-value    • p-value and log<sub>2</sub> FC



**i**      • NS    • Log<sub>2</sub> FC    • p-value and log<sub>2</sub> FC

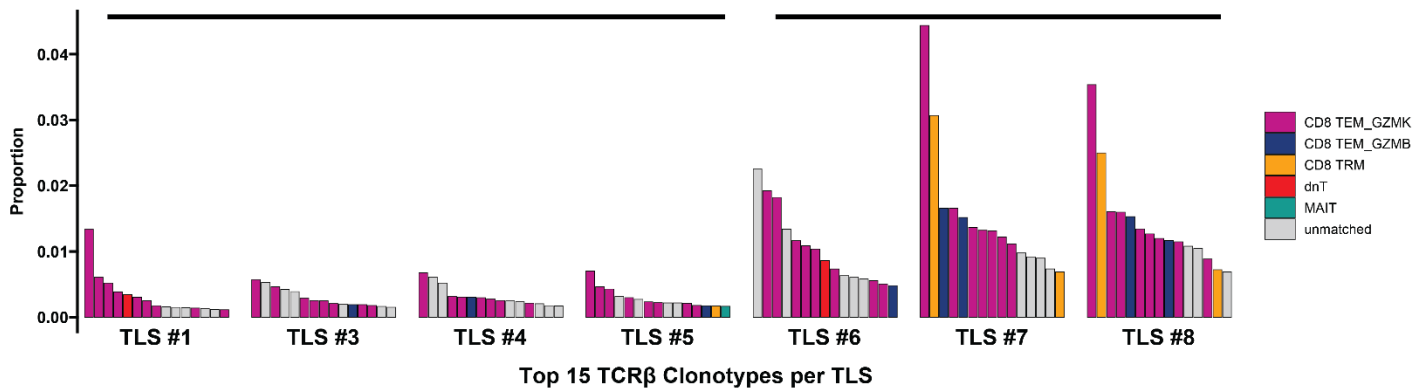


**j**      • NS    • Log<sub>2</sub> FC    • p-value    • p-value and log<sub>2</sub> FC



**k**      **Mature**

**Involved**

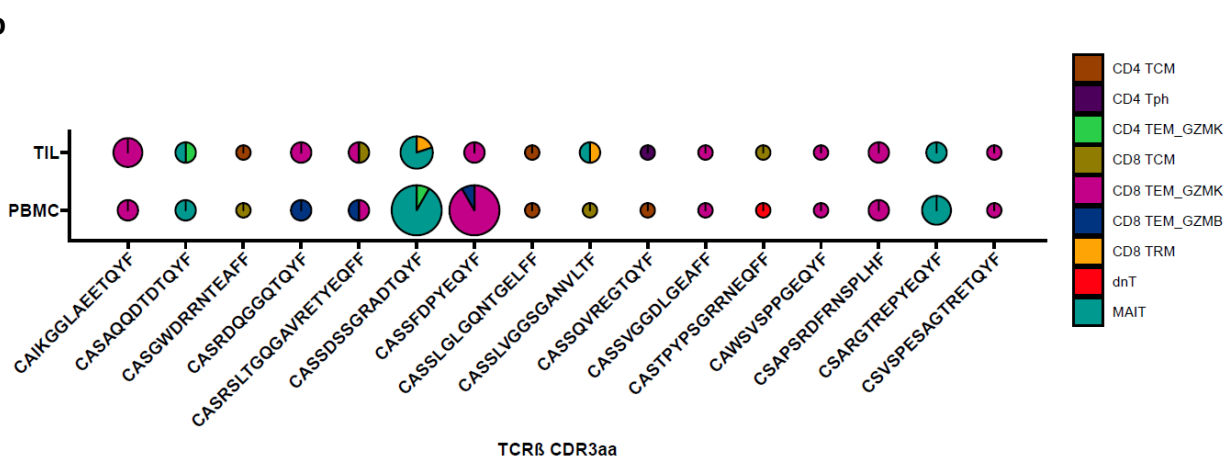


1744 **Extended Data Fig. 11 | Single cell sequencing of post-treatment TIL from patient OT6. a,**  
1745 Uniform Manifold Approximation and Projection (UMAP) for 562 T cells identified by single cell  
1746 RNA/TCR/BCR sequencing of CD3<sup>+</sup>CD19<sup>+</sup> FACS-sorted tumor infiltrating lymphocytes. **b,** Barplot  
1747 showing number of single cells per cluster. **c,** Violin plots showing expression of subset specific  
1748 marker genes across clusters. **d-e,** UMAPs showing clonality of single cells with an associated T  
1749 cell receptor sequence (**d**) and single cells with a TCR $\beta$  identified in microdissected TLS (**e**). **f,**  
1750 Stacked barplot showing proportion of each single cell cluster identified in TLS. **g,** Heatmap  
1751 showing gene expression of the top 3 differentially expressed genes per cluster. Rows represent  
1752 single genes and columns represent individual cells. Annotation bar indicates cluster identity,  
1753 whether each cell had a sequenced TCR, the clonality of the TCR, and whether the TCR was  
1754 identified in microdissected TLS from the same patient. **h-j,** Volcano plots showing differentially  
1755 expressed genes in the CD8 TEM\_GZMK (**h**), CD8 TEM\_GZMB (**i**), and CD4 Tph (**j**) clusters  
1756 compared to all other cells. Vertical dotted lines indicates a fold change of greater or less than  
1757 1.4 and horizontal line indicates a P value of 0.05. **k,** Inferred transcriptional phenotype of the top  
1758 15 TCR $\beta$  clonotypes in mature and involuted TLS of patient OT6.  
1759

1760 a  
1761

TCR $\beta$ CDR3aa	<i>n</i> cells in peripheral blood	<i>n</i> cells in tumor
CAIKGGLAEETQYF	2	4
CASAQQD TDTQYF	2	2
CASGWDRRNTAEFF	1	1
CASRDQGGQTQYF	2	2
CASRSLTGQGAVRETYEQFF	2	2
CASSDSSGRADTQYF	12	5
CASSFDPYEYQYF	12	2
CASSLGLGQNTGELFF	1	1
CASSLVGGSGANVLTF	1	2
CASSQVREGTQYF	1	1
CASSVGGDLGEAFF	1	1
CASTPYPSGRRNEQFF	1	1
CAWSVSPPGEQYF	1	1
CSAPSRDFRNSPLHF	2	2
CSARGTREPYEYQYF	4	2
CSVSPESAGTRETQYF	1	1

1762 b  
1763



1770  
1771  
1772  
1773  
1774  
1775  
1776  
1777  
1778  
1779  
1780  
1781  
1782  
1783  
1784  
1785  
1786  
1787

**Extended Data Fig. 12 | Cluster annotation of single cells with shared TCR $\beta$  in post-treatment peripheral blood and TIL (*n* = 16) from patient OT6. a, Shared TCR $\beta$  identified in both PBMC and TIL for patient OT6. Rows indicate different TCR $\beta$  clonotype and columns provide the complementarity determining region 3 (CDR3) amino acid sequence and number of cells with the TCR $\beta$  CDR3 amino acid sequence in peripheral blood and TIL, respectively. b, Single cell cluster identities of shared TCR $\beta$  according to unique CDR3 and compartment where the TCR was identified. Piecharts are colored according to the cluster identities of all cells with the same TCR $\beta$ . The radius of each piechart is proportional to the total number of cells in which each TCR $\beta$  was identified (square root of *n* cells divided by eight).**